# List of publications

- Structure and bonding of propyne on Cu(111) from density functional periodic and cluster models, A. Valcárcel, J.M. Ricart, A. Clotet, A. Markovits, C. Minot, F. Illas, J. Chem. Phys. 116 (2002) 1-6.

- Theoretical study of the structure of propene adsorbed on Pt(111), A. Valcárcel, J.M. Ricart, A. Clotet, A. Markovits, C. Minot, F. Illas, Surf. Sci. 519 (2002) 250-258.

- Comparative DFT study of the adsorption of 1,3-butadiene, 1-butene and 2-*cis/trans*-butenes on the Pt(111) and Pd(111) surfaces, A. Valcárcel, A. Clotet, J.M. Ricart, F. Delbecq, P. Sautet, Surf. Sci. 549 (2004) 121-133.

- Theoretical study of propene adsorbed on sulphated Pt(111), A. Valcárcel, A. Gil, A. Clotet, J.M. Ricart, Chem. Phys. Lett. 339(2004) 295-299. .

- Theoretical interpretation of the IR spectrum of propyne on Cu(111), A. Valcárcel, J.M. Ricart, F. Illas, A. Clotet, J. Phys. Chem. B 108 (2004) 18297-18305.

- Comparative theoretical study of the structure and bonding of propyne on the Pt(111) and Pd(111) surfaces, A. Valcárcel, A. Clotet, J.M. Ricart, F. Illas, Chem. Phys. 309 (2005) 33-39.

- Selectivity control for the catalytic 1,3-butadiene hydrogenation on Pt(111) and Pd(111) surfaces: radical versus closed-shell intermediates, A. Valcárcel, A. Clotet, J.M. Ricart, F. Delbecq, P. Sautet, J. Phys. Chem. B, in press.

- Analysis of the reaction intermediates for propylene dehydrogenation on Pt(111), A. Valcárcel, A. Clotet, J.M. Ricart, F. Illas, A. Markovits, C. Minot, in preparation.

- DFT characterization of adsorbed $NH_x$ species on Pt(111) and Pt(100) surfaces, G. Novell-Leruth, A. Valcárcel, A. Clotet, J.M. Ricart, J. Perez-Ramirez, J. Phys. Chem. B, submitted.

# Agraïments

Primer de tot, vull agrair a la meva família el seu recolzament incondicional. Gràcies per donar-me ànims constantment, per estar al meu costat en els moments bons i en els no tant bons. Mai us podré agrair prou tot el que heu fet per mi. Gràcies!

Agraeixo als meus directors de tesi, Josep Manel Ricart i Anna Clotet, haver-me permès incorporar-me al seu grup, donar-me l'oportunitat de realitzar aquesta tesi i la seva ajuda. A la resta dels *seniors* i col·laboradors directes de l'Àrea de química quàntica, gràcies sense excepció ja que de tots i cada un de vosaltres també he après molt.

Menció especial mereixen en Jose C., en Joan i L'Elisenda, pel seu magnífic treball al càrrec de la 'maquinaria' del grup i, concretament per haver estat els "metges de capçalera" del meu ordinador.

El meu agraïment més especial és, però, pels meus "companys de la ex-5ena planta": l'Alfred, en Paco, en Gerard, en Benjamí, en Dani, la Isa, la Susanna, l'Esther, l'Elena, la Núria, en Jesús, en David, el Campa, l'Elies, en Xavi, en Jose, en Jorge i en Juan Miquel ... i per als fitxatges més recents, en Toni i en Jordi. Moltíssimes gràcies!!!!!!!!!!!!!

Vull donar gràcies a Philippe Sautet i Françoise Delbecq, per haver-me acollit al seu grup a l'*Ecole Normale Superieure* de Lyon i fer-me sentir com a casa. El capítol 5 d'aquesta tesi no hagués estat possible sense la seva valuosa col·laboració. A la resta de companys de Lyon, també gràcies.

Vull agrair a Christian Minot i Alexis Markovits per donar-me l'oportunitat de fer una profitosa estada el seu grup a la Universitat *Pierre et Marie Curie* de Paris.

En l'àmbit institucional vull agrair a la Generalitat de Catalunya la concessió d'una beca pre-doctoral i a la Unió Europea la beca *Marie Curie*. També, vull expressar el meu agraïment la Universitat Rovira i Virgili i, especialment, al Departament de Química Física i Inorgànica.

Finalment, gràcies a les meves amigues, especialment a la Iolanda per la seva ajuda inestimable en la confecció de la portada i per donar-me un copet de mà amb la llengua de Shecspir.

# 3

# Propyne on the (111) surfaces of Cu, Pt, Pd and Rh: adsorption sites, bonding mechanism and vibrational spectra

*We have studied the adsorption of propyne on the (111) surfaces of Cu, Pt, Pd and Rh. On Cu (111), we have found that propyne adsorbs with its molecular plane perpendicular to the surface and bisecting a Cu-Cu bond. On Pt(111), Pd(111) and Rh(111), propyne prefers to sit on a 3-fold hollow site, with the C≡C axis parallel to a metal-metal bond and the molecular plane tilted away from the surface normal. The analysis of the DOS has allowed us to explain the apparently anomalous adsorption behaviour of propyne on the Cu surface. The simulation of the vibrational spectra has permitted us to corroborate and complete the experimental band assignment and confirm the adsorption site preference for propyne on Cu and Rh. Our calculations have also given a possible explanation for the presence of the MSSR-inactive C≡C stretch on Cu. For propyne on Pt and Pd,we have predicted the vibrational bands that will appear in the spectrum.*

*This chapter is organised as follows: section 3.1 is a literature review of the experimental and theoretical data available for propyne adsorbed on Cu(111), Pt(111), Pd(111) and Rh(111); section 3.2 discusses the geometry and vibrational spectrum of gas-phase propyne; section 3.3 presents the results for the adsorption of propyne on the (111) surfaces of Cu, Pt, Pd and Rh and discusses these results in terms of electronic and vibrational properties, through the analysis of the DOS and the simulated vibrational spectra; section 3.4 summarises the conclusions of this work.*

## 3.1 Introduction

The chemistry of alkynes on metal surfaces exhibits a remarkable complexity that cannot be anticipated from the molecular structure and reactivity of the corresponding gas-phase molecules. The establishment and understanding of the microscopic mechanisms of these surface reactions requires the determination of the structure of the adsorbed molecules. Among the large number of surface analytical methods, vibrational spectroscopies (RAIRS and HREELS) are widely used in heterogeneous catalysis research [1-3]. The analysis of vibrational spectra, in particular, the assignment of the adsorbate vibrational modes, provides valuable information regarding the adsorbate structure, bonding modes and adsorption sites [4]. This information largely contributes to establish a first step towards the understanding of the elementary reaction steps occurring at the surface. The assignment of vibrational frequencies in terms of group functional frequencies is claimed to be very useful [6] although one must realize that this kind of analysis is based on rather classical arguments [7]. For adsorbates that retain most of their gas phase geometric and electronic structure, the assignment of vibrational frequencies is straightforward; it just requires direct comparison with available data for the gas phase molecule. However, when the interaction between the adsorbate and the surface implies a largely distorted structure for the adsorbate, the assignment becomes much more difficult. In some cases, it is possible to extract information from the IR spectra of the corresponding molecule obtained in different, but related, chemical environments such as inorganic complexes [8]. Nevertheless, this may lead to serious errors because the surface may strongly influence some particular normal modes [9]. Once vibrational bands are assigned, several hypotheses about the adsorption geometry are formed usually applying symmetry constrains and the *metal surface selection rule* (MSSR) [10,11]. Assuming the validity of this rule, it is usual to predict whether a given bond is parallel or not to the surface, on the basis of the presence or absence of the corresponding stretching band on the spectrum. Unfortunately, a lack of appreciation of the extent to which normal modes are composed of two or more coordinates produces errors in the assignation. Often, arguments based on Fermi resonances are to be invoked when a given band cannot be directly assigned.

Propyne ($CH_3C{\equiv}CH$) is one of the simplest hydrocarbons with more than two carbon atoms and an ideal candidate to study the structure and bonding modes of alkynes. In

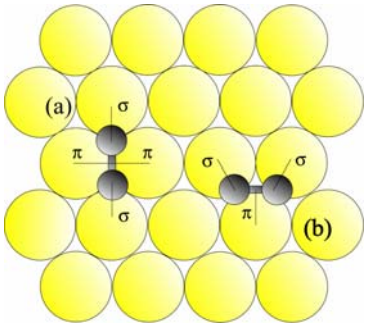


**Scheme 3.1.** Schematic diagram of the adsorption site of propyne on a (111) surface. Species (a) di-σ/di-π bonded and species (b) di-σ/π bonded.

principle, it is reasonable to expect propyne surface chemistry on metal surfaces to be similar to that of acetylene, as both molecules possess the same triple bond functionality. Besides, similarly to acetylene, propyne trimerises to form trimethylbenzene on the Pd(111) surface [12] and mainly undergoes dehydrogenation and further decomposition to surface carbon on both Pt(111) and Rh(111) surfaces [13,14]. However, it has been reported that the coupling reactions of propyne on Cu(111) are very different from those exhibited by acetylene. Actually, acetylene trimerises over Cu(111) even at low temperature while propyne mostly desorbs and undergoes dimerisation to benzene in a small fraction [15]. Structural studies have ascribed the low reactivity of propyne to steric repulsion between the methyl groups [16,17]. Elucidating the nature of the propyne-surface interaction, adsorption site, adsorption modes, packing arrangement and adsorption energies for these metals may also shed light on the causes of the different reactivity.

The carbon skeleton of propyne adsorbed on Cu(111) has been established by means of quantitative surface structure analysis based on the C(1s) Photoelectron Diffraction, PhD, technique. Likewise, LEED studies have also unambiguously established the long-range periodicity of propyne adsorbed on Cu(111) [16]. The propyne molecule binds to the copper surface in a di-σ/di-π adsorption mode (see **Scheme 3.1**) with its triple bond parallel to the surface in a cross-bridge position. A very important conclusion of this experimental study is that propyne arranges in a 4x√3 fashion. In a later study [18], McCash and co-workers have proposed a similar long-range periodicity for acetylene on Cu(111). Unfortunately, available structural information on the adsorption of propyne on Pt(111), Rh(111) and Pd(111) surfaces is relatively scarce. Comparison to acetylene adsorption mode suggests that propyne is also di-σ/π-bonded (see **Scheme 3.1**) to the Pt(111) surface [19]. A later temperature programmed desorption (TPD) study estimated a binding energy of ~–160 kJmol$^{-1}$ at 0.25 ML coverage [13]. For propyne on Rh(111), an exhaustive experimental study [14] has proposed that this molecule binds to the Rh surface with its unsaturated bond approximately parallel to the surface forming a 2x2 ordered pattern but no detailed information about the adsorption mode and adsorption site is available. To the best of our knowledge there is no structural information available for propyne on Pd(111).

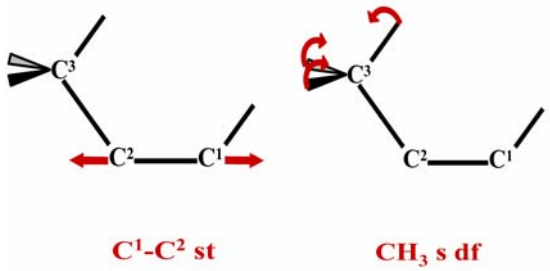


**Scheme 3.2.** Schematic representation of the $C^1$-$C^2$ stretch and the $CH_3$ symmetric deformation modes.

Experimental vibrational studies on Cu(111) [8] and Rh(111)[14] complete the structural information available. Despite the importance of these rigorous works, some bands have not been unambiguously assigned. In particular, the feature in the 1300–1400 $cm^{-1}$ region has been attributed either to the $C^1{\equiv}C^2$ stretching ($C^1{\equiv}C^2$ st) or to the $CH_3$ symmetric deformation ($CH_3$ s st), see **Scheme 3.2**. On Cu(111), Chesters *et al.* assigned the band at 1361 $cm^{-1}$ to the $C^1{\equiv}C^2$ stretch mode on the basis of a shift down to 1353 $cm^{-1}$ upon deuteration of the 'acetylenic' hydrogen. Indeed, the EELS [20] and RAIR [8] spectra of acetylene on Cu(111) exhibits a strong peak at 1307 and 1294 $cm^{-1}$ which has been also assigned to the $C^1{\equiv}C^2$ stretch. In these studies, the presence of the MSSR-inactive $C^1{\equiv}C^2$ stretch has been justified in terms of changes in dipole moment perpendicular to the surface arising from modification of the electron density near the $C^1{\equiv}C^2$ bond region produced by the vibrational mode parallel to the surface. McCash *et al*. [4] have suggested that this electron density change is enough to make this vibrational mode MSSR active and so intense. On the other hand, on Rh(111), Bent and co-workers [14] have assigned the 1370 $cm^{-1}$ signal to the $CH_3$ symmetric deformation by comparison with the gas phase propyne spectrum. Later studies on Cu(110), Ni(111)[21], Pd(110)[22] have discussed the assignment of the bands in the 1300–1400 $cm^{-1}$ region. On the Cu(110) and Ni(111) surfaces, Roberts *et al.*[21] have also assigned the 1354 and 1358 $cm^{-1}$ features to the methyl symmetric deformation. They have based their assignment on the fact that methyl group deuteration produces a significant shift of these bands towards lower frequencies. In a similar way, Camplin *et al.* [22] have found that deuterium substitution on the acetylenic hydrogen does not affect the position of the 1343 $cm^{-1}$ band on Pd(100) and thus they have assigned this peak to the methyl symmetric deformation although the same authors admit that the corresponding feature for propyne on Cu(111) may indeed correspond to the $C^1{\equiv}C^2$ stretching mode. They have proposed that in the last case the unit cell dimensions are such that the distance between two adjacent hollow sites matches that of the $C^1{\equiv}C^2$ bond of the chemisorbed propyne. This correspondence may allow the $C^1{\equiv}C^2$ stretch to become active at the expense of the methyl deformation.

**Table 3.1.** Calculated and experimental frequencies (in $cm^{-1}$) for the free propyne molecule

| vibrational mode | calc. ($\omega_i$) | exp. ($\nu_i$) | $\Delta_{calc.-exp}$ |
|---|---|---|---|
| CH st | 3398 | 3334 | 64 |
| $CH_3$ as st | 3019 | 3008 | –11 |
| $CH_3$ s st | 2976 | 2918[a] | 58 |
| $C^1{\equiv}C^2$ st | 2172 | 2142 | 30 |
| $CH_3$ as df | 1424 | 1452 | –28 |
| $CH_3$ s df | 1359 | 1382 | –23 |
| $CH_3$ ro + λ CCC b | 1001 | 1053 | –52 |
| $C^2$-$C^3$ st | 958 | 931 | 27 |
| CH b | 619 | 633 | –14 |
| CCC b | 325 | 328 | –3 |

Key: as, asymmetric; s, symmetric; st, stretching; df, deformation; ro, rocking; b, bending.
[a]Selected value. Fermi resonance with the $CH_3$ as df overtone. Experimental values at 2941 and 2882 $cm^{-1}$.

The need for a theoretical study is evidenced both by the lack of completeness of the available structural information and the existing disagreement in the literature regarding band assignment. Computational chemistry studies can be very useful in understanding the interaction of adsorbates with metal surfaces. The advantage of these studies is that they allow to obtain information that is difficult to measure experimentally such as adsorption energies for different structures or C−H distances. Moreover, the modern theoretical methods of electronic structure applied to surface science phenomena permit to obtain all the frequencies and, which is more important, they allow to get their relative intensities without further assumptions. Likewise, spectra for different isotopic substituted species —complicated and expensive to produce experimentally—can easily be obtained from theory with no significant additional cost.

For this chapter, we performed a series of self-consistent DFT calculations to asses the adsorption behaviour of propyne on four (111) metal surfaces: Cu, Pt, Pd and Rh. These surfaces were selected by the vast interest in catalysis of these four metals. The focus was on the adsorption site, electronic and vibrational properties, with a close comparison with the experimental results available. Our discussion is mainly focused on the comparison of the calculated vibrational spectra on the different metal surfaces.

## 3.2 Gas-phase propyne

First, for sake of comparison, the geometry of the gas phase molecules was optimised. We took a large box unit cell (15x15x15 $Å^3$) to avoid lateral interactions between periodic images. The results for the propyne molecule were close to the ones in previous experimental and theoretical studies [23]. The computed $C^1{\equiv}C^2$ and $C^2{-}C^3$ distances are

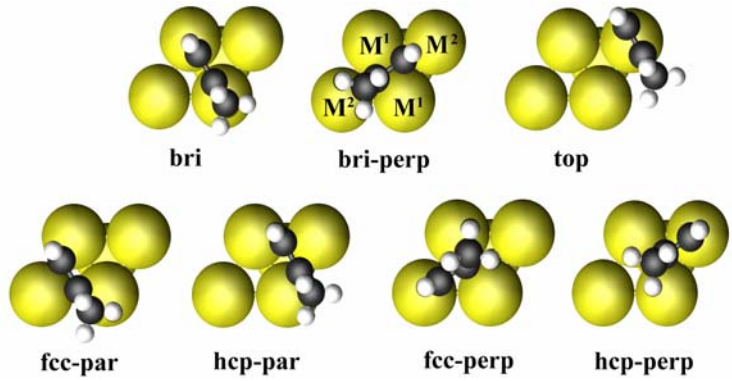


**Figure 3.1.** Scheme of adsorption structures for propyne on (111) metal surfaces.

1.21 Å, and 1.45 Å, respectively and the $C^1{\equiv}C^2{-}C^3$ angle is 180º as expected. The computed frequencies and assignments for gas phase propyne are displayed in **Table 3.1** where experimental results [24] have also been included for comparison. The agreement between experimental and calculated data is fairly good. Actually, the average deviation for the PW91 harmonic calculated vibrational frequencies ($\omega_i$) with respect to the fundamental experimental values, $\nu_i$, is of ~30 $cm^{-1}$.

The accurate assignment of the corresponding bands requires special care. In fact, upon deuteration couplings between group frequencies can appear, disappear or change their relative percentage. On deuteration of the 'acetylenic' hydrogen the CH st frequency shifts down and couples with the $C^1{\equiv}C^2$ st. McCash and co-workers [8] have also reported the existence of this coupling in the spectrum of physisorbed propyne on Cu(111). In this weak adsorption mode (physisorption) the molecule keeps its gas phase geometry and consequently its spectra can be compared to that of free propyne.

### 3.3 Adsorbed propyne

We identified at least seven different adsorption modes as possible starting points for geometry optimisations. The ball-and-stick representations are shown in **Figure 3.1**. The structures can be grossly classified as bridge (bri) when the C≡C is directly above a $M^1{-}M^1$ bond, hollow (fcc or hcp) when the molecule sits in a three-fold hollow site and top when the C≡C bond is directly above one metal atom. Depending on the angle formed by the C≡C axis and the $M^1{-}M^1$, we can distinguish two orientations namely parallel (par) and perpendicular (perp). Clotet and Pacchioni [25] have identified analogous structures for acetylene on Cu(111) and Pd(111). However, the lower symmetry of the propyne molecule duplicates some surface structures. For bri-perp two alternative situations exist depending on the position of the 'acetylenic' unit ($C^1$–H). The 'acetylenic' unit can sit on the fcc hollow site (see **Figure 3.1**) or on the hcp one. For sake of simplicity, we named them bri-

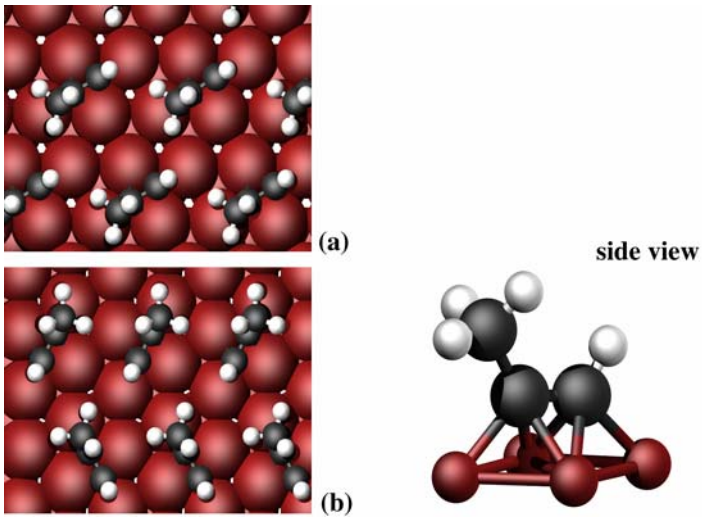


**Figure 3.2.** Bridge perpendicular (bri-perp) of propyne on Cu(111): 2x2 unit cell (a) and 4x√3-rect unit cell (b).

perp ($C^1$–H on fcc) and bri-perp' ($C^1$–H on hcp). Similarly, for fcc-perp and hcp-perp structures the $C^1$–H unit can be placed above the $M^2$ atom (**Figure 3.1**) or above the $M^1$–$M^1$ bond (not shown in the figure).

We performed the geometry optimisations using a 2x2 unit cell (associated with a molecular coverage of 0.25 ML). For propyne on Cu(111) a 4x√3 unit cell was also used to reproduce the LEED pattern observed experimentally [16]. We computed the adsorption energies with **equation 2.41** (**section 2.10**, **Chapter 2**). We also carried out frequency calculations with a 2x2 unit cell except for Cu, for which we used the experimental supercell [26]. Moreover, for the Rh surface, we also performed some calculations with a bigger supercell (two propyne molecules in a 2x4 unit cell).

### 3.3.1 Geometry, adsorption site preference and adsorption energy

*Propyne on Cu(111)*. We consider first the case of propyne adsorbed on Cu(111). We found that only bri-perp structures are stable. These adsorption sites are fully compatible with the di-σ/di-π adsorption mode predicted by experiments. The adsorption energy is –73 kJmol$^{-1}$ on the 2x2 unit cell (**Figure 3.2a**). The two possible orientations are strictly equivalent i.e. there is no difference in adsorption energy (nor in adsorption geometry, see below). The slab model permitted us to reproduce the long-range order proposed from LEED experiments (4x√3 unit cell, see **Figure 3.2b**) [16]. The adsorption energy is slightly larger on the 4x√3 unit cell (–98 kJmol$^{-1}$) than on the 2x2 one. The 4x√3 unit cell is the most stable adsorbed overlayer, as predicted from experiments.

We found no difference in the geometry of the two possible bri-perp structures (bond distances are equal up to the second decimal number). Moreover, both the 2x2 and the 4x√3 unit cell predicted identical adsorption geometry. This is a highly distorted propyne with the methyl group tilted away from the surface. The molecular $C^1$–$C^2$–$C^3$ plane is perpendicular to the surface (see **Figure 3.2** side view). The computed $C^1$–$C^2$ distance is 1.38 Å. Notice that the calculated value is well within the error bars of the experimental value which is 1.47 ± 0.16 Å. Similarly, the calculated $C^2$–$C^3$ distance is 1.51 Å to be compared with an experimental value of 1.57 ± 0.14Å and the $C^1$–$C^2$–$C^3$ bond angle is of 122º to be compared with a PhD value of 123 ± 7º (experimental values from ref. 16). There are several internal parameters that cannot be predicted by the diffraction experiments. Those are the bond distances and bond angles concerning the propyne hydrogen atoms. Not surprisingly, the C-H distances are all within 1.100±0.005Å where the error bars cannot be taken strictly as errors but as a measure of the dispersion of obtained results. The hydrogen methyl atoms are in a *cis* orientation, with one of the H atoms in $C_3$ almost in front of that in $C_1$ (**Figure 3.2**). Nevertheless, the rotation of the methyl group along the $C^2$–$C^3$ axis is almost free (less than 4 kJmol$^{-1}$). More important is the H– $C^1$–$C^2$ angle because it provides a measure of the $C^1$ hybridization. The calculated value is 120º and adds further support to a di-σ/di-π adsorption mode with $C^1$ and $C^2$ both on a $sp^2$-$sp^3$ like hybridisation. Here, it is important to point out that due to the lack of accuracy on PhD prediction of the bond distances that are nearly parallel to the surface. Toomes *et al.* [16] have not been able to distinguish between $sp^2$ and $sp^3$ hybridisation on $C^1$ and $C^2$. Chesters and McCash raised similar claims from the vibrational analysis [8]. The present values for the $C^1$–$C^2$ bond distance and H–$C^1$–$C^2$ and $C^1$–$C^2$–$C^3$bond angle strongly suggest an $sp^2$-$sp^3$ hybridisation. Indeed, this hybridisation is consistent with the di-σ/di-π coordination mode whereas it is difficult to understand the bonding of propyne to the surface with tetrahedral $C^1$ and $C^2$ atoms.

Finally, we discuss the vertical distances from the propyne carbon atoms to the surface plane and the surface relaxation. Experimentally it appears that both bri-perp and bri-perp' possibilities have the same probability and no structural differences are found. Hence, any deviation on the calculated geometry (or adsorption energy) of the two orientations could be taken as a measure of the model limitations. The vertical distances of C atoms to the surface in both the bri-perp and bri-perp' orientations are 1.39 ($C^1$) and 1.47 ($C^2$) to be compared with the experimental values, 1.44 ± 0.04 Å and 1.45 ± 0.04 Å, respectively. The vertical distances commented above are not changed when the two orientations within the 4x√3-rect unit cell were considered. Minor changes are observed on the Cu(111) surface upon adsorption of the propyne molecule. The three Cu atoms surrounding the $C_2$ move upward while the one directly under the 'acetylenic' unit moves inward, causing a slight corrugation of the metallic surface (< 3%). The changes on the second metal layer are even smaller. Only the hcp Cu atoms in the adsorption site move down, away from the carbon atom directly above.

*Propyne on Pt(111).* Among all the structures described above there are only two, fcc-par and hcp-par, which correspond to stable stationary points with minimum energy. The calculated adsorption energies for a coverage of 0.25 ML are –197 kJ mol$^{-1}$ for the fcc-par

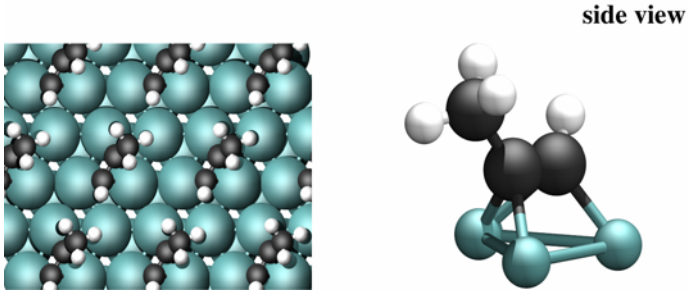


**Figure 3.3.** Hollow parallel (fcc-par) adsorption of propyne on Pt(111): 2x2 unit cell.

site and –193 kJ $mol^{-1}$ for the hcp-par one. We can consider these surface structures equivalent as the energy difference between the fcc and hcp sites is only of 4 kJ $mol^{-1}$. On the other hand, this result is nicely compared with the TPD suggested value of ~–160 kJ $mol^{-1}$ at 0.25 ML coverage [13]. Moreover, the energy barrier to diffusion perpendicular to the bridge is expected to be small based on the small energy gradients across the bridge computed during the geometry optimisation. It is worth to point out that the adsorption energy of propyne is smaller than the –218 kJ $mol^{-1}$ [29] or –229 kJ$mol^{-1}$ [27] reported for the adsorption energy of the acetylene molecule also on Pt(111) using similar methods and models. The difference can be attributed to the presence of the extra methyl group, as in the case of adsorbed propylene compared to ethylene on Pt(111) [28] (see also **Chapter 4**).

On the Pt(111) surface, the molecule binds to two Pt atoms (di-σ bond) and forms an additional π bond with a third Pt (see **Figure 3.3**). The resulting structure is in a good agreement with the di-σ/π one suggested by early experimental studies [19]. Due to the extra π-bond, the molecular $C^1$–$C^2$–$C^3$ plane is tilted away from the surface normal of ~ 15º (side view, **Figure 3.3**). Both minimum energy structures have similar adsorption energies and rather similar geometries indicating that the bonding is dominated by the three surface atoms defining a hollow site with little influence of the atoms in the second and third layers. Propyne adsorbs on Pt(111) with the $C^1$–$C^2$ bond almost parallel to the surface and the methyl group pointing outwards the metal surface with a $C^1$–$C^2$–$C^3$ angle of 125º (124º) for the fcc-par (hcp-par) structure. The $C^2$–$C^3$ is 1.50 Å for both surface minima and we did not find significant differences in the C–H bond distances (~1.10 Å). The $C^1$–$C^2$ distances are 1.39 Å and 1.40 Å for the fcc and hcp modes, respectively. This value can be used as a measure of the activation of the $C^1$–$C^2$ bond. Evidently, the $C^1$–$C^2$ distance is rather elongated from the calculated value for the gas-phase propyne (1.21 Å) and lies between the usual distances for a double (1.34 Å, gas-phase propylene) and a single bond (1.54 Å, gas-phase propane). The significant elongation of the $C^1$–$C^2$ distance indicates a considerable loss of triple-bond character upon adsorption. Similar elongation of the triple bond (1.40 Å) has been recently reported for acetylene on the Pt(111) surface [29]. The 123º value for the H–$C^1$–$C^2$ angle adds further support to a di-σ/π adsorption mode with $C^1$ and $C^2$ both in a $sp^2$–$sp^3$ like hybridisation.

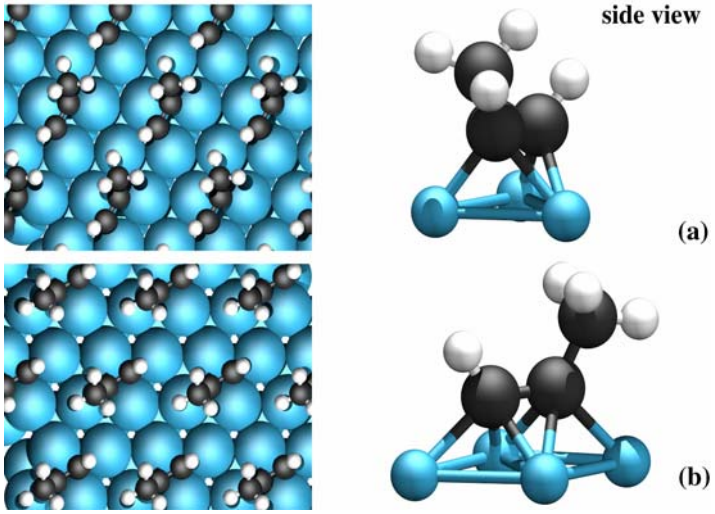


**Figure 3.4.** Adsorption of propyne on Rh(111): 2x2 unit cell; hcp-par (a) and bri-perp' (b).

The vertical distances of $C^1$ and $C^2$ atoms to the metal surface are 1.44 Å and 1.52 Å respectively for the fcc-par and 1.45 Å ($C^1$) and 1.53 Å ($C^2$) for the hcp-par mode. As for the Cu(111) surface, minor changes are observed on the Pt(111) one upon adsorption of propyne. The surface metal atoms in the adsorption site move slightly upward (~0.12 - 0.24 Å) to the adsorbed molecule whereas the fourth atom in the unit cell moves inward (~0.1 Å). This produces a small surface corrugation. The relaxation of atoms in the second metal layer is even smaller. Therefore, the space between to consecutive metal layers increases in ~4%.

*Propyne on Pd(111).* When adsorption takes place on the Pd(111) surface, we obtained the same geometrical trends we found for the adsorption on the Pt(111) surface. Among all the initial structures tested, only the fcc-par and the hcp-par adsorption modes led to stable structures. Similarly to Pt, we can consider the two minima *quasi*-degenerate as the adsorption energies are –160 and –161 kJ $mol^{-1}$ for the fcc and hcp adsorption modes, respectively. There appears to be no difference between binding at fcc *versus* hcp sites; that is, the presence or absence of the second layer Pd atom, below the hollow site does not affect the adsorption. In this case, the adsorption energy is also smaller than the computed one for acetylene on Pd (-196 kJ $mol^{-1}$) [29].

Both minima also have quite close geometries. The molecule binds to the metal surface in a di-σ/π fashion with the molecular plane slightly tilted from the surface normal (~13º). The $C^1$–$C^2$ distance is 1.36 Å for the fcc-par and 1.37 Å for the hcp-par adsorption mode. DFT periodic calculations carried out by Mittendorfer and co-workers [29] predict the same $C^1$–$C^2$ distance for the acetylene molecule adsorbed on Pd(111), which is indeed close to the experimental value of 1.34 Å [30]. The calculated H–$C^1$–$C^2$ and $C^1$–$C^2$–$C^3$angles are

**Table 3.2.** Computed propyne adsorption energies (in kJmol$^{-1}$) and geometries (distances in Å, angles in degrees) for the most stable structures on the (111) surface of Cu, Pt, Pd and Rh

| | **Cu** | **Pt** | **Pd** | **Rh** | |
|---|---|---|---|---|---|
| Adsorption mode | bri-perp | fcc-par | fcc-par | hcp-par | bri-perp' |
| Adsorption energy | –98 | –197 | –161 | –226 | –209 |
| $C^1$–$C^2$ distance | 1.38 | 1.39 | 1.36 | 1.39 | 1.42 |
| $C^2$–$C^1$–H angle | 123 | 123 | 125 | 123 | 120 |
| $M^1$–$C^1$ /$C^2$ distance | 2.13 /2.13 | 2.01/2.02 | 2.00/2.03 | 2.04/2.01 | 2.11/2.20 |
| $M^2$–$C^1$ /$C^2$ distance | 2.04/2.06 | 2.20/2.25 | 2.19/2.22 | 2.20/2.16 | 2.19/2.18 |
| Tilt[a] | 0 | 16 | 14 | 15 | 0 |

[a]Angle of the molecular plane of propyne with respect to the surface normal.

125º and 127º for both surface minima. These values strongly suggest a $sp^2$ to $sp^3$ hybridisation consistent with the di-σ/π coordination mode.

For the fcc-par structure the height of $C^1$ and $C^2$ atoms above the metal surface is 1.45 Å and 1.55 Å, respectively. These distances are only 0.01 Å longer for the hcp-par structure. The Pd surface relaxation is ~3%.

*Propyne on Rh(111)*. The computed adsorption behaviour of propyne on Rh(111) follow similar trends to the results for the other metals. We performed the calculations using a 2x2 unit cell. Indeed, Somorjai and co-workers [14] have suggested that this is the pattern propyne forms on the Rh surface. On this metal surface, four different adsorption modes correspond to minima: hollow-par (fcc and hcp) and the bri-perp structures (see **Figure 3.4**). The hollow-par adsorption sites are the most stable ones with adsorption energies of –226 kJmol$^{-1}$ and –216 kJmol$^{-1}$ for the hcp-par and fcc-par structures, respectively. Contrary to Pt and Pd, on the Rh surface the adsorption on the hcp hollow site is slightly favoured compared to the adsorption on the fcc. Previous theoretical studies have pointed out this site preference for molecules (such as acetylene or NO) and atoms (C, N) [27,31]. The bri-perp surface structures have somehow lower binding energies (–207 for bri-perp and –209 kJmol$^{-1}$ for bri-perp'). The energy difference between bri-perp adsorption mode and the hcp-par surface structure is smaller than 20 kJmol$^{-1}$. This difference is not big enough to be conclusive. In fact, a recent study for CO adsorption on Pt(111) has shown that GGA-DFT yields an error of 10–20 kJmol$^{-1}$ for the comparison of adsorption sites [32], predicting an erroneous binding site. Hence, the simulation of the vibrational spectrum may be of great importance to confirm the site preference obtained from total energy calculations (see **section 3.3.3**). Allendorf and co-workers [27] have obtained similar results for acetylene on Rh(111). Both hollow-par and bri-perp structures lie in a small range of energies and the most stable adsorption site is also the hcp-par (–258 kJmol$^{-1}$).

Although the adsorption energies are rather similar, the differences in geometry are not negligible. The molecular geometry is clearly less distorted on the hollow-par than on the bri-perp structures. In fact, the calculated $C^1$–$C^2$ distance is 1.39 Å and the H−$C^1$–$C^2$ and $C^1$–$C^2$–$C^3$ angles are 123º and 124º for both surface minima (hcp and fcc) to be compared with 1.42 Å, 125º and 127º obtained for the bridge perpendicular minima (bri-perp and bri-

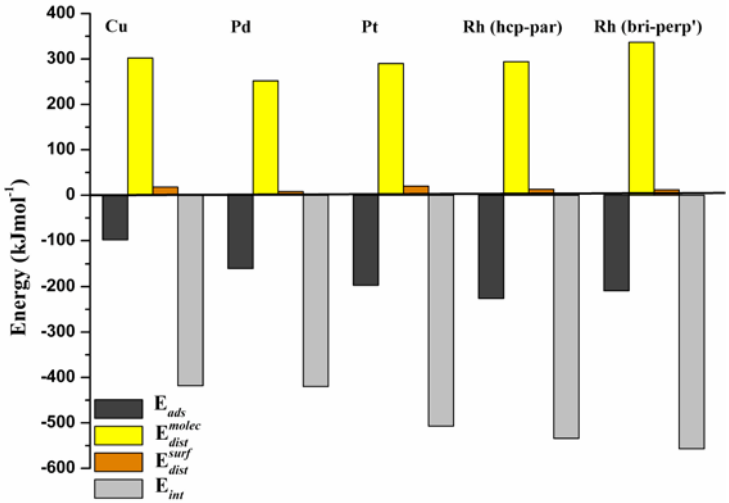


**Figure 3.5.** Decomposition of the adsorption energy for the most stable adsorption mode on the (111) surfaces of Cu, Pd, Pt, and Rh. Adsorption energy (dark grey), distortion energy of the molecule (yellow), distortion energy of the surface (orange) and interaction energy (light grey).

perp'). There are also rather important differences in the vertical distances. For the hollow-par structures the height of $C^1$ and $C^2$ atoms above the metal surface is 1.53 Å and 1.62 Å, respectively. However, these values are reduced to 1.40 Å ($C^1$) and 1.49 Å ($C^2$) for the bri-perp structures.

Similarly to the other metals studied, there are no significant changes in the geometry of the metal surface on adsorption. For all the minima, the surface relaxation is <4%. As expected, the changes in the Rh(111) surface are similar to those observed in Pt(111) and in Cu (111) for the hollow-par and for the bri-perp's structure, respectively.

**Table 3.2** summarises the results described above. It provides a list of adsorption energies and geometric parameters for the most stable adsorption mode on each metal surface. For the Rh surface, we also included the bri-perp' surface structure. We can explain the variation of adsorption energies on Cu (–98 $kJmol^{-1}$), Pd (–161 $kJmol^{-1}$), Pt (–197 $kJmol^{-1}$) and Rh (–209 $kJmol^{-1}$ for the bri-perp' structure and –226 $kJmol^{-1}$ for the hcp-par adsorption mode) in terms of geometric distortions and electronic interactions. We can decompose the adsorption energy in three terms (**Figure 3.5**): the distortion energy of the surface, related to the distortion of the first metallic layers; the distortion energy of the molecule, i.e the energy necessary to distort the molecule from its gas phase geometry to the adsorption geometry; and the interaction energy between the distorted molecule and the distorted surface. The distortion energy of the surface is a minor contribution. In all the cases, this value is smaller than 20 $kJmol^{-1}$ in good agreement with the small changes observed on the metal surface on adsorption (see above). The distortion energy of propyne increases following: Pd (252 $kJmol^{-1}$) < Pt (290 $kJmol^{-1}$) ≈ Rh (294 $kJmol^{-1}$, hcp-par) ≈ Cu (302 $kJmol^{-1}$) < Rh (337 $kJmol^{-1}$, bri-perp'). These values reflect the increasing deformation

of the molecular geometry upon adsorption. The hollow-par adsorption structures of Pt and Rh have surprisingly close geometries. On the other hand, the geometry of the bri-perp's structure differs from those obtained for propyne adsorbed on Cu(111). Distinctly, the distortion of the molecular geometry is higher on Rh. In fact, we can consider the changes in $C^1$–$C^2$ bond length and the H–$C^1$–$C^2$ angle as an indicative of the 'activation' of the molecule. The more elongated is the $C^1$–$C^2$ distance and the smaller is the H–$C^1$–$C^2$ angle the higher is the activation. The interaction energy between the two distorted fragments increases from Cu (–418 $kJmol^{-1}$) ≈ Pd (–420 $kJmol^{-1}$) < Pt (–507 $kJmol^{-1}$) < Rh (hcp-par, –534 $kJmol^{-1}$) to Rh (bri-perp, –557 $kJmol^{-1}$). The interaction energy is clearly stronger on Rh and Pt than on Pd and Cu. The rather strong activation and the high interaction of propyne on Pt and Rh cause the adsorbed molecule to be susceptible of decomposition. Our calculations are in good agreement with the experimental results [13,14]. Unfortunately, our results do not give any indication as to why propyne trimerises on Pd and dimerises on Cu. Experimental [15] and theoretical [17] studies have proposed the key intermediates and the mechanism for propyne dimerisation on Cu. The study of the reaction intermediates and the possible reaction pathways on both metal surfaces is necessary to establish the causes of the differences observed.

### 3.3.2 Electronic analysis

In the foregoing section, we have discussed the relative stability and adsorption site preference on the Cu, Pt, Pd and Rh surfaces. The analysis of the projected density of states (PDOS) with the simple frontier orbital model [33] can help us to understand the bonding mechanism. **Figures 3.6** and **Figure 3.7** show the PDOS on the atomic orbital of $C^1$ and the surface metal atoms. For Cu, Pt, and Pd we only considered the most stable structures whereas for Rh both hcp-par and bri-perp adsorption modes are analysed. In hollow-par and bri-perp's adsorption modes the orbitals into play are mainly the $p_x$ and $p_z$ of the C atom ($\pi$ system) and the $d_{xz}$, $d_{yz}$ and $d_z^2$ metal orbitals (d-band). However, we also investigated the contribution of the sp-band to the propyne-surface interaction. For these metals, the sp-band doses not strongly contribute to the adsorbate-surface interaction except for Cu (see discussion below).

First of all, we discuss the isolated propyne molecule. In each graphic, window (1) presents the PDOS on the $p_x$ and $p_z$ orbitals of the $C^1$ atom of both the gas phase (dotted line) and the 'distorted' propyne (full line) —i.e the isolated molecule but in the adsorption geometry—. The highest occupied molecular orbitals (HOMO) and the lowest unoccupied molecular orbitals (LUMO) are doubly degenerate in the gas phase. On adsorption, the molecular distortion results in a symmetry lowering and in a marked reduction of the HOMO-LUMO (H–L) gap. It is well known that the energy difference between the HOMO and the LUMO is directly linked to the distortion of the molecule: the higher is the distortion the smaller is the H–L gap. **Figure 3.8** shows that there is a clear linear relationship between the H–L gap and the energy cost to distort the propyne molecule from its gas phase geometry to the adsoption geometry. Moreover, this distortion causes an increase of the mixing between $p_x$ and $p_z$ orbitals with C orbitals of 'pure' $\sigma$ character. As a result of this mixing two peaks grow in the 4.5–7.5 eV range.

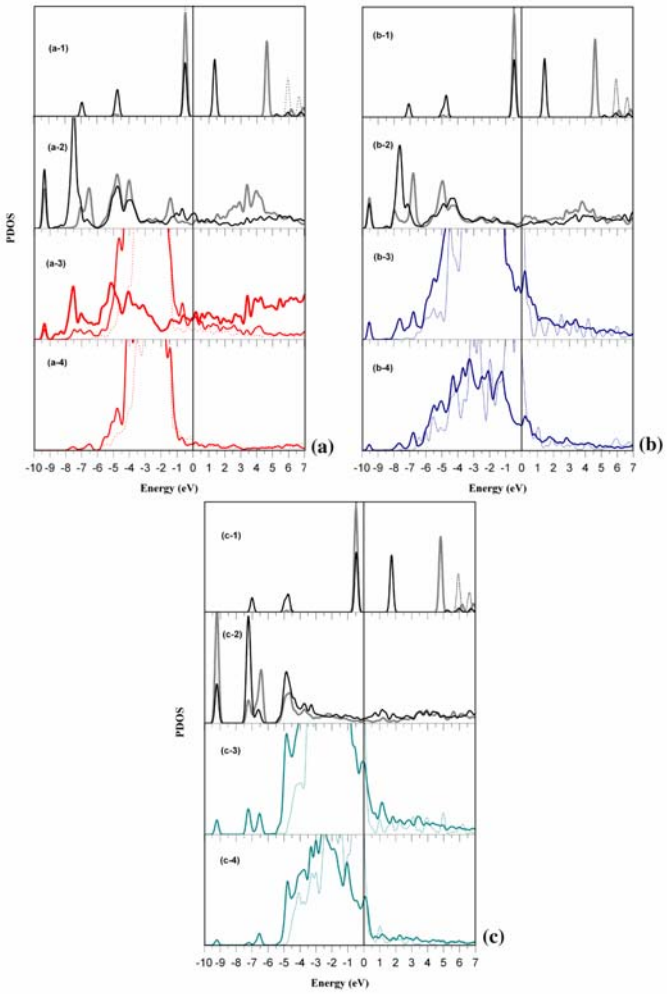


**Figure 3.6.** Density of states projected (PDOS) on the $p_x$ (gray) and $p_z$ (black) atomic orbitals of propyne and the $d_{z^2}$ and $d_{xz}+d_{yz}$ of Cu(111) (a); Pt(111) (b) and Pd(111)(c). Window 1, propyne in the gas phase (dotted line) and isolated propyne distorted as in the surface structure (full line). Window 2 adsorbed propyne. Window 3, $d_{z^2}$ of the clean (dotted line) and 'interacting' (full line) metal surface. For Cu, the sp-band is also depicted in window 3 (thick line). Window 4, $d_{xz}+d_{yz}$ of the bare surface (dotted line) and with adsorbed propyne (full line). Fermi level is taken as zero.

Due to the interaction with the metal surface, the adsorbate contributions are broadened and pushed to lower energies (see window (2)). The more 'dilute' the $p_x$ and $p_z$ contributions are, the stronger is the interaction with the metal surface. This is evident if we

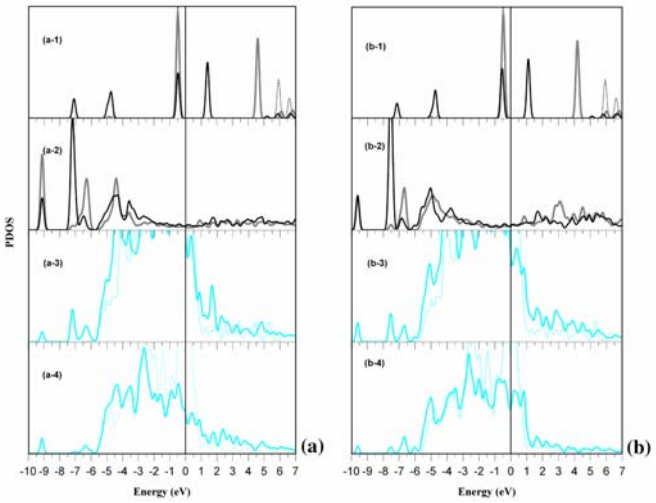


**Figure 3.7.** Density of states projected (PDOS) on the $p_x$ (grey) and $p_z$ (black) atomic orbitals of propyne and the $d_{z^2}$ and $d_{xz}+d_{yz}$ of Rh(111): hcp-par (a) and bri-perp'(b). Window 1, propyne in the gas phase (dotted line) and isolated propyne distorted as in the surface structure (full line). Window 2 adsorbed propyne. Window 3, $d_{z^2}$ of the clean (dotted line) and 'interacting' (full line) metal surface. Window 4, $d_{xz}+d_{yz}$ of the bare surface (dotted line) and with adsorbed propyne (full line). Fermi level is taken as zero.

compare, for example, the adsorption of propyne on Pt (interaction energy –507 $kJmol^{-1}$) and Pd (interaction energy –420 $kJmol^{-1}$), see **Figures 3.6b** and **c**. We can invoke similar arguments to compare the two stable adsorption structures on Rh (**Figures 3.7a-b**).

Windows (3) and (4) show the PDOS on the $d_{xz}$ + $d_{yz}$ and th $d_z^2$ orbitals for the clean (dotted line) and 'interacting' (full line) metal surface. For Cu (**Figure 3.6a**) we also included the sp-band. Notice that the Cu d-band remains rather narrow upon adsorption. Consequently, the interaction with the H–L contributions of propyne is less effective. On the other hand, there is a noticeable interaction of these orbitals with the sp-band. This interaction is evidenced by the matching energies between the sp contributions and $p_x$ and $p_z$ contributions. There is an important overlap of the s metal contributions and the π C–C antibonding orbitals, which strengthens the surface-adsorbate binding (peaks in the range 2–4.5 eV). These results are analogous to those of acetylene on the Cu(111) surface. Indeed, Clotet and Pacchioni [25] have proposed that the sp-band participates substantially in the acetylene binding to Cu.

For Pt, Pd and Rh, (**Figures 3.6b-c** and **Figure 3.7a-b**, respectively) the interaction takes place mainly with the $d_{xz}$, $d_{yz}$ and $d_z^2$ bands. Upon adsorption, the d contributions just below the Fermi level (taken as zero energy) are rather reduced, while new contributions appear at low energies (below the d-band bottom) and above the Fermi level from the bonding and antibonding contributions with the $p_x$ and $p_z$ orbitals. The interaction primarily takes place with the HOMO of propyne. However, there is a non negligible contribution of

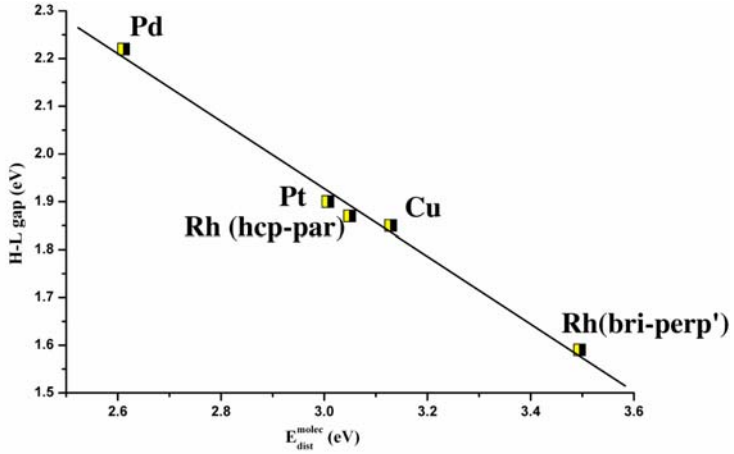


**Figure 3.8.** HOMO–LUMO gap *vs*. the distortion energy of the molecule. Energies in eV.

the propyne LUMO. The surface-metal interaction increases in the order Pd < Pt < Rh, well in line with the increase of the d-bandwidth. The greater expansion of the d orbitals favours the overlap of the metal and adsorbate states. The 4d orbitals of Pd are narrower than the 5d orbitals of Pt. Rh (a more electropositive metal) has higher d states and more diffuse orbitals. Moreover, the stronger distortion of the molecular geometry of adsorbed propyne (Rh > Pt > Pd) also favours the overlap between the adsorbate and the d metal band and propitiates the interaction.

The unique adsorption behaviour of propyne on Cu arises from the singular adsorbate-surface interaction.

### 3.3.3 Vibrational spectra

The system propyne/M(111) surface belongs to the $C_1$ symmetry (see **section 3.3.1**). Therefore, all the vibrational modes can be active. However, when the calculated frequencies are compared with the IR or HREELS spectra, the metal surface selection rule has to be taken into account [10,11]. Only modes that produce a significant change in the dipole moment perpendicular to the metal surface are active (for further details see **Chapter 2, section 2.6**)

Although the adsorbed system does not exhibit any particular symmetry, the propyne molecule has a local symmetry close to $C_s$. Actually, we can consider that the 'acetylenic' and the methyl hydrogens lie in the plane formed by the three C atoms because the deviation from this plane is always smaller than 5º. Thus, for sake of simplicity, we used the $C_s$ local symmetry and the group frequencies displayed in **Figure 3.9** to assign the bands. Our goal is to 'translate' the computed normal modes into 'functional group' modes. Sometimes vibrational normal modes are the sum of two (even more) functional group modes. So, we will use a '+' sign to indicate that two (or more) functional groups couple

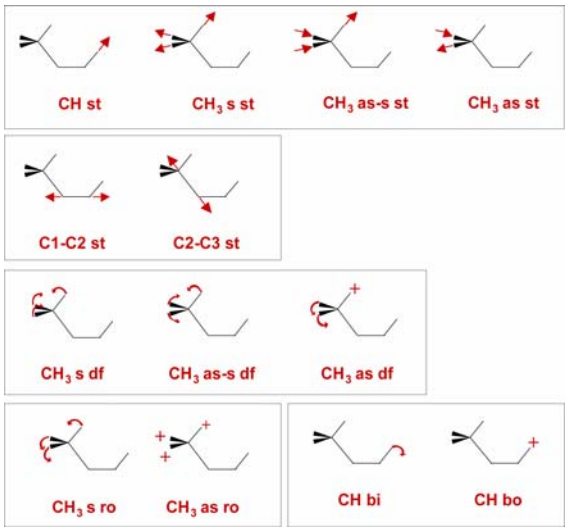


**Figure 3.9.** Notation used in the band assignation. Key: as, asymmetric; s, symmetric; st, stretching; bi, bending in-plane; bo, bending out-of-plane; ro, rocking; df, deformation. The as-s notation corresponds to nuclear displacements symmetric to molecular plane.

(or sum) in the sense displayed in **Figure 3.9** and a '–' sign when they couple in opposite sense (i.e. displacement vectors of each functional group move in opposite sense).

*Propyne on Cu(111)*. The experimental RAIR spectrum of propyne on Cu(111) [8] has four bands in the CH stretching region (2923, 2883, 2855 and 2828 $cm^{-1}$) and a quite strong feature at 1361 $cm^{-1}$. Chesters and McCash [8] have assigned the band at 2923 $cm^{-1}$ to the $CH_3$ as st, the one at 2883 $cm^{-1}$ to the $CH_3$ s st, the feature at 2855 $cm^{-1}$ to the 'acetylenic' hydrogen stretch (CH st), the peak at 2828 $cm^{-1}$ to the $CH_3$ s st coupled with the overtone of the $CH_3$ s df (Fermi resonance) and the band at 1361 $cm^{-1}$ to the $C^1$–$C^2$ st. Unfortunately, the resolution of this spectrum is rather low and the authors have only assigned the main bands with no attempt to resolve the numerous shoulders. To corroborate and complete the experimental assignment, we computed the vibrational frequencies of propyne on Cu(111) using two different models: a 2x√3 supercell (1 molecule per unit cell) and the 4x√3 supercell (experimental LEED pattern [16], 2 molecules per unit cell).

First, we computed the vibrational frequencies of the bri-perp and bri-perp' using the 2x√3 cell. **Table 3.3** shows these results. This model reproduces rather well the CH stretching region: $CH_3$ as st (3020/3024 $cm^{-1}$), $CH_3$ as-s st (3004/2997 $cm^{-1}$), CH st (2944/2944 $cm^{-1}$) and $CH_3$ s st (2923/2927 $cm^{-1}$). Here, the values in parenthesis correspond to the bri-perp and bri-perp' orientations, respectively. The anharmonic effects are obvious in the comparison between computed and experimental frequencies, with a discrepancy of the same range as in the gas phase propyne (see **section 3.2**). The model also reproduces rather well the band intensities in the 2900–3100 $cm^{-1}$ region. The $CH_3$ s st is the most intense feature followed by the CH st and the $CH_3$ as-s st mode. The $CH_3$ as st has an

**Table 3.3.** Computed frequencies (in $cm^{-1}$) for propyne ($CH_3CCH$) on Cu(111)

| vibrational mode | 2x√3 | | 4x√3 | |
|---|---|---|---|---|
| | $\omega_i$ | $I_i$[a] | $\omega_i$ | $I_i$[a] |
| A ($CH_3$ as st) | 3020 | 0.1 | 3018 | 0.2 |
| B ($CH_3$ as st) | 3024 | 0.1 | 3008 | 0.2 |
| B ($CH_3$ as-s st) | 2997 | 0.6 | 2992 | 1.7 |
| A ($CH_3$ as-s st) | 3004 | 0.7 | 2989 | 0.7 |
| B (CH st) | 2944 | 3.7 | 2935 | 6.5 |
| A (CH st) | 2944 | 3.5 | 2930 | 4.4 |
| A ($CH_3$ s st) + (CH3 s st) | 2923 | 18.0 | 2920 | 25.8 |
| B ($CH_3$ s st) – (CH3 s st) | 2927 | 14.2 | 2918 | 5.0 |
| A ($CH_3$ as-s df) | 1427 | 0.1 | 1477 | 0.2 |
| B ($CH_3$ as-s df) | 1430 | 0.1 | 1429 | 0.0 |
| A ($CH_3$ as df) | 1410 | 0.0 | 1422 | 0.1 |
| B ($CH_3$ as df) | 1413 | 0.1 | 1413 | 0.0 |
| B ($C^1$–$C^2$ st – $CH_3$ s df) – A($C^1$–$C^2$ st – $CH_3$ s df) | 1356 | 2.4 | 1354 | 1.2 |
| A ($C^1$–$C^2$ st – $CH_3$ s df)+ B($C^1$–$C^2$ st – $CH_3$ s df) | 1357 | 2.0 | 1350 | 5.9 |
| B ($CH_3$ s df + $C^1$-$C^2$ st) | 1327 | 0.4 | 1330 | 0.2 |
| A ($CH_3$ s df + $C^1$-$C^2$ st) | 1328 | 0.1 | 1325 | 0.9 |

Key: as, asymmetric; s, symmetric; st, stretching; df, deformation; ro, rocking; b, bending.
[a]IR intensities in $Kmmol^{-1}$. A and B account for the bri-perp and bri-perp'structures, respectively. In red, inter-molecular coupling.

intensity close to zero (see **Table 3.3**). The outstanding difference arises from the band order. In the experimental spectrum the $CH_3$ s st mode appears at higher frequency than the CH st mode whereas it appears at a lower frequency in the simulated spectrum. This order reversal may be ascribed to the presence of the $CH_3$ s df overtone in the experiment, which, obviously, is not explicitly included in the harmonic frequency calculations. However, our calculation have confirmed that propyne adsorbs on Cu(111) on two distinct adsorption sites. Thus, it may be interesting to study how the existence on the surface of molecules adsorbed on different orientations (bri-perp and bri-perp') influences the frequencies and intensities. The exhaustive study of Chesters and McCash [8] has neglected this effect because the experimental spectrum has been performed and assigned thirteen years before the LEED pattern has been resolved [16].

In the 1300–1500 $cm^{-1}$ region, we assign the very weak feature at 1427/1430 $cm^{-1}$ to the $CH_3$ as-s st. The peak at 1357/1356 $cm^{-1}$ is the only band in this region with a significant intensity. The agreement with the experiment is excellent. Cherters and McCash [8] have assigned the feature at 1361 $cm^{-1}$ to the $C^1$–$C^2$ st. However, we assign this feature to the $CH_3$ s df coupled to the $C^1$–$C^2$ st. mode. Interestingly enough, this coupling produces two bands with very different intensities. Actually, the negative coupling (1356/1357 $cm^{-1}$, $C^1$–$C^2$ st – $CH_3$ s st) is up to eighteen times more intense than the positive coupling (1327/1328 $cm^{-1}$, $CH_3$ s st + $C^1$–$C^2$ st). Here, positive and negative refers to notation in **Figure 3.9**.

It is not easy to discuss the change in frequency upon adsorption because it is not always possible to link the vibrational modes in the adsorbed molecule to those in the gas

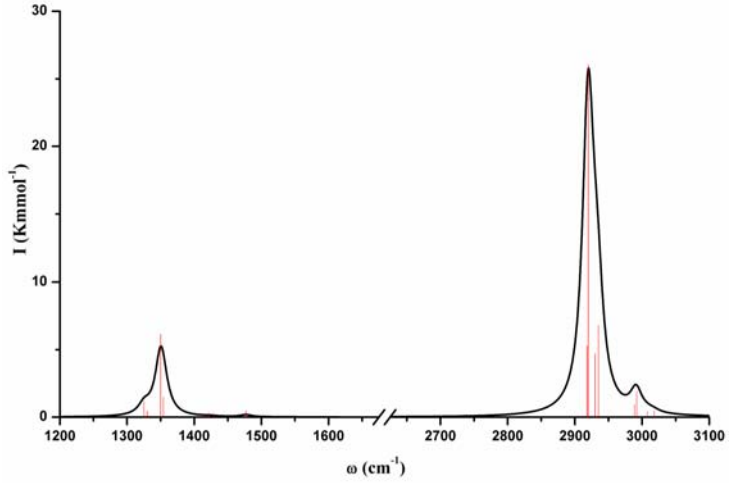


**Figure 3.10.** Simulated vibrational spectrum for propyne/Cu(111) for the 4x√3 unit cell. Obtained using Lorentzian functions, with a bandwidth of 20 $cm^{-1}$ and a resolution of 0.5 $cm^{-1}$.

phase species. However, some general trends can be observed. On adsorption there are no significant changes in the methyl stretching and deformation frequencies well in line with the absence of geometric changes. On the other hand, the CH st and the $C^1$–$C^2$ st frequencies decrease drastically (~450 and ~800 $cm^{-1}$, respectively). We can consider these differences as a measure of the activation of the C≡C bond. Computed frequencies support the $sp^2$–$sp^3$ hybridisation inferred from structural data.

After the analysis of the local modes, we will discuss the results that we obtained with the 4x√3 model. **Figure 3.10** shows the simulated vibrational spectrum. In the forthcoming paragraphs, we will focus our attention in the analysis of the possible inter-molecular couplings and the isotopic effects. There are no important changes in both frequencies and intensities in the CH stretching region except for the $CH_3$ s st mode. The coupling between the $CH_3$ s st modes of the two molecules present in the unit cell produces two bands with a very different intensity (26/5, **Table 3.3**). The intense peak corresponds to the vibrational mode where all the methyl hydrogen atoms move in the same sense and the weak feature corresponds to the normal mode where the H atoms move in the opposite sense.

The two models predict the same band order in the 2900–3100 $cm^{-1}$ region. Therefore, we can exclude that the coupling between functional group modes of molecules adsorbed in different adsorption sites causes the reverse order of the $CH_3$ s st and the CH st modes. Thus, we confirm the assignment of Chesters and McCash [8].

The results for the 1300–1500 $cm^{-1}$ region are also well in line with those obtained with the 2x√3 unit cell. The peaks at 1350/1354 $cm^{-1}$ and 1325/1330 $cm^{-1}$ are also assigned to the negative and positive coupling between the $CH_3$ s df and the $C^1C^2$ st mode. However, there is a small shift (< 7 $cm^{-1}$) of these bands to lower frequencies and, more important, the intensity of the 1350 $cm^{-1}$ feature becomes six times larger than the one of the 1354 $cm^{-1}$

**Table 3.4.** Main IR peaks (in $cm^{-1}$) for $CH_3CCD$ and $CD_3CCH$ on Cu(111):4x√3 unit cell

| vibrational | $CH_3CCD$ | | vibrational | $CD_3CCH$ | |
|---|---|---|---|---|---|
| mode | $\omega_i$ | $I_i$[a] | mode | $\omega_i$ | $I_i$[a] |
| CD st | 2157/2161 | 1.3/1.6 | CH st | 2930/2935 | 3/5 |
| $CH_3$ as st | 3008/3017 | 0.1/0.2 | $CD_3$ as st | 2224/2232 | 0.1/0.2 |
| $CH_3$ as-s st | 2989/2992 | 0.6/1.6 | $CD_3$ as-s st | 2210/2212 | 1/2 |
| $CH_3$ s st | 2918/2921 | 5/29 | $CD_3$ s st | 2097/2098 | 2/12 |
| $C^1$–$C^2$ st – $CH_3$ s df | 1342/1347 | 6/2 | $C^1$–$C^2$ st | 1345/1351 | 2/1.6 |
| $CH_3$ as df | 1413/1422 | 0/0 | $CD_3$ as df | 1014/1017 | 1/0.1 |
| $CH_3$ as-s df | 1429/1477 | 0/0.2 | $CD_3$ as-s df[b] | 1021/1060 | 0/0.3 |
| $CH_3$ s df + $C^1$-$C^2$ st | 1323/1328 | 0.4/0 | $CD_3$ s df[b] | 1046/1052 | 3/0 |

Key: as, asymmetric; s, symmetric; st, stretching; df, deformation; ro, rocking; b, bending.
[a]Intensities in $Kmmol^{-1}$. [b]the mode is coupled with the CH bi.

band. This intensity change arises from an inter-molecular coupling (see **Table 3.3**). The positive coupling (($C^1$–$C^2$ st – $CH_3$ s df) + ($C^1$–$C^2$ st – $CH_3$ s df )) increases the dipole moment change and, consequently, the intensity. Camplin *et al.* [22] have proposed that the unit cell dimensions for Cu(111) are such that the distance between two adjacent hollow sites matches that of the C≡C bond of the chemisorbed propyne. This correspondence allows the $C^1$–$C^2$ stretch to become active at expense of the methyl deformation. Our calculations confirm and complete the experimental assignment. The MSSR-inactive $C^1$–$C^2$ st becomes active because is coupled with the $CH_3$ s df (i.e. the normal mode is the sum of the two functional group modes).

Upon deuteration of the 'acetylenic' hydrogen (see **Table 3.4**), there are no significant changes in the CH st mode and the frequency shift is in good agreement with the one predicted from a simple harmonic oscillator model [34]. Moreover, our calculations predict a shift down of the peak at 1350/1357 $cm^{-1}$ of ~8 $cm^{-1}$ in good agreement with the experimental isotopic shift [8]. This result allows us to emphasize the shortcomings of band assignation based exclusively on isotopic shifts.

Upon methyl deuteration, the $CH_3$ symmetric stretching frequencies shift down but the normal modes do not change (i.e. new couplings do not appear). The picture for the $CH_3$ deformation modes is rather more complicated. The $CH_3$ asymmetric deformation modes shift down to ~1000 $cm^{-1}$ and mix with the CH bi mode (see footnotes **Table 3.4**). Besides, the 1325–1357 $cm^{-1}$ peaks change significantly. The methyl deuteration breaks the coupling between the $C^1$–$C^2$ st and $CH_3$ s df modes. Two well separated bands appear with close intensities. Although the $C^1$–$C^2$ bond is almost parallel to the metal surface, the $C^1$–$C^2$ st mode is still observed (1345/1351 $cm^{-1}$, **Figure 3.11**). The RAIR[8] and EEL[20] spectra of acetylene adsorbed on Cu(111) also exhibit a strong band at 1294 and 1307 $cm^{-1}$, respectively. These features have also been assigned to the MSSR-inactive C≡C stretch.

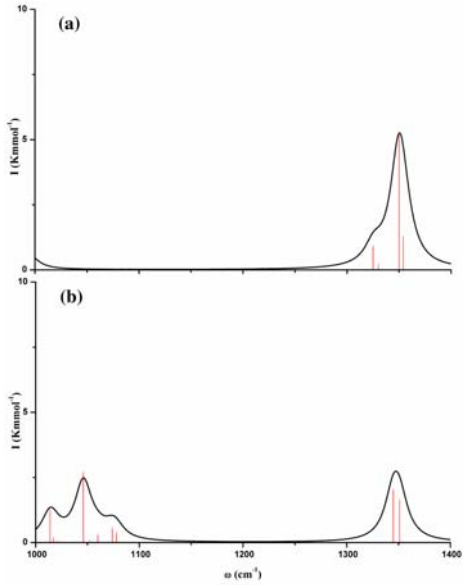


**Figure 3.11.** Isotopic effects on the simulated vibrational spectrum of propyne/Cu(111): 4x√3 unit cell. $CH_3CCH$ (a), $CD_3CCH$ (b).

*Propyne on Pt(111).* To our knowledge, the experimental spectrum of propyne on Pt(111) is not available. We present the calculated frequencies, RAIRS intensities and band assignment in **Table 3.5**. In the CH stretching region, the most intense feature is the $CH_3$ s st but $CH_3$ as and CH st have also a non negligible intensity. Interestingly enough, the band order is the same than that for the gas phase propyne (see **section 3.2**). The frequencies of the $CH_3$ stretching modes do not change significantly on adsorption but there is a great shift down of the CH st frequency. The changes in frequency are well in line with the changes in geometry.

In the 1300–1500 $cm^{-1}$, three features have a noteworthy intensity. We assign these peaks to the $CH_3$ as-s df + $C^1$–$C^2$ st (1433 $cm^{-1}$), $CH_3$ as df (1407 $cm^{-1}$) and $CH_3$ s df (1330 $cm^{-1}$). The feature at 1433 $cm^{-1}$ has its counterpart at 1355 $cm^{-1}$ ($C^1$–$C^2$ st – $CH_3$ as-s df), which has an intensity equal to zero.

Upon deuteration of the 'acetylenic' hydrogen, there are no significant changes in the normal modes (see **Appendix A.1**). Obviously, the CH st frequency is shifted to lower frequencies (2246 $cm^{-1}$). Moreover, the 1355 $cm^{-1}$ band is shifted to 1346 $cm^{-1}$. This difference indicates that the 'acetylenic' hydrogen contributes to the mode. On methyl deuteration, both the $CH_3$ st and the $CH_3$ df modes are obviously shifted to lower frequencies. Only the $CH_3$ deformation modes change in some extent. These modes shift down to the ~1000 $cm^{-1}$ region and mix with the $C^2$–$C^3$ st and CH bi modes (see **Appendix A.1**). Moreover, this frequency shift also breaks the coupling of the $CH_3$ as df modes with the $C^1$–$C^2$ st. The $C^1$–$C^2$ st mode appears at 1361 $cm^{-1}$ but its intensity is almost negligible.

**Table 3.5.** Computed frequencies (in $cm^{-1}$) for propyne ($CH_3CCH$) on Pt(111) and Pd(111): 2x2 unit cell

| vibrational | Pt(111) | | vibrational | Pd(111) | |
|---|---|---|---|---|---|
| mode | $\omega_i$ | $I_i^a$ | mode | $\omega_i$ | $I_i^a$ |
| CH st | 3049 | 1.4 | CH st | 3045 | 0.9 |
| $CH_3$ as st | 3028 | 0.6 | $CH_3$ as st | 3016 | 0.6 |
| $CH_3$ as-s st | 3011 | 2.0 | $CH_3$ as-s st | 3004 | 2.5 |
| $CH_3$ s st | 2934 | 7.2 | $CH_3$ s st | 2935 | 9.1 |
| $CH_3$ as-s df + $C^1$–$C^2$ st | 1433 | 0.7 | $CH_3$ as-s df + $C^1$–$C^2$ st | 1439 | 0.7 |
| $CH_3$ as df | 1407 | 2.0 | $CH_3$ as df | 1405 | 0.5 |
| $C^1$–$C^2$ st – $CH_3$ as-s df | 1335 | 0.0 | $C^1$–$C^2$ st – $CH_3$ as-s df | 1394 | 0.9 |
| $CH_3$ s df | 1330 | 1.6 | $CH_3$ s df | 1327 | 0.8 |

Key: as, asymmetric; s, symmetric; st, stretching; df, deformation; ro, rocking; b, bending.
[a]IR intensities in $kmmol^{-1}$.

*Propyne on Pd(111).* The computed spectrum for propyne on Pd(111) is similar to that on Pt(111) (see **Table 3.5**). In the CH stretching region, there are no major differences between the two metal surfaces in both frequencies and intensities. However, there are some significant changes in the 1300–1500 $cm^{-1}$ region. The $CH_3$ as-s df and $CH_3$ as df modes appear at 1439 and 1405 $cm^{-1}$, respectively. These two modes mix in some extent with the $C^1$–$C^2$ st (see **Table 3.5**). Moreover, we assign the 1394 $cm^{-1}$ feature to the $C^1$–$C^2$ st + $CH_3$ as-s df mode. This peak has an intensity different from zero due to the positive sign of the coupling. The peak at 1327 $cm^{-1}$ corresponds to the $CH_3$ s df mode.

Upon deuteration, the changes are analogous to those observed on Pt(111) (see **Appendix A.2**).

*Propyne on Rh(111).* The experimental HREELS spectrum of propyne on Rh(111) [14] shows five broad peaks at: 2930, 1445, 1370, 1115 and 1005 $cm^{-1}$. The 2930 $cm^{-1}$ feature is the most intense band in the spectrum. The peaks at 1445, 1370 and 1005 $cm^{-1}$ have rather similar intensities (~2/3 of the intensity of the main peak) and the 1115 $cm^{-1}$ feature is the less intense signal (~1/2 of the intensity of the 2930 $cm^{-1}$ band). Somorjai and co-workers [14] have interpreted this spectrum by comparison with the gas-phase IR spectrum of propyne. They have assigned the bands at 2930, 1445, 1370, 1115 and 1005 $cm^{-1}$ to the $CH_3$ as st, $CH_3$ as df, $CH_3$ s df, $C^1C^2$ st and $CH_3$ ro, respectively.

**Table 3.6** shows the calculated vibrational frequencies, HREELS intensities and band assignment for the two surface minima on Rh (see **section 3.3.1**): hcp-par and bri-perp'. **Figure 3.12a-b** illustrates the simulated HREEL spectra. The overall agreement between experimental and theoretical spectrum is better in the case of the hcp-par structure. The peaks at 2930, 1445 and 1370 $cm^{-1}$ appear among the frequencies of the two minima. We assign the feature at 2936/2936 $cm^{-1}$ to the $CH_3$ s st, the one at 1432/1409 $cm^{-1}$ to the $CH_3$ as df and the peak at 1330/1324 $cm^{-1}$ to the $CH_3$ s df . Here, the values correspond to the hcp-par/bri-per' minima, respectively (see **Table 3.6**). We disagree with the assignment of

**Table 3.6.** Computed frequencies (in $cm^{-1}$) for propyne ($CH_3CCH$) on Rh(111): 2x2 unit cell

| vibrational | hcp-par | | vibrational | bri-per | |
|---|---|---|---|---|---|
| mode | $\omega_i$ | $I_i^a$ | mode | $\omega_i$ | $I_i^a$ |
| CH st | 3035 | 0.2 | $CH_3$ as st | 3035 | 0.1 |
| $CH_3$ as st | 3018 | 0.2 | $CH_3$ as-s st | 3001 | 0.0 |
| $CH_3$ as-s st | 3005 | 0.6 | CH st | 2963 | 0.4 |
| $CH_3$ s st | 2936 | 2.9 | $CH_3$ s st | 2936 | 2.0 |
| $CH_3$ as-s df + $C_1$–$C_2$ st | 1432 | 0.1 | $CH_3$ as-s df | 1431 | 0.1 |
| $CH_3$ as df | 1411 | 1.1 | $CH_3$ as-s df | 1409 | 0.9 |
| $CH_3$ s df | 1330 | 1.1 | $CH_3$ as df | 1324 | 1.6 |
| $C^1$–$C^2$ st – $CH_3$ as-s df | 1323 | 0.0 | $C^1$-$C^2$ st | 1207 | 0.1 |
| $CH_3$ s ro + CH bi | 1083 | 0.2 | $CH_3$ s ro – CH bi | 1063 | 1.1 |
| CH bi – $CH_3$ s ro | 988 | 1.4 | $CH_3$ as ro | 958 | 0.3 |
| $CH_3$ s ro | 978 | 0.2 | CH bi + $CH_3$ s ro | 952 | 0.0 |
| $C^2$– $C^3$ st | 907 | 0.7 | $C^2$– $C^3$ st | 841 | 1.1 |
| CH bo | 749 | 0.8 | CH bo | 779 | 0.0 |

Key: as, asymmetric; s, symmetric; st, stretching; df, deformation; ro, rocking; b, bending.
[a]HREELS intensities computed following the experimental setting in ref 14.

the ~2930 $cm^{-1}$ band in ref [14]. However, the band intensities of the hcp-par spectra are closer to the experimental values than the ones of the bri-perp spectrum. In the latter, the peak at 1324 $cm^{-1}$ is obviously more intense than the feature at 1409 $cm^{-1}$ whereas on the experimental spectrum these two peaks have similar intensities. The bands at 1115 $cm^{-1}$ and 1005 $cm^{-1}$ are also in better agreement with the frequencies of the hcp-par structure. However, we disagree with the experimental band assignment. For the hcp-par adsorption mode, we assign the features at 1083 and 988 $cm^{-1}$ to the negative and positive coupling between the $CH_3$ s ro and the CH bi. The picture is similar for the bri-perp structure. We assign the bands at 1063 $cm^{-1}$ and 958 $cm^{-1}$ to the (CH3 s ro + CH bi) and to the $CH_3$ as ro, respectively. Actually, the differences between the experimental and the theoretical values are smaller than 32 $cm^{-1}$ for the hcp-par mode whereas they are of 52 $cm^{-1}$ and 47 $cm^{-1}$ for the bri-perp structure (see **Table 3.6**). However, the theoretical intensities do not match well with the experiment. Our calculations predict two bands with very different intensities in this region for both minima while the differences in the experimental spectrum are not so important (see below).

Besides, the spectrum of the bri-perp' surface structure has a quite strong peak at 841 $cm^{-1}$ not present in the experimental one. The differences between the experimental and the computed bri-perp' spectra are big enough to rule out this adsorption mode as the majority species on the surface but they are not sufficient to exclude its presence on the surface.

To study how the presence of these two adsorption modes on the surface can change the appearance of the spectrum, we calculated the hcp-per and bri-perp' modes co-adsorbed on a 2x4 unit cell. Unfortunately, during the geometry optimisation the bri-perp structure

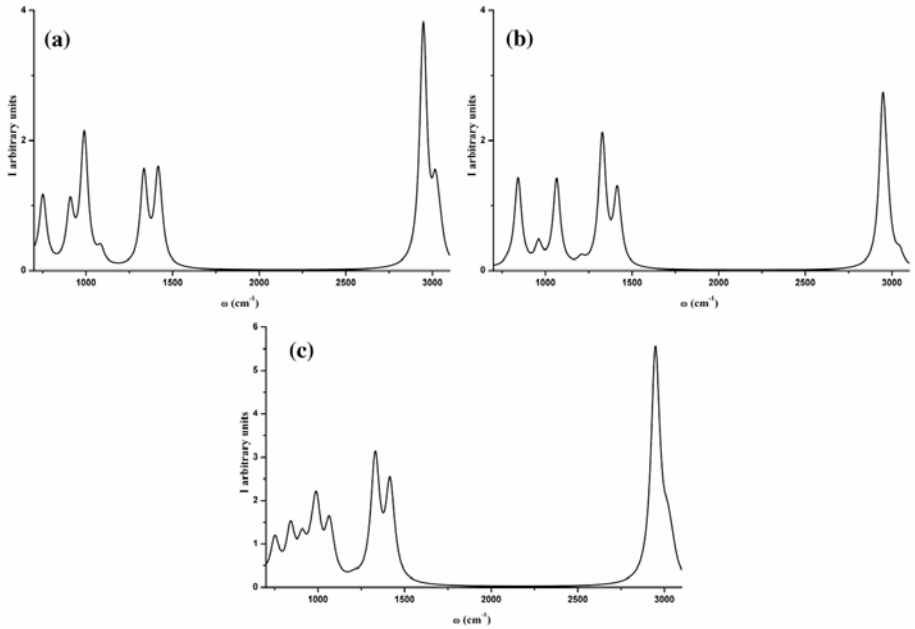


**Figure 3.12.** Simulated HREELS spectra for propyne adsorbed on Rh(111): hcp-par mode (a), bri-perp' mode (b) and sum of the spectra of the two posible surface structures.

evolved to the hcp-par mode, which indicates that this surface overlayer is not stable. The use of a large unit cell (e.g a 4x4 supercell with four adsorbed molecules) is prohibitively expensive. This is one of the shortcomings of the slab model. Thus, we simulated the vibrational spectrum as a sum of the spectrum obtained for each mode separately (see **Figure 3.12-c**). Notice that the coupling between adsorbed molecules is neglected. Moreover, the ratio hcp-par/bri-perp' is 1/1. Despite the limitations of this approximation, we observe a quite interesting conclusion. The presence of the bri-perp' structure increases the intensity of the band at ~1100 $cm^{-1}$. This fact allows us to conclude that the hcp-par structure covers the Rh(111) surface but there is a small proportion of bri-perp' adsorbed molecules. The results from the simulation of the vibrational spectra support the conclusions inferred from electronic energy calculations.

We considered it interesting to focus our attention on the MSSR-inactive $C^1$–$C^2$ st mode. For sake of comparison, we analyse the changes in the RAIRS intensities. For the hcp-par structure, this mode appears at 1323 $cm^{-1}$ coupled with the $CH_3$ as df. For the bri-perp adsorption mode, it appears at 1207 $cm^{-1}$. For both minima, the $C^1$–$C^2$ st has an intensity close to zero (< 0.1 $kmmol^{-1}$). Upon methyl deuteration, the normal mode changes but frequencies do not (differences < 5 $cm^{-1}$). Only the intensity of the bri-perp' $C^1$–$C^2$ st increases slightly (up to ~ 0.3 $kmmol^{-1}$).

In the first place, we compare the spectra of the hollow parallel structures (Pt, Pd and Rh). We do not observe important differences in the CH stretching region. On the 1300–1500 $cm^{-1}$ range, we focus our attention on the $C^1$–$C^2$ st mode. We observe that the $C^1$–$C^2$ stretch couples with the $CH_3$ asymmetric deformation in all the cases. Upon methyl deuteration, this coupling disappears but the changes in both intensities and frequencies are not very important. The $C^1$–$C^2$ st mode appears at 1361 $cm^{-1}$ for Pt, 1410 $cm^{-1}$ for Pd and 1325 $cm^{-1}$ for Rh. These values are in good agreement with the molecular distortion predicted by our calculations (see **Figure 3.5**). Unfortunately, the intensity of this feature is almost zero and it cannot be used to identify the adsorption structure from experiments.

For the bri-perp minima (Cu and Rh), there are no outstanding differences in the 2900–3100 $cm^{-1}$ region. On the other hand, the $C^1$–$C^2$ st couples strongly with the $CH_3$ s df on Cu whereas this mode is almost pure on Rh. On methyl deuteration, the coupling observed on Cu disappears. The $C^1$–$C^2$ st appear at 1357 $cm^{-1}$ on Cu and 1203 $cm^{-1}$ on Rh. Again, calculated frequencies are well in line with predicted geometries.

Finally, we compare the hollow-par spectra with the bri-perp results. There are considerable differences. In the spectra of the hollow-par minima the CH st appears at higher frequencies than in that of bri-perp structures. This is not surprising because propyne is more activated in the bri-perp adsorption modes (i.e. the distortion energy of the molecules is higher than in the hollow parallel minima).

However, the intensity of the $C^1$–$C^2$ st mode illustrates the most remarkable difference. Notice that we compare the spectra for $CD_3CCH$. For hollow parallel modes this feature is not active (intensity < 0.1 $kmmol^{-1}$). On the other hand, for bri-per structures this mode is active. The intensity of the $C^1$–$C^2$ st is very low for propyne on Rh but it is quite important on Cu. In the former, the molecule interacts predominantly with the d-band while in the latter the sp-band plays the main role. The delocalised nature of the sp electrons may increase the electronic density around the $C^1$–$C^2$ and cause this mode to be infrared active. McCash and co-workers [4,8] proposed that for acetylene on Cu(111) the changes in the electron density in the C≡C bond due to its stretching mode are enough to make this mode MSSR-active.

## 3.4 Conclusions

We studied the adsorption of propyne on the (111) surface of Cu, Pt, Pd and Rh by means of DFT periodic calculations. We investigated several possible adsorption modes and determined that the most stable adsorption geometry is the bridge-perpendicular configuration (di-σ/di-π) for Cu(111) and the hollow-parallel adsorption mode (di-σ/π) for Pt(111), Pd(111) and Rh(111). Besides, on the Rh(111) surface we found that the bri-perp structure is close in energy to the most stable one. Our results are in agreement with the experimental data available.

We explained the variation of the adsorption energies on Cu (–98 $kJmol^{-1}$), Pt(–197 $kJmol^{-1}$), Pd(–161 $kJmol^{-1}$) and Rh (–226 $kJmol^{-1}$) and the exceptional behaviour of Cu(111) in terms of geometric distortions and electronic interaction.

The decomposition of the adsorption energy in its main contributions was not conclusive but shed light on the reasons for the different reactivity of propyne on these surfaces. The strong interaction of propyne with Pt and Rh favours probably its decomposition. However, on Pd(111) and Cu(111) further analysis of the reaction intermediates and possible reaction pathways is necessary to understand the differences observed.

The analysis of the projected density of states (PDOS) allowed us to conclude that the interaction between the π system of propyne and the d-band of the metal is better on Rh, than on Pt, than on Pd, than on Cu, because of the filling and shape of the d-band. We also observed that propyne mainly interacts with the sp-band of Cu. These findings helped us to understand the trends in adsorption energies and the unique behaviour of Cu. We attributed the singular adsorption behaviour of propyne on Cu to the high degree of overlap of Cu 4s band with the π antibonding orbitals of propyne.

For propyne on Cu and Rh, calculated vibrational spectra permitted us to reproduce the experimental spectra with a very good fit. Computed frequencies confirm the results obtained from electronic energy calculations. We corroborate the presence of the MSSR-inactive C≡C stretching mode in the spectrum of propyne on Cu and give and explanation for this result. The C≡C st mixes with the $CH_3$ s df. This coupling causes an increase of the dynamic dipole moment perpendicular to the surface. On methyl deuteration, this coupling disappears but the changes in the electron density near the C≡C are enough to create a significant dipole moment perpendicular to surface. Consequently, the mode is IR active. Moreover, on Rh the analysis of the simulated spectrum and the comparison with the HREELS data led to a co-adsorption of propyne in both surface structures (hcp-par and bri-perp'), with larger proportion of the hollow parallel adsorption mode. Calculations also allowed us to predict the vibrational bands for propyne on Pt(111) and Pd(111).

### 3.5 References and Notes

[1] J. Ryczkowski, *Cat. Today* 68 (2001) 263.
[2] N. Sheppard, *Ann. Rev. Phys. Chem.* 39 (1988) 589.
[3] P. Hollins, J. Pritchard, *Prog. in Surf. Sci.* 19 (1985) 275.
[4] E.M. McCash, Surface Chemistry, Oxford University Press Inc., New York (2001).
[5] D.P, Woodruff, T.A. Delchar, *Modern Techniques of Surface Science*, 2ond Ed., Cambridge Solid State Science Series, Cambridge University Press, Cambridge (1994).
[6] N. Shepard, C. De La Cruz, *Cat. Today* 70 (2001) 3.
[7] I.N. Levine, *Molecular Spectroscopy*, John Wiley &Sons, Inc., New York (1975) 268.
[8] M.A. Chesters, E.M. McCash, *J. Elec. Spec. Relat. Phenom.* 44 (1987) 99.
[9] A. Markovits, M. García-Hernández, J.M. Ricart, F. Illas, *J. Phys. Chem. B* 103 (1999) 509.
[10] R.G. Greenler, *J. Chem. Phys.* 44 (1966) 310.
[11] H.A. Pearce, N. Sheppard, *Surf. Sci.* 59 (1976) 205.
[12] T. M. Gentle, E.L. Muetterties, *J. Phys. Chem.* 87 (1983) 2469.
[13] J.W. Peck, D.I. Mahon, B.E. Koel, *Surf. Sci.* 410 (1998) 200.
[14] B.E. Bent, C.M. Mate, J.E. Crowell, B.E. Koel, G.A. Somorjai, *J. Phys. Chem.* 91(1987)1493.
[15] R.L. Middleton, R.M. Lambert, *Catal. Lett.* 59 (1999) 15.

[16] R.L. Toomes, R. Lindsay, P. Baumgärtel, R. Terborg, J.-T. Hoeft, A. Koebbel, O. Schaff, M. Polcik, J. Robinson, D.P. Woodruff, A.M. Bradshaw, R.M. Lambert, *J. Chem. Phys.* 112 (2000) 7591.
[17] A. Clotet, J.M. Ricart, F. Illas, G. Pacchioni, R.M. Lambert, *J. Am. Chem. Soc.* 122 (2000) 7573.
[18] C.J. Ennis, P.A. Carr, E.M. McCash, *Surf. Sci.* 539 (2003) L574.
[19] R.J. Koestner, J.C. Frost, P.C. Stair, M.A. van Hove, G.A. Somorjai, *Surf. Sci.* 116 (1982) 85.
[20] B.J. Bandy, M.A. Chesters, M.E. Pemble, G.S. MacDougall N. Shepard, *Surf. Sci.* 139 (1984) 87.
[21] A.J. Roberts, S. Haq, R. Raval, *J. Chem. Soc. Faraday Trans.* 92 (1996) 4823.
[22] J.P. Camplin, J.K. Eve, E.M. McCash, *Phys. Chem. Chem. Phys.* 2 (2000) 4433.
[23] M.I. El Idrissi, J. Liévin, M. Herman, A. Campargue, G. Graner, Chem. Phys. 265 (2001) 273.
[24] T.Shimanouchi, *Tables on Molecular Vibrational Frequencies*, National Standard Reference Data Series, National Bureau of Standards, Washington, DC (1972) and references therein.
[25] A.Clotet, G. Pacchioni, *Surf. Sci.* 346 (1996) 91.
[26] We used a 4x√3 unit cell and a 2x√3 model.
[27] J. W. Medlin, M.D. Allendorf, *J. Phys. Chem. B* 107 (2003) 217.
[28] F. Delbecq, P. Sautet, *J. Catal.* 211 (2002) 398.
[29] F. Mittendorfer, C. Thomazeau, P. Raybaud, H. Thoulhoat, *J. Phys. Chem. B* 107 (2003) 12287.
[30] C. J. Baddeley, A. F. Lee, R. M. Lambert, T. Giessel, O. Schaff, V. Fernandez, K. -M. Schindler, A. Theobald, C. J. Hirschmugl, R. Lindsay, A. M. Bradshaw, D. P. Woodruff, *Surf. Sci.* 400 (1998) 166.
[31] M. Mavrikakis, J. Rempel, J. Greeley, L.B. Hansen, J.K. Norskov, *J. Chem. Phys.* 117 (2002) 6737.
[32] A. Gil, A. Clotet, J.M. Ricart, G. Kresse, M. García-Hernandez, N. Rösch, P. Sautet, *Surf. Sci.* 530 (2003) 71.
[33] R. Hoffmann, *Angew. Chem. Int. Ed. Engl.* 26 (1987) 846.
[34] Isotopic factor, ωD/ωH= 1.35–1.39.

# 2

# Method and model

*A detailed knowledge of catalysis and surface chemistry at a molecular level is crucial to understanding chemical processes. Theoretical simulations can provide a better interpretation of experimental results and provide information that cannot be obtained or is difficult to obtain experimentally. The last few years have seen enormous improvements in computer capacity and speed. There is now a wide and increasing variety of methods in Computational Chemistry. We are able to perform electronic structure calculations on models of sufficient size to represent the 'chemistry' occurring at surfaces. Computational Chemistry tools can reliably predict interaction energies, geometric structures and electronic properties.*

*This chapter is organised as follows: section 2.1 introduces the Born-Oppenheimer approximation; section 2.2 summarises the basic principles of Density Functional Theory; section 2.3 describes the common strategies for dealing with infinite systems; section 2.4 briefly explains pseudopotential approximation; section 2.5 summarises the key features of the program used to perform the calculations, VASP; section 2.6 discusses the fundamental principles of RAIRS and HREELS spectroscopies and develops the approximations used in this thesis to simulate the vibrational spectra; section 2.7 describes the transition state search algorithms currently available in VASP and the strategies used in this thesis to find saddle points; section 2.8 discusses the calculation of the Density of States; section 2.9 summarises the approximations used to construct the pressure and temperature phase diagrams and section 2.10 presents and discusses some computational details of this thesis.*

## 2.1 Born-Oppenheimer approximation

The *Schrödinger equation* is the key equation of the science of quantum mechanics. This equation, developed by the physicist Erwin Schrödinger in 1925-26, has the same central importance to quantum mechanics as Newton's laws of motion have to the large-scale phenomena of classical mechanics.

For a system composed of *N* electrons and *M* nuclei, it is expressed as:

$$\hat{H}\Psi_n\left(\{\vec{r}_i\}\{\vec{R}_\mu\}\right) = E_n\Psi_n\left(\{\vec{r}_i\}\{\vec{R}_\mu\}\right) \qquad (2.1)$$

where $\hat{H}$ is the time-independent Hamiltonian, $\Psi_n$ is the wave function of the system associated to the energy level $E_n$ (*n* accounts for the quantisation of the system) and $\vec{r}_i$ and $\vec{R}_\mu$ are the spatial coordinates of the electrons and the nuclei, respectively. All the properties of the electron-nuclei system are described by **equation 2.1** (except for relativistic effects). By solving this equation we therefore obtain all the physico-chemical properties of the target system. Unfortunately, this involves dealing with a system of *(N+M)* interacting particles. Even for a very small system, this process is too complex to solve (even numerically!). To solve the Schrödinger equation, therefore, several approximations are needed.

For systems with many variables, a common way to simplify complicated equations is to separate the variables. One such separation step, universally accepted in electronic structure theory, is the separation of nuclear and electronic motion—the so-called *Born-Oppenheimer approximation* [1]. This approximation is based on the difference in mass between nuclei and electrons. The lightest nucleus, the one of the hydrogen atom, is actually 1,836 times heavier than an electron. We can therefore consider nuclear and electronic motion as independent. Electrons follow nuclei instantaneously during the motion of the latter, i.e. they change their wave function very quickly with respect to the timescale of nuclei. We can then rewrite the expression for the Hamiltonian as

$$\hat{H} = \hat{T}_{nuc} + \hat{H}_{el} \tag{2.2}$$

The electronic Hamiltonian $\hat{H}_{el}$ depends parametrically on nuclear positions ($R_\mu$): the nuclear coordinates appear in the electronic Hamiltonian, but derivatives with respect to these coordinates do not. Therefore, the electronic problem can be solved for nuclei that are momentarily fixed in space.

$$\hat{H}_{el}(r,R)\psi_{el}(r,R) = E_{el}(R)\psi_{el}(r,R) \tag{2.3}$$

*R* and *r* are the total set of nuclear and electronic coordinates. The total wave function can then be approximated as a product

$$\Psi_{BO}(r,R) = \psi_{nuc}(R)\psi_{el}(r,R) \tag{2.4}$$

where the nuclear wave function $\psi_{nuc}(R)$ is a solution to the equation

$$\{\hat{T}_{nuc}(R) + E_{el}(R)\}\psi_{nuc}(R) = E\psi_{nuc}(R) \tag{2.5}$$

Separation of the electronic and nuclear wave functions clearly simplifies the resolution of the Schrödinger equation. The determination of the total wave function of the system nuclei plus electrons is reduced to the determination of the total electronic wave function. However, for systems with hundreds or even thousands of electrons the electronic part of the problem is too complicated to be treated exactly.

First-principle quantum chemical methods are intended to solve *ab initio* (‘from scratch’) the electronic Schrödinger equation. *Ab initio* methods include wave function methods—e.g. Hartree-Fock (HF), Configuration Interaction (CI) theory, Perturbation theory (PT) and coupled Cluster Methods (CC)—and Density Functional Theory (DFT) methods [2–7]. The former, which can provide extremely accurate results if a high level of Configuration Interactions is included, are limited to 10–100 electrons because of the great scaling with the system size. For transition metal surfaces its application is therefore restricted to quite small systems (tens of atoms). This usually makes these methods

unattractive to model transition metal catalysts. In fact, in surface science and catalysis they are mainly used as benchmarks [8] that can be used to gauge the accuracy of less computational-time-demanding DFT methods. Density Functional Theory has therefore been used for the calculations in this thesis. In the next section we briefly report the bases of this method.

## 2.2 Density Functional Theory

In the mid 1920s, Thomas and Fermi [9] made a crucial advance towards the resolution of the electronic Hamiltonian. They established that the energy of a homogeneous electron gas is a function of its electronic density. In 1964, Hohenberg and Kohn [10] showed that this principle can be generalised to any kind of electronic system and established the basis of *Density Functional Theory* (DFT). For a system of N electrons and M nuclei, the electronic Hamiltonian can be written as

$$\hat{H} = \hat{T} + \hat{V} + \hat{W} \tag{2.6}$$

The first term in equation (**2.6**), $\hat{T}$, is the kinetic energy arising from the motion of electrons, the second term is the potential energy of the nuclear-electron attraction, $\hat{V}$, and the third term is the electron-electron repulsion, $\hat{W}$.

Hohenberg and Kohn proved that the ground-state molecular energy, wave function, and all other molecular properties are uniquely determined by the exact electron density, $\rho(\vec{r})$. Therefore, the central focus of DFT is the electronic density, $\rho$, rather than the wave function, $\psi$. If N is the number of electrons, the density function, $\rho(\vec{r})$, is defined by

$$\rho(r) = N \int ... \int |\psi|^2 ds_1 dr_2 ... dr_N \tag{2.7}$$

where $\psi$ is the electronic wave function of the system. Then

$$\int \rho(r) dr = N \tag{2.8}$$

DFT is based on two main theorems, the first and second *Hohenberg-Kohn theorems:*

***Theorem 1****. The external potential $\hat{V}$ is a unique functional of $\rho$; since V fixes the Hamiltonian, the particle ground state is a unique functional of $\rho$. Therefore, there is a direct relationship between the electronic density and the energy (and its individual parts).*

$$E[\rho] = T[\rho] + V[\rho] + W[\rho] \tag{2.9}$$

$$V[\rho] = \int \rho(r) v(r) dr \tag{2.10}$$

***Theorem 2***. *For a trial density* $\rho(\vec{r})$ *, such as* $\rho(\vec{r}) \geq 0$ *and* $\int \rho(r)dr = N$ , $E_0[\rho_0] \leq E[\rho]$. *In other words, the energy of the system* $E[\rho]$ *reaches a minimum value* $E_0$ *for the exact density* $\rho_0$ *. This is the so-called variational principle.*

If we take a closer look at equation (**2.9**), we can separate the $W[\rho]$ functional into two contributions: the classic interaction between two charge densities (Coulomb) and a second term that contains the non-classical parts (**eq. 2.11**).

$$W[\rho] = \frac{1}{2}\iint \frac{\rho(\vec{r}_1)\rho(\vec{r}_2)}{r_{12}} d\vec{r}_1 d\vec{r}_2 + W_{NCL}[\rho] = W_{CL}[\rho] + W_{NCL}[\rho] \tag{2.11}$$

The complete energy functional can be expressed as

$$E[\rho] = T[\rho] + V[\rho] + W_{CL}[\rho] + W_{NCL}[\rho] \tag{2.12}$$

In equation (**2.12**) only the $V[\rho]$ and $W_{CL}[\rho]$terms are known. To solve the problem of the kinetic energy functional, this term is split into two contributions: $T_s[\rho]$and $T_C[\rho]$. The former is expressed as a one-particle approach (**2.13**) and the latter, still unknown, contains the difference between the real functional and the one particle term.

$$T_S[\rho] = \frac{1}{2}\sum_i \left\langle \psi_i \middle| \nabla^2 \middle| \psi_i \right\rangle \tag{2.13}$$

Equation (**2.12**) can be rewritten as follows

$$\begin{aligned} E[\rho] &= T_S[\rho] + T_C[\rho] + V[\rho] + W_{CL}[\rho] + W_{NCL}[\rho] \\ &= T_S[\rho] + V[\rho] + W_{CL}[\rho] + E_{XC}[\rho] \end{aligned} \tag{2.15}$$

where the $E_{XC}[\rho]$or *exchange-correlation functional* contains all the unknown terms (all the many-body interactions).

Unfortunately, the Hohenberg and Kohn theorems do not tell us how to calculate $E_0$ from $\rho$ since the exact form of the functional is not known. Kohn and Sham [11] invented an indirect approach to this functional. In the *Kohn-Sham method*, the exact ground state can be found from the Kohn-Sham orbitals,

$$\rho(r) = \sum_i |\psi_i(r)|^2 \tag{2.16}$$

The Kohn-Sham orbitals are obtained from the one-electron Kohn-Sham equations

$$f_S^{KS}\psi_i = \varepsilon_i\psi_i \tag{2.17}$$

where $f_S^{KS}$ is

$$f_S^{KS} = -\frac{1}{2}\nabla^2 - \int \frac{\rho(\vec{r}_2)}{r_{12}}d\vec{r}_2 + \sum_\mu \frac{Z_\mu}{r_{1\mu}} + v(r) \tag{2.18}$$

These equations are solved iteratively. Thus, we propose a guess density, which is used to build the $f_S^{KS}$, then we solve the set of equations (**2.17**) and obtain a new density, which is used to build a second $f_S^{KS}$, until self-consistency is reached. No one knows what the exact functional $E_{XC}[\rho]$ is. Finding the analytical expression of the exchange-correlation term is a major task in DFT. Some approximate functionals have been proposed.

### 2.2.1 The exchange-correlation functional

To describe $E_{XC}[\rho(r)]$, two approximations are generally used: the *Local Density Approximation* (LDA) and the *Generalised Gradient Approximation* (GGA).

LDA is based on a model called uniform electron gas [9]. This approximation assumes that the charge density varies slowly throughout a molecule so that a localised region of the molecule behaves like a uniform electron gas. The exchange-correlation energy is then expressed as a function of the exchange-correlation functional per particle of a uniform electron gas, $\varepsilon_{XC}$.

$$E_{XC}^{LDA}[\rho(r)] = \int \rho(r)\varepsilon_{XC}[\rho(r)]dr \tag{2.19}$$

The energy functional accounts for the local value of $\rho$ at each point in space regardless of any other point. Vosko, Wilk and Nusair (VWN) [12] reported the first analytic expression for the correlation term within this approximation.

GGA adds an additional term to the LDA exchange-correlation energy. Gradient corrections are introduced to allow exchange-correlation functional to vary (the density gradient is taken into account). $E_{XC}[\rho(r)]$ is expressed as

$$E_{XC}^{GGA}[\rho(r)] = \int f_{XC}(\rho(r), |\nabla\rho(r)|)\rho(r)dr \tag{2.20}$$

There are many exchange-correlation expressions in the literature, e.g. Perdew (P86), Becke (B86, B88), Perdew-Wang (PW91), Laming-Termath-Handy (CAM) and Perdew-Burke-Enzerhof (PBE) for the exchange part and Perdew (P86), Lee-Yang-Parr (LYP), Perdew-Wang (PW91) and Perdew-Burke-Enzerhof (PBE) for the correlation term [13].

There is a third class of functionals in DFT called *hybrid functionals*, like the popular B3LYP [14] exchange-correlation functional. These include the exact exchange energy as a contribution from the exact exchange. This approach has extensively proven its accuracy for many systems, although they are more time-demanding than *non-hybrid* exchange-correlation functionals because of the calculation of the two-electron integrals in the exact exchange.

We chose the PW91 exchange-correlation functional for all the calculations performed in this thesis because of its good description of the chemical bond [15].

If the exact form of $E_{xc}$ is unknown, one cannot say very much about the performance of a new functional until it is tested with different chemical systems. The exchange-correlation functional is still the most restrictive approximation in DFT calculations. Unfortunately, other approximations are needed to cope with the systems studied in this thesis (hydrocarbons on transition metal surfaces).

## 2.3 Periodic calculations

Metal crystals have an infinite number of atoms. Working with a system with an infinite number of atoms implies that the wave function has to be calculated for each of the infinite number of electrons and the basis set in which the wave function is expressed will be also infinite. In this section we briefly describe how to overcome these difficulties.

### 2.3.1 Modelling a periodic system

We are essentially interested in metallic surfaces. These bi-dimensional systems can be modelled by two different approaches: the finite, or the so-called *cluster model approach* [16–19], and the *periodic* or *slab model* [17,20]. Although finite models have extensively proven their ability to describe local properties [21–23], we chose periodic models to perform the calculations in this thesis because of the poor convergence of adsorption energies with respect to cluster size and the need to use a considerably large cluster in order to avoid undesirable edge effects.

The slab model is based on the band-structure theory. A bi-dimensional slab is formed by periodically repeating the geometry of the system on the x and y axes. In the third direction (z axes), the periodicity is broken to create the surface. Depending on the basis set used in the periodic calculation, this slab is further repeated in the direction perpendicular to the surface with a large vacuum width between the repeated slabs (see **Figure 2.1**). This periodic approach avoids problems related to the artificial cluster boundaries, once the limitations associated with the model's finite number of layers are under control. Another advantage of supercell models is that they are well suited to studying the influence of the adsorbates coverage on the surface. However, to study low coverage situations with slab models we need to use large supercells, with a concomitant increase in computational costs.

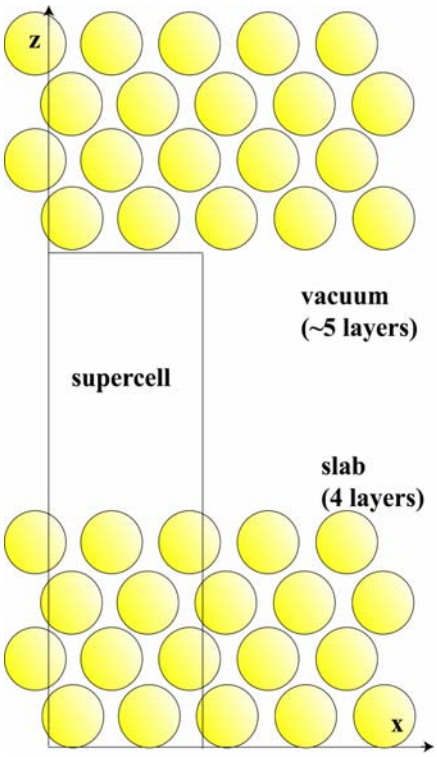


**Figure 2.1.** Sketch of the slab model. For sake of simplicity, only x and z directions are shown.

### 2.3.2 Bloch's theorem and the plane wave basis set

In a perfect metallic crystal, atoms are arranged in a regular way. The repeated units of the system are all identical and can be obtained by simple repetition of the unit cell [24]. This means that the Hamiltonian $\hat{H}$ has to commute with the translation operator $\hat{T}$

$$\left[\hat{H},\hat{T}\right]=0 \tag{2.21}$$

*Bloch's theorem* [25] uses the periodicity of the crystal to reduce the infinite number of the one-electron wave function s to be computed to the number of electrons in the unit cell of the crystal. Then we can express the one-electron wave function s as the product of a cell periodic part and a wave-like part (*Bloch functions*)

$$\psi_{n,\vec{k}}(\vec{R}) = \exp i(\vec{k}\cdot\vec{R})\phi_{nBAND,\vec{k}}(\vec{R}) \tag{2.22a}$$

where $\psi_{n,\vec{k}}$ is the wave function of the periodic system, $\vec{R}$ is the position in the crystal, $\vec{k}$ is a vector of the reciprocal space of the crystal and $\phi_{nBAND,\vec{k}}(\vec{R})$ is a periodic function associated with a band $n_{BAND}$ (or 'energy level' for periodic systems), which has the same periodicity of the system. The problem is then transferred from the real to the reciprocal space. The infinite number of electrons is now mapped onto the problem of expressing the wave function in terms of an infinite number of reciprocal space vectors within the first Brillouin zone [26], $\vec{k}$ . Unfortunately, we cannot deal with an infinite number of $\vec{k}$ . We can solve this problem by sampling the Brillouin zone at special sets of k-points. The k-points sample can be calculated by various methods. The most popular ones are the Monkhorst-Pack method [27] and the Chadi-Cohen [28] method.

The total wave function at each k-point can be expressed in terms of a discrete plane-wave basis set (3D-Fourrier series)

$$\psi_{n,\vec{k}}(\vec{R}) = \sum_{\vec{g}} a_{nBAND,\vec{g},\vec{k}} \exp i(\vec{g}+\vec{k})\vec{R} \tag{2.22}$$

In principle this set is infinite but we can consider it converged for large values of $\left|\vec{g}+\vec{k}\right|$. Introducing a plane-wave energy cut-off $\left|\vec{g}+\vec{k}\right| < G_{cut-off}$ reduces the basis set to a finite size. This energy cut-off value depends on the system one is working with. Therefore, it is strictly necessary to test the convergence of the energy for a given cut-off value. Moreover, the use of plane-waves forces us to describe the vacuum with the same accuracy as the regions of high electronic density (atoms). Usually a large number of plane waves are necessary.

Using pseudopotentials reduces the $E_{cut-off}$ and, consequently, the size of the expansion.

### 2.4 Using Pseudopotentials. The PAW method

Working with transition metals involves dealing with a large number of electrons, so the computational time increases exponentially as the system size increases. 'Luckily', the chemical bond does not strongly depend on the core electrons. In fact, only the bonding energy is affected by the average electrostatic potential generated in the vicinity of the core. The aim is then to model the core electrons and their interaction with the other electrons.

The concept of *pseudopotential* dates from the 1930s, when Fermi and Hellmann proposed solving the Schrödinger equation for the valence electrons in the subspace orthogonal to the core electrons. This concept was extended and led to the development of

pseudopotential methods such as 'norm-conserving' pseudopotentials [29], ultra-soft pseudopotentials (US-PP) [30] and the Projector Augmented Wave (PAW) method [31].

The PAW method, introduced by Blöchl, is built on projector functions that allow the complicated wave functions to be mapped onto 'pseudo' wave functions, which are easier to treat computationally. With this method, we model the core electrons taking the difference between the 'true' wave function and a pseudo-wave function obtained and neglecting the core electrons. The Schrödinger equation is then expressed as

$$\tau^* H \tau \tilde{\Psi} = E \tau^* \tau \tilde{\Psi} \tag{2.23}$$

where $\tilde{\Psi}$ is the pseudo wave function and $\tau$ is the operator of transformation that connects the exact wave function ($\Psi$) and the pseudo-wave function ($\tilde{\Psi}$).

In DFT, we solve the Schrödinger equation to determine the 'pseudo'-wave functions. Projectors then enable us to obtain the exact density (whenever the basis set expansion is complete).

The PAW method has extensively proven its high performance for studying molecules, surfaces and solids. We therefore used these pseudopotentials to perform our calculations.

## 2.5 The VASP code

The program VASP (Vienna *Ab initio* Simulation Package), developed by G. Kresse, J. Furthmüller and J. Hafner [32], has been used for all the calculations in this thesis. This code applies DFT to periodical systems, using plane waves and pseudopotentials. VASP includes an optimised set of US-PP and PAW potentials for all elements of the periodic system.

In VASP, the Kohn-Sham equations are solved self-consistently with an iterative matrix diagonalisation combined with the Broyden/Pulay mixing method [33,34] for charge density. Combining these two techniques makes the code very efficient, especially for transition metal systems that present a complex band structure around the Fermi level. The algorithms implemented in VASP are based on the conjugate gradient scheme, the block Davidson scheme or a residual minimisation scheme (RMM). These algorithms work as follows: they calculate the electronic ground state for a given geometry, calculate forces, and then, based on these forces, predict a new geometry. These steps are then repeated until an energy convergence criterion is reached. A special algorithm is the *quasi*-Newton, where the energy criterion is ignored and only the forces are minimised. A detailed description of the algorithms implemented in VASP can be found in references [35,36].

The Hamiltonian is determined in pieces in direct and reciprocal space. Fast Fourrier Transformations (FFT) are used to switch from direct to reciprocal space and *vice-versa*. This allows for partial diagonalisation.

Besides the pure local density approximation LDA, several gradient-corrected functionals are implemented in VASP to account for the non-local in the exchange-correlation (BP, PW91, PBE).

The number of k-points in the irreducible part of the Brillouin zone is crucial for accurately integrating the properties computed. The k-points sample is usually calculated by the program using the Monkhorst-Pack method [27]. To improve the convergence with respect the k-points sampling, several techniques can be used: the linear tetrahedron method, smearing methods such as finite temperature approaches or improved functional form (Methfessel and Paxton method [37], and finite methods such as gaussian or fermi smearing).

Transition state structures and energies can also be found by various techniques (NEB, Dimer method) implemented in the VASP code. Frequencies and normal modes can also be calculated with this code. Unfortunately, intensities cannot be directly computed.

Further information about VASP can be found at:
http://cms.mpi.univie.ac.at/vasp/vasp/vasp.html.

## 2.6 Vibrational analysis

### 2.6.1 Experimental Techniques

Vibrational data on the adsorbates have been widely used to determine the bonding pattern of the adsorbed species, including what sort of site the adsorbate has adopted. It is also very useful for providing valuable information about any fragmentation or reaction that has taken place. Two main techniques have been developed for studying vibrations of adsorbed species on single-crystal metallic surfaces: high-resolution electron energy loss spectroscopy, HREELS (or vibrational EELS, VEELS) and reflection adsorption infrared spectroscopy, RAIRS. We can find detailed and accurate descriptions of these techniques in references [38–42]. Here we will only sketch the most important points.

#### 2.6.1.1 Reflection Adsorption Infrared Spectroscopy (RAIRS)

The application of IR techniques to surfaces owes much of its early development to the work of Eichens, Sheppard and Greenler. Reflection-adsorption infrared spectroscopy (RAIRS) allows for the study of metallic films, single crystals and opaque solids by reflection. This technique has also proved to be a particularly powerful research tool for studying adsorbed phases on metal surfaces. Greenler [43] was the first to demonstrate that the absorption of IR radiation by adsorbates on metallic films is enhanced at high angles of incidence. **Figure 2.2** illustrates the plane of incidence (which contains the incident and the reflected rays and the surface normal), and the so-called *s* (perpendicular to the plane of incidence) and *p* (parallel to the plane of incidence) components of the radiation. At the interface, the p-polarised radiation has a net amplitude almost twice that of the incident radiation (p+p').On the other hand, for s-polarised radiation the incident and emitted rays (s and s') undergo a 180º transformation with respect to each other, so the net amplitude of the radiation parallel to the surface is zero. As a result, only vibrations with a component of the dynamic dipole that is polarised in the direction normal to the surface can be observed in RAIRS.

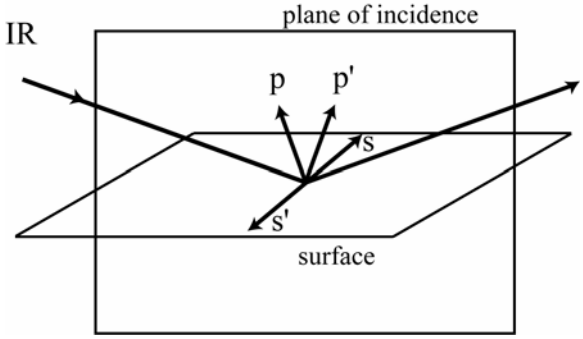


**Figure 2.2.** Definition of the s and p polarised radiation in the RAIRS experiment.

The IR spectrum of an adsorbate is recorded by tacking a single reflection of an infrared beam at high angles of incidence and taking the ratio of the resulting spectrum to the spectrum obtained for the reflection off the clean surface. The presence of the adsorbate causes small changes in reflectivity at the frequencies of the adsorbate vibrations, where IR radiation is absorbed.

Surface IR spectroscopy can be performed only if the substrate does not absorb strongly. Depending on the substrate, this leads to a cut-off in the 500–1000 $cm^{-1}$ region of the spectrum. The vibrational frequencies of both substrate-adsorbate bond and surface phonons are too low to be studied by this technique.

#### 2.6.1.2 High Resolution Electron Energy Loss Spectroscopy (HREELS)

In the early 1970s, Ibach and co-workers revolutionised surface science thanks to the development of this technique as a surface probe. Early studies demonstrated that HREELS is sensitive to adsorbates with relatively weak dynamic dipoles. At that time, IR methods such as RAIRS restricted its application to molecules with large dynamic dipole moments due to the limitations of equipment and detectors. Moreover, HREELS can interrogate the low-frequency region (100–800 $cm^{-1}$), where RAIRS cannot be used.

In an EELS experiment, the energetic distribution of electrons back-scattered from a sample bombarded with low energy electrons ($E_0$, typically in the range of about 8–80 $cm^{-1}$) is measured and the energy analysis is performed around the primary energy along a given direction with respect to the surface normal (see **Figure 2.3**). The energy E (energy of the scattered electrons) at which a signal occurs is (**equation 2.24**)

$$E = E_0 - h\nu \tag{2.24}$$

where $E_0$ is the energy of the incident electrons, $h$ is the Planck's constant and $\nu$ is the frequency of the excited vibration.

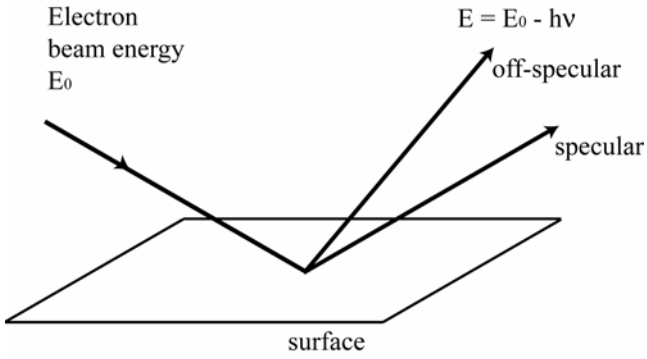


**Figure 2.3.** Schematic representation of the HREELS experiment.

To correctly interpret EEL spectra we need to know how electrons scatter inelastically. Two types of scattering of electrons can be considered (*dipole* scattering and *impact* scattering). A third mechanism in which an electron is trapped at the surface for a finite time will not be discussed here.

*Dipole scattering mechanism*

The dipole scattering mechanism is due to the long-range interaction between the electric fields from the incoming electrons and the adsorbate dipoles, which vary in magnitude during the vibration. The scattered electrons are grouped in a small angle around the specular direction. On metal surfaces, the conduction electrons screen the electric field associated with the vibration dipole inside the solid. Therefore, in a first approximation, we need to consider both the electric field generated by the dipole itself and its image underneath the metal surface—the so-called *image-charge* effect. **Figure 2.4** shows that, for an adsorbate dipole of magnitude μ oriented parallel to the surface plane, the image dipole cancels out the surface dipole such that the net dipole is null. However, for a dipole normal to the surface, the presence of the image dipole results in a reinforcement of the net dipole. Therefore, only the vibrating modes that have a component that is perpendicular to the surface are detectable, i.e. only the IR active modes. For this reason, a RAIRS spectrum and a dipolar EELS spectrum are equivalent in terms of band positions, although intensities may vary due to differences in scattering and absorption factors. The absolute intensity of energy loss peaks from the dipole scattering mechanism is expressed as [41,44]

$$\frac{I_{loos}}{I_{elastic}} = \frac{\hbar(1-\theta_E)^{1/2}}{8a_0\varepsilon_0 E_0 \cos\theta_I}\left(\frac{\delta\mu}{\delta Q_k}\right)^2 \frac{1}{\nu_k} F\left(\hat{\theta}_C\right) n_s \qquad (2.25)$$

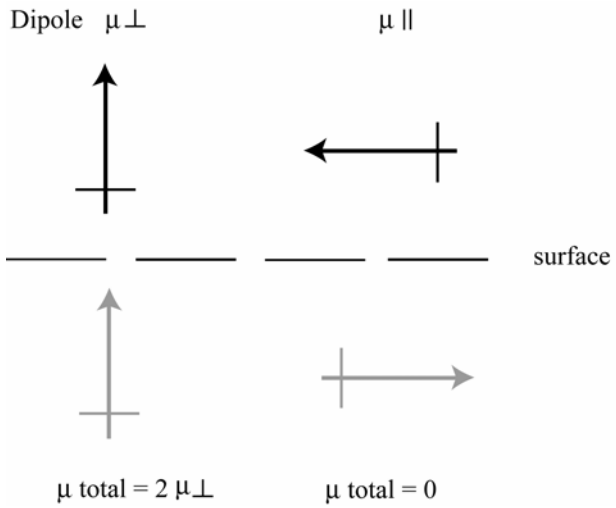


**Figure 2.4.** Image dipole at a metallic surface.

where $a_0$ is the Bohr radius, $\varepsilon_0$ is the vacuum permittivity, $E_0$ is the primary energy of the electron beam, $\theta_I$ is the incident angle, $\left(\delta\mu/\delta Q_k\right)$ are the dynamic dipole moment derivatives and $n_s$ [45] is the surface coverage. $F(\hat{\theta}_C)$, $\theta_E$ and $\hat{\theta}_C$ are defined as

$$F(\hat{\theta}_C) = \left( \frac{\hat{\theta}_C^2}{1+\hat{\theta}_C^2} (\sin^2(\theta_I) - 2\cos^2(\theta_I) + (1+\cos^2(\theta_I))\ln(1+\hat{\theta}_C^2)) \right) \qquad (2.26)$$

$$\theta_E = \frac{h\nu_k}{2E_0} \quad \text{and} \quad \hat{\theta}_C = \frac{\theta_C}{\theta_E} \qquad (2.27 \text{ and } 2.28)$$

where $\theta_C$ is the acceptance angle of the spectrometer.

*Impact scattering mechanism*

This scattering mechanism is best visualised by assuming that the incoming electron 'hits' or 'impacts' the adsorbate and is scattered by the surface atomic potentials, which are modulated at the vibrational frequencies. This mechanism is not subject to the same selection rule as dipole scattering, i.e. the rules valid for RAIRS are no longer appropriate. To determine whether a vibrational mode will lead to an impact scattered loss peak, we need to consider the orientation of the dynamic dipole with respect to the incidence plane of

**Table 2.1.** Comparative physical characteristics of the RAIRS and HREELS techniques

| | RAIRS | HREELS |
|---|---|---|
| Sample preparation | Easy | Difficult |
| Temperature range (K) | 70-600 | Ambient |
| Pressure range (mbar) | Even above atmospheric P | $\sim 10^{-6}$ |
| Resolution ($cm^{-1}$) | 0.5-8 | 20-80[a] |
| Lower limit ($cm^{-1}$) | 500-1000 | <100 |
| Information | Adsorbed species<br>Functional groups | Metal-ligand bonds |

[a] advanced spectrometers can now attain 8 $cm^{-1}$.

the electron beam (specifically to its symmetry elements). This involves group theory, which is beyond the scope of this chapter. In any case, the key point is that it is possible to detect vibrational modes that produce dynamic dipoles both perpendicular and parallel to the metal surface. Impact scattering is only observed in the off-specular direction.

RAIRS and EELS can be considered complementary techniques. **Table 2.1** summarises the main characteristics of these two techniques.

### 2.6.2 Simulation of vibrational spectra

The theoretical simulation of vibrational spectra is becoming increasingly important in catalysis research. Its uses are diverse. In this thesis we use the theoretically predicted frequencies, intensities and normal modes to corroborate dubious or ambiguous assignments, identify reactive intermediates and characterise transition states.

The vibrational frequencies and the corresponding normal modes were calculated within the harmonic approach using the VASP code. We greatly simplified the vibrational treatment by neglecting the coupling between surface phonons and adsorbate vibrations. We performed several tests to improve the description of the molecule-metal bond vibrations (frequencies below 600 $cm^{-1}$). To do this we included the two uppermost metal layers in the Hessian matrix. These calculations showed that the frequency changes were always less than 10 $cm^{-1}$ (for more details see **Chapter 3**).

In VASP, the Hessian dynamical matrix is built with finite differences of the first derivatives of the total energy by geometrical perturbation of the optimised Cartesian coordinates. To establish the step length for these numerical differences, we performed extensive tests. These displacements should be taken as large as possible to have meaningful numerical values but small enough to avoid going beyond the harmonic region. We explored the 0.005 to 0.05 Å range and established that the optimal step length $(\Delta r_i)$ was 0.02 Å. The diagonalisation of the Hessian matrix provides the adsorbate frequencies and the corresponding normal modes $Q_k$ with a matrix of weights $P_{ij}$.

To our knowledge, VASP does not compute intensities directly but provides the dynamical dipole moment at each configuration used to construct the Hessian matrix. We calculated the first derivatives of the dynamical dipole moment $\left( {d\mu}/{dQ_k} \right)$ to estimate the RAIRS and dipolar HREELS intensities for each normal mode. Note that, in RAIRS and dipolar HREELS, only vibrational modes that lead to an oscillating dipolar moment perpendicular to the surface are active. Consequently, to calculate the intensities we only considered the z-component of the dipole moment, $\mu_z$.

RAIRS intensities are directly related to the square of the first derivative of $\mu_z$ with respect to the normal mode $Q_k$. We evaluated the RAIRS intensities in the Cartesian coordinate system $(\Delta r_i)$ following

$$I^k \propto \left( \frac{d\mu_z}{dQ_k} \right)^2 = \left( \sum_{i=1}^{3N} \frac{P_{ki}}{\sqrt{m_i}} \frac{d\mu_z}{d\Delta r_i} \right)^2 \tag{2.29}$$

where $\mu_z$ is the z-component of the dipole moment, $\Delta r_i$ are the Cartesian displacements and ${P_{ki}}/{\sqrt{m_i}}$ is the mass weighted coordinate matrix of the normal mode.

To simulate the dipole HREELS spectra, we computed the absolute intensities $I_{loss}^k$ of the energy losses normalised to the elastic peak intensity $I_{elastic}$ as

$$\frac{I_{loss}^k}{I_{elastic}} = \left( \sum_{i=1}^{3N} \frac{P_{ki}}{\sqrt{m_i}} \frac{d\mu_z}{d\Delta r_i} \right)^2 \frac{F(\omega_k)}{\omega_k} n_s \tag{2.30}$$

where $n_s$ [45] is the surface coverage, $\omega_k$ is the calculated frequency associated with a given normal mode and $F(\omega_k)$ is a function of some fixed experimental parameters (energy of the electron beam and working angles; see **equations 2.26** to **2.28**).

$$F(\omega_k) = F(\hat{\theta}_C)(1-\theta_E)^{1/2} \tag{2.31}$$

## 2.7 Transition state search

Precise knowledge of the reaction energetics is essential for determining the minimum energy pathway leading from reactants to the desired products. Also, the possible intermediates and transition states need to be identified. At minima (reactants, products and intermediates) and transition states, the first derivatives of the energy (forces) must be zero.

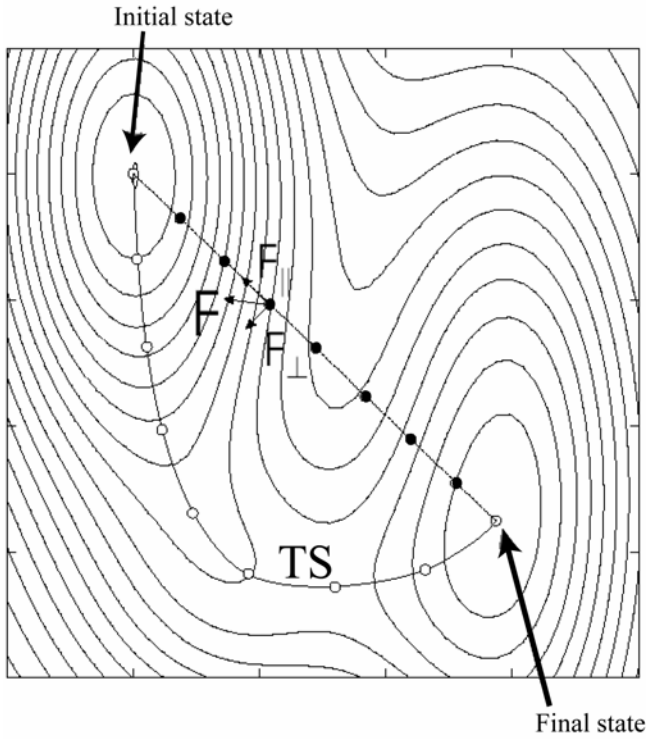


**Figure 2.5.** Schematic representation of the Nudged Elastic Band method. Starting from an initially guessed reaction path (black dot) the chain settles to the minimum energy path (white dot).

However, unlike minima, transition states (i.e. first order saddle points) must be a maximum along one direction (the one which connects the reactant and the product minima) and minimum in all the other (perpendicular) directions i.e. the second derivative of the energy with respect to the reaction coordinate is negative but in all the other directions it is positive [46].

Transition state localisation is vital for understanding the energetics of a chemical reaction. A reliable method is therefore needed to obtain them. Jónsson and co-workers developed the two transition state search algorithms implemented in VASP and used during this thesis: the *Nudged Elastic Band (NEB) Method* and the *Dimer method.* These methods are summarised in the next sections.

### 2.7.1 Nudged elastic band method

The *Nudged Elastic Band (NEB) Method* [47] is an example of what is called a 'chain-of states' method. With these methods, several images or states of the system are connected

to trace out a path of some sort. Two points in the configuration space are needed (initial and final states). First, a set of images ([$R_0$, $R_1$, $R_2$ ... $R_N$], N-1 replicas) between the initial and final states, typically in the order of 4–20, is obtained by linear interpolation (**Figure 2.5**). This is the most important step in the method: the initial guess has to be good enough to converge to a realistic Minimum Energy Path (MEP).

With the NEB method, the N-1 images are optimised with respect to all degrees of freedom except that of the reaction pathway. A spring constant is added to ensure the continuity of the path. The total force on an atom is the sum of the true force perpendicular to the local tangent and the spring force along the local tangent. The projection of the parallel component of the true force acting on the images and the perpendicular component of the spring force are cancelled.

$$F_i = F_i^s|_{\parallel} - \nabla E(R_i)|_{\perp} \tag{2.32}$$

The two projections are

$$\nabla E(R_i)|_{\perp} = \nabla E(R_i) - \nabla E(R_i)\hat{\tau}_i \tag{2.33}$$

and

$$F_i^s = k\left(|R_{i+1} - R_i| - |R_i - R_{i-1}|\right)\hat{\tau}_i \tag{2.34}$$

Here, E is the energy of the system, k is the spring constant and $\tau_i$ the normalised local tangent at the image i. The above definition of the spring force ensures the constant spacing of the images. The program will run each image simultaneously and communicate the forces at the end of each ionic cycle to compute the force acting on each replica. The minimisation of the forces acting on the images would bring the NEB to MEP.

Usually the number of images in NEB is too small for the length of the path and none of the images lies near to the transition state at the end of the minimisation process. Saddle point energy needs to be estimated by interpolation. The CI-NEB [48] was developed to cope with this problem. After several runs with the 'regular' NEB, the highest energy image is identified (*imax*). This image is treated particularly and the force acting on it is now calculated as

$$F_{i\max} = -\nabla E(R_{i\max})| + 2\nabla E(R_{i\max})|_{\parallel} \tag{2.35}$$

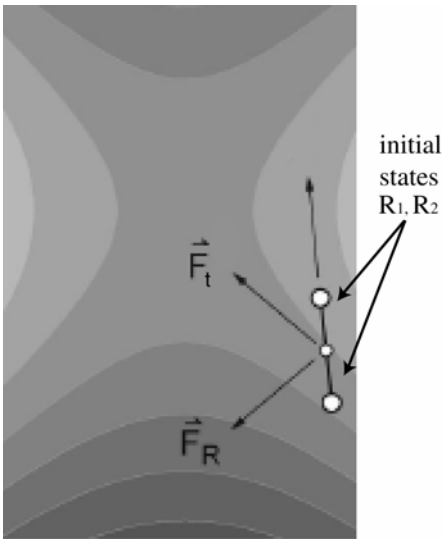


**Figure 2.6.** Schematic representation of the Dimer method.

where $2\nabla E(R_{i\max})|_{\|}$ is twice the opposite of the true force parallel to the local tangent. The highest energy image is no longer affected by the spring forces. The minimisation of this force leads to a rigorous convergence to the saddle point.

### 2.7.2 The Dimer method

The *Dimer method* [49] involves working with two images (replicas, $R_1$ and $R_2$) of the target system (n atoms). This pair of images is called 'dimer'. These two replicas have almost the same 3n coordinates, but are displaced a small distance from a common midpoint (centre of the dimer). The saddle point search algorithm involves moving the dimer uphill on the potential energy surface. There are two parts to each move: rotating and translating the dimer. Each time the dimer is translated, it has to be rotated in order to find the lowest curvature mode (lowest energy orientation). A rotational force $\vec{F}_R$ is defined which is the difference in the force on the two replicas. Minimising the energy with respect to this rotational force aligns the dimer with the lowest curvature mode (see **Figure 2.6**).

The saddle point is at a maximum along the lowest curvature direction. As well as being rotated, the dimer has to be translated and moved up the potential energy surface. The net force acting on the centre of the dimer tends to pull it towards a minimum.

To avoid this, an effective force $\vec{F}_t$ on the dimer is defined. In this modified force, the true force due to the potential acting in the midpoint of the dimer is defined as the opposite of the component along the dimer. Minimising with respect to this force brings the dimer to the saddle point.

In this thesis the *Nudged Elastic Band* method was used in combination with the *Dimer* method to determine the transition states. After a few iterations with the NEB, we obtained a rough estimate of the shape of the MEP. We then chose the two images with the highest energy to be the starting point for the Dimer method. Our results were refined until the value of the forces with the *quasi*-Newton algorithm implemented in VASP was negligible. We found that this sequence of algorithms (NEB, *Dimer*, *quasi*-Newton) was the most efficient for the transition state search.

We verified the transition states identified with the NEB and Dimer methods by vibrational frequency analysis (see **section 2.6.2**), yielding a single negative/imaginary frequency. This imaginary frequency has to be consistent with the reaction path under study.

## 2.8 Density of states

One of the main objectives of computational surface science is to establish a detailed understanding of the adsorption process. *Density of States* (DOS) is an important tool for studying electronic interactions in periodic systems. For each energy E, DOS gives the number of states in the interval [E, E+δE]

$$DOS(E) = \frac{number\ of\ \ states\ between\ E\ and\ E + \partial E}{\partial E} \tag{2.36}$$

Moreover, we can split the 'total' DOS into the different contributions of the atomic orbitals. In VASP the local orbitals are the spherical harmonics. We define the 'projected' Density of States (PDOS) as the projection of the 'total' DOS onto the spherical harmonics (of fixed radius) of each atom. With this approach, it is easier to analyse the character of the bond.

## 2.9 Temperature and pressure phase diagrams

DFT is often described as a zero-temperature, zero-pressure technique. To determine the stable phase at a given temperature and pressure, we must compute the Gibbs free energy for all the competing phases. In this thesis, we calculated the temperature pressure diagrams using a simple thermodynamical model [50] in which the gas phase plays the role of a reservoir in equilibrium with the surface and the substrate phase. Thus, it imposes its pressure and temperature on the adsorbed phase. The free Gibbs energy is expressed as:

$$\Delta G(T,P) = \theta\left( E_{ads} + \Delta ZPE - RT\ln\left(\frac{q_{ads}}{q_{gas}}\right) - RT\log\left(\frac{P}{P_0}\right)\right) \tag{2.37}$$

where $\theta$ is the surface coverage, $E_{ads}$ is the adsorption energy (calculated with VASP), $\Delta$ZPE is the variation of the zero-point energy between the adsorbed phase and the gas-phase plus the clean slab, $q_{ads}$ and $q_{gas}$ are the partition functions of the adsorbed and gas phase, respectively, and the last term comes from the temperature pressure dependence of the gas phase chemical potential.

$\Delta$ZPE is small since the hardest molecular frequencies are not significantly affected by the surface process and therefore do not contribute to the free Gibbs energy. Additional approximations were made to evaluate the partition functions. The partition function of the gas phase molecule is expressed as

$$q_{gas} = q_{gas}(rot)q_{gas}(trans)q_{gas}(vib) \tag{2.38}$$

For the adsorbed case the rotational and translational contributions are transformed into additional vibrational contributions

$$q_{ads} = q_{ads}(vib) \tag{2.39}$$

Finally, we assumed that the vibrational partition functions of the gas-phase, the adsorbed system and the clean surface are rather similar so they can be cancelled out; then:

$$\frac{q_{ads}}{q_{gas}} \approx \frac{1}{q_{gas}(rot)q_{gas}(trans)} \tag{2.40}$$

For a given value of temperature and pressure, the favoured coverage is the one that leads to minimum $\Delta$G. However, we should bear in mind that all our approximations were rather crude and the values obtained only provided general trends in adsorption.

## 2.10 Computational Details

In the previous sections we established the method and model we used to perform all the calculations in this thesis.

To obtain generally uniform results, certain parameters have to be controlled: the DFT lattice constant of the metal (i.e. metal-metal distance), the ideal cut-off of the plane wave expansion, and the number of k-points needed to converge the energy. Also, the vacuum width between adjacent slabs and the thickness (number of layers) of the slabs have to be determined.

First of all, we determined the DFT lattice constant that minimises the energy of the elementary mesh. In this thesis we studied four different metal surfaces: Cu, Pt, Pd and Rh. We optimised the metal-metal interatomic distance for the bulk and obtained the following values: 2.57 Å (Cu–Cu), 2.82 Å (Pt–Pt), 2.80 Å (Pd–Pd) and 2.72 Å (Rh–Rh). All these values are very close to the experimental ones. In fact, the differences are less than 2% [51].

We obtained a tight convergence of the plane-wave expansion with a cut-off of 400 eV. This is the value we used to perform all the calculations in **Chapters 4** and **5**. However, we used a larger value (500 eV) to compute the geometry optimisations and frequency calculations in **Chapter 3**.

For our purposes, we considered several unit cells: √3x√3, 2x2, 3x2, 4x2 4x√3 and 3x3. We performed the 2D Brillouin integrations on a 7x7x1 grid for the √3x√3 unit cells, 5x5x1 for the 2x2 structures, on a 3x5x1 grid for the 3x2 and 4x2, 3x7x1 for the 4x√3 and on a 3x3x1 k-mesh for the 3x3 unit cells. We checked that this density of k points provided a correct convergence of the adsorption energy in the case of the 3x3 unit cell with a difference of ~4 $kJmol^{-1}$ between the 3x3x1 and 5x5x1 grids. Moreover, the energy differences among various adsorption modes were not modified at all when the grid was changed. However, we increased the number of k-points to compute the DOS because these calculations require a denser k-mesh (e.g. for a 2x2 unit cell we used a 7x7x1 k-points grid, for a 3x3 a 5x5x1 mesh …).

We also investigated how the slab thickness and vacuum width affected the adsorption energy.

In agreement with a study of Sautet and co-workers [52], comparison of the four-layer and six-layer slabs showed that the results were consistent only when the k-point convergence was reached and that the six-layer model needed a larger grid. In this thesis the surfaces were modelled by slabs containing four atomic metal layers.

To determine the required vacuum size, we studied the convergence of the adsorption energy using a four layer slab and different vacuum widths. We found that adsorption energies converged for a vacuum width of around 12 Å.

We performed all the calculations on one face of the metal slab (i.e. the target molecule or molecules were adsorbed only on one side of the model). We fully optimised the geometries of the adsorbate and the two uppermost metal planes but kept the two lower metal layers fixed at the optimised bulk geometry.

We computed the adsorption energies ($E_{ads}$) with the following formula

$$E_{ads} = (E_{C_xH_y/surface} - E_{surface} - E_{C_xH_y(g)}) \quad (2.41)$$

To calculate the relative stabilities of the possible reaction intermediates, we used **equation 4.1** and **5.1** (see **Chapter 4** and **5**).

## 2.11 References and Notes

[1] M. Born, J.R. Oppenheimer, *Ann. Physik* 84 (1927) 457.

[2] W.J. Here, L. Radom, P.V.R. Schleyer, J. A. Pople, *Ab initio Molecular Orbital Theory*, John Wiley, New York (1986).

[3] J. Almlöf, R. Ahlrichs, *Notes on Hartree-Fock theory and related topics* in *European Summer School in Quantum Chemistry 2003, Book I,* B. O. Roos, P.-O. Widmark Eds., Lund University, Lund (2003) 169.

[4] B.O. Roos, *Multiconfigurational (MC) Self-Consistent (SCF) Theory* in *European Summer School in Quantum Chemistry 2003, Book II*, B. O. Roos, P.-O. Widmark Eds., Lund University, Lund (2003) 285.
[5] P.R. Taylor, *Coupled-Cluster Methods in quantum Chemistry* in *European Summer School in Quantum Chemistry 2003, Book II*, B. O. Roos, P.-O. Widmark Eds., Lund University, Lund (2003) 361.
[6] N.C. Handy, *Density Functional Theory* in *European Summer School in Quantum Chemistry 2003, Book II*, B. O. Roos, P.-O. Widmark, Eds., Lund University, Lund (2003) 503.
[7] J.E. Baerends, O.V. Gritsenko, *J. Phys. Chem. A* 101(1997) 5383.
[8] M. Head-Gordon, *J. Phys. Chem*. 100 (1996) 13213.
[9] L.H. Thomas, *Proc. Camb. Phil. Soc*. 23 (1927) 542; E. Fermi, *Rend. Accad. Lincei*. 6 (1927) 602.
[10] H. Hohenberg, W. Kohn, *Phys. Rev. B* 136 (1964) 864.
[11] W. Kohn, L.J. Sham, *Phys. Rev. A* 140 (1965) 1133.
[12] S. H. Vosko, L. Wilk, M. Nusair, *Can. J. Phys.* 58 (1980) 1200.
[13] A. D. Becke, *J. Chem. Phys.* 84 (1986) 4524; A. D. Becke, *Phys. Rev. A. 38* (1988) 3098; J. P. Perdew, *Phys. Rev. B.* 33 (1986) 8822; J. P. Perdew, *Phys. Rev. B.* 34 (1986) 7406; J. P. Perdew, Y. Wang, *Phys. Rev. B.* 33 (1986) 8800; C. Lee, W. Yang, R. G. Parr, *Phys. Rev. B.* 37 (1988) 785; J.P. Perdew, K. Burke, M. Ernzerhof, *Phys. Rev. Lett*. 77 (1996) 3865.
[14] A. D. Becke, *J. Chem. Phys.* 98 (1993) 5648.
[15] G.Y. Sun, J. Kurti, P. Rajczy, M. Kertesz, J. Hafner, G. Kresse, *J. Molec. Struc. Theochem* 624 (2003) 37.
[16] G. Pacchioni, *Heterogeneous Chemistry Reviews* 2 (1996) 213.
[17] F. Illas, J.M. Ricart, *Química cuántica en materia condensada: aplicación al estudio de superficies, quimisorción, catálisis heterogénea y propiedades de sólidos* in *Química teórica y computacional*, J. Andrés and J. Beltran Eds., Universitat Jaume I, Castelló de la plana (2001) 217.
[18] J. Sauer, *Chem. Rev*. 89 (1989) 199.
[19] G.Pacchioni, P.S. Bagus, F. Parmigiani (Eds.), *Cluster Models for Surface and Bulk Phenomena*, NATO ASI Series B, Volume 283, Plenum Press, New York, 1992.
[20] N.W. Ashcroft, I. Mermin, N. David, *Solid State Physics*, W.B. Saunders Company, New York (1976).
[21] D. Curulla, A. Clotet, J.M. Ricart, F. Illas, *J. Phys. Chem*. 103 (1999) 5246.
[22] D. Curulla, R. Linke, A. Clotet, J.M. Ricart, J.W. Niemantsverdriet, *Phys. Chem. Chem. Phys.* 4 (2002) 5372.
[23] A. Gil, A. Clotet, J.M. Ricart, G. Kresse, M. Garcia-Hernandez, N. Rösch, P. Sautet, *Surf. Sci.* 530 (2003) 71.
[24] The unit cell of a system is not unique. We can choose the unit cell with the smallest volume, the one with the better symmetry properties or the Wigner-seitz unit cell.
[25] C. Cohen-Tannoudji, B. Diu, F. Laloë, *Mechanique quantique*, Hermann, Paris (1994).
[26] Wigner-Seitz unit cell but in the reciprocal lattice.
[27] H.J. Monkhorst, J.D. Pack, *Phys. Rev. B* 13 (1976) 5188.
[28] D.L. Chadi, M.L. Cohen. *Phys. Rev. B* 59 (1999) 1758.
[29] D.R. Hamann, M. Schlüter, C. Chiang, *Phys. Rev. Lett.* 43 (1979) 1494; G.B. Bachelet, M. Schlüter, C. Chiang, *Phys. Rev B* 26 (1982) 4199.
[30] D. Vanderbilt, *Phys. Rev B* 41 (1990) 7892.
[31] P. Blöchl, *Phys. Rev. B* 50 (1994) 17953.

[32] G. Kresse, J. Hafner, *Phys. Rev. B* 47 (1993) 558; G. Kresse, J. Hafner, *Phys. Rev. B* 48 (1993) 13115; G. Kresse, J. Hafner, *Phys. Rev. B* 49 (1994) 14251; G. Kresse, J. Furthmüller, *Comp. Mat. Sci.* 6 (1996) 15; G. Kresse, J. Furthmüller, *Phys. Rev. B* 54 (1996) 11169.
[33] D.D. Johnson, *Phys. Rev.* B 38 (1988) 12087.
[34] P.Pulay, *Chem. Phys. Lett.* 73 (1980) 393.
[35] G. Kresse, J. Furthmüller, *Comput. Mat. Sci.* 6 (1996) 15.
[36] G. Kresse, J. Furthmüller, *Phys. Rev. B* 54 (1996) 11169.
[37] M. Methfessel, A.T. Paxton, *Phys. Rev. B* 40 (1989) 3616.
[38] M.E. Pemble, *Vibrational Spectroscopy from Surfaces* in *Surface analysis- The Principal Techniques*, Edited by J. C. Vickerman, John Wiley and Sons Ltd., New York(1997) 267.
[39] E.M. McCash, *Surface Chemistry*, Oxford University Press, Oxford (2001)
[40] G. Coudurier, F. Lefebvre, *Infrared Spectroscopy* in *Catalyst Characterisation, Physical Techniques for Solid Materials*, Edited by B. Imelik and J.C. Vedrine, Plenum Press, New York(1994) 11.
[41] J.C. Bertolini, *Vibrational Electron Energy Loss Spectroscopy* in *Catalyst Characterisation, Physical Techniques for Solid Materials*, Edited by B. Imelik and J.C. Vedrine, Plenum Press, New York(1994) 271.
[42] K.W. Kolanski, *Surface Science, Foundations of Catalysis and Nanoscience*, John Wiley and Sons Ltd., West Sussex (2002).
[43] R.G. Greenler, *J. Chem. Phys.* 44 (1966) 310.
[44] Y. Morikawa, *Phys. Rev. B* 63 (2001) 033405.
[45] Coverage is usually represented by the symbol $\theta$. Not used here to avoid any misunderstanding.
[46] J.W. McIver, A. Komornicki, *J. Am. Chem.. Soc.* 94 (1972) 2625.
[47] H. Jónsson, G. Mills, K. W. Jacobsen, Nudged elastic band method for finding minimum energy path of transitions, Classical and Quantum Dynamics in condensed Phase Simulations, J. B. Berne, G. Ciccotti, D. F. Coker Eds, World Scientific, Singapore, 1998, 385.
[48] G. Henkelman, B. P. Uberuaga, H. Jónsson, *J. Chem. Phys.* 113 (2000) 9901.
[49] G. Henkelman, H. Jónsson, *J. Chem. Phys.* 111 (1999) 7010.
[50] K. Reuter, M. Scheffler, *Phys. Rev. B* 65 (2001) 035406.
[51] the experimental values are 2.55 Å, 2.77 Å, 2.75 Å and 2.69 Å for Cu, Pt, Pd and Rh, respectively. R.W.G. Wyckoff, in: *Crystal Structures*, 2nd ed., vol. 1, Interscience, New York (1965).
[52] C. Morin, D. Simon, P. Sautet, *J. Phys. Chem. B* 107 (2003) 2995.

# 6

# Summary and concluding remarks

## 6.1 Summary

In this thesis we performed a systematic study of the adsorption of unsaturated hydrocarbons on metal surfaces. We used DFT-based methods and periodic models. The characterisation of the surface structures, adsorption modes and nature of the adsorbate-surface interaction along with the calculation of the relative stabilities, reaction energies and reaction barriers are key steps to understand surface phenomena. We want also to emphasize that the simulation of vibrational spectra can also play a decisive role in heterogeneous catalysis. Our work was aimed at complementing experimental observations and providing additional data, so that complex surface processes could be unravelled.

We focused our attention on three systems: propyne adsorbed on copper, platinum, palladium and rhodium (**Chapter 3**); the dehydrogenation reaction of propylene to propylidyne on platinum (**Chapter 4**) and the selective hydrogenation of 1,3-butadiene to butane on platinum and palladium (**Chapter 5**).

The objectives and the main conclusions of this work are:

In **Chapter 3**, we present a systematic study of the adsorption of propyne on several metal surfaces: Cu(111), Pt(111), Pd(111) and Rh(111). First of all, we determined the most favourable adsorption sites and their relative stabilities. The agreement between our results and the experimental data available is fairly good. We found that propyne adsorbs on Cu(111) with its molecular plane perpendicular to the metal surface and bisecting a Cu–Cu bond (di-σ/di-π adsorption mode). On the other hand, on Pt(111), Pd(111) and Rh(111), it prefers to sit on a 3-fold hollow site, with the molecular plane tilted away from the surface normal and the C≡C axis parallel to a metal-metal bond (di-σ/π). The decomposition of the adsorption energy in its main contributions helped us to rationalise the variation in adsorption energy observed for Cu (–98 $kJmol^{-1}$), Pd (–161 $kJmol^{-1}$), Pt (–197 $kJmol^{-1}$) and Rh (–226 $kJmol^{-1}$). On the Pt and Rh surfaces, the strong activation of the molecule and the high surface-adsorbate interaction cause propyne to be susceptible of decomposition. These results are well in line with the experimental evidence.

The analysis of the projected density of states (PDOS) enabled us to understand the unique adsorption behaviour of propyne on Cu(111). We found that the differences arise from the unique adsorbate-surface interaction. On this surface, the interaction takes place mainly through the sp-metal band whereas on Pt, Pd and Rh the interaction takes place via the d-band.

Besides, our calculations allowed us to corroborate and complete the experimental band assignment and confirm the adsorption site preference for propyne on Cu(111) and Rh(111). E.M. McCash and co-workers have assigned the band at 1361 $cm^{-1}$ in the spectrum of propyne on Cu(111) to the C≡C stretching mode. This assignment has given rise to a controversy because it violates the metal surface selection rules (MSSR). Our calculations support and complete this assignment. We proposed that this mode strongly mixes with the $CH_3$ symmetric deformation. This coupling enhances the dynamic dipole moment perpendicular to the surface (in the z direction) and makes this mode active. However, on methyl deuteration this coupling disappears but the C≡C stretch is still intense. Our calculations demonstrated that this is due to the special nature of the propyne-Cu interaction.

For the system propyne/Rh(111), we concluded that the Rh surface is mainly covered with species adsorbed in a di-σ/π fashion. The simulated HREELS spectrum matches very well with the experimental one performed by G. A. Somorjai and co-workers. Frequencies and band intensities are well reproduced except for the feature at ~1100 $cm^{-1}$. This feature is clearly weaker in the simulated spectrum than on the experimental one. The presence on the surface of a small fraction of di-σ/di-π adsorbed species explains this difference.

The good agreement between the theoretical and experimental frequencies and intensities enabled us to predict the RAIRS spectrum of propyne on Pt(111) and Pd(111). To our knowledge, these spectra are not available in the literature.

In **Chapter 4**, we investigated the intermediates of the dehydrogenation of propylene to propylidyne on Pt(111). First of all, we studied the adsorption of propylene on Pt(111). For this molecule, we found two stable adsorption structures: bridge (di-σ) and top (π). The adsorption on bridge (–87 $kJmol^{-1}$) is more stable than the adsorption on top (–51 $kJmol^{-1}$). After determining and characterising the adsorption structure of this molecule, we investigated the possible reaction intermediates. Our study allowed us to obtain the adsorption site, geometry and relative stabilities of propylidyne and several $C_3H_x$ (x=3–7) intermediates that may potentially be involved in the propylene-to-propylidyne transformation (1-propyl, 2-propyl, propylidene, 1-propenyl, 2-propenyl, propyne, propenylidene and propynyl). Our calculations showed that the Pt(111) surface tends to stabilise $sp^3$ bound intermediates. They also indicate that the dehydrogenation of propylene to propylidyne is favoured because the propylidyne moiety is the most stable surface species. Moreover, we computed the reaction energy for the possible elementary steps involved in the dehydrogenation reaction. Our calculations indicate that the propynyl intermediate formation is not energetically favoured and, therefore, this species may not be involved in the direct transformation of propylene to propylidyne.

Besides, we simulated the vibrational spectra for propylene, propylidyne and all the $C_3H_x$ (x=3–7) intermediates. The results for propylene and propylidyne are in reasonable

agreement with the experimental data. Unfortunately, the information available for the possible reaction intermediates is scarce. F. Zaera and co-workers have studied the changes in the IR spectrum of propylene on Pt(111) between ~230–300 K. They observed that the spectrum at ~260 K presents a signal at 2890 $cm^{-1}$ that cannot be assigned to propylene either to propylidyne and, therefore, it belongs to a new species. Moreover, in the 1100–1500 $cm^{-1}$ region all the features correspond to propylene or to propylidyne. Our best guesses are propylidene and 1-propenyl.

We also studied the surface structure and stability of a propylene-sulphate complex on Pt(111). We showed that the formation of this intermediate is energetically favoured and provided a theoretical support to the experimental observations. We proposed the surface structure for this alkyl-sulphate complex and demonstrated that the interaction of propylene with sulphate species activates the hydrocarbon molecule up to a large extent. Moreover, we showed that the simulated IR spectrum of the adsorbed alkyl-sulphate can be very useful to the identification of this surface species. The peaks at 1078 and 1047 $cm^{-1}$ and the splitting of the $SO_4$ group frequencies of the sulphate unit are the fingerprint of this intermediate.

We studied the selective hydrogenation of 1,3-butadiene to butenes on Pt(111) and Pd(111) in **Chapter 5**. First of all, we studied the adsorption of 1,3-butadiene and butenes on Pt(111) and Pd(111). Despite the different electronic behaviour of Pt and Pd surfaces, the same adsorption modes with close adsorption energies have been found for 1,3-butadiene and butenes on both metal surfaces. For the 1,3-butadiene molecule the preferred adsorption structure has been characterised as a tetra-σ mode with the four C atoms bounded to four neighbour Pt atoms. In this surface structure the carbon chain remains almost parallel to the surface. The most stable adsorption mode for the butenes is the di-σ-mode. In the optimised geometry the C=C bond lies parallel to the metal surface and the alkyl groups point outwards the surface. Nevertheless on Pd(111) the molecules are less distorted than on the Pt surface. Moreover, the π adsorption modes are less destabilised with respect to the σ ones on Pd(111). In consequence, the energy difference between the di-σ and π modes is clearly smaller on palladium. We showed that the different selectivity observed on Pt(111) and Pd(111) for this reaction cannot be satisfactory explained by the single comparison of the relative stabilities of 1,3-butadiene and 1-butene on these metals. Our calculations suggested that the different selectivity observed arises from the reaction intermediates. We analysed the possible reaction pathways and computed the activation barriers. The pathway leading to the butan-1,3-diyl radical is competitive with those leading to butene on Pt(111). Indeed, the difference in energy activation is only 5 $kJmol^{-1}$. The formed butene desorbs as long as butadiene is present on the surface. The di-radical intermediate can be further hydrogenated, leading to the formation of butane as a primary product. This is in good agreement with the partial selectivity (60 %) to butene observed in experiments. On Pd(111), the butan-1,3-dyil radical is also stabilised but this effect is clearly smaller than on Pt. The difference in activation energy leading to 1-butene and butan-1,3-dyil is large enough (~30 $kJmol^{-1}$) to exclude the formation of this intermediate. Hence, our calculations predict a full selectivity to butene on Pd(111) in agreement with experiments.

## 6.2 General conclusions

The chemistry of unsaturated hydrocarbons at metal surfaces assumes a daunting complexity because of the huge number of possible surface structures. The great variety of species arises from the availability of large ensembles of atoms. Periodic DFT calculations proved once more to be an excellent partner of experiment. These methods permitted us to calculate adsorbate energetics, structure and spectra. Moreover, they provided detailed information on the elementary reaction steps, in terms of thermochemistry, reaction pathways and activation barriers.

The main conclusions about the studied systems can be divided in five groups:

- Chemisorption energy of molecules and molecular fragments

Calculations permitted us to obtain the adsorption energies on different adsorption sites for different unsaturated hydrocarbons adsorbed on metals. The decomposition of the adsorption energy in its main contributions (the distortion energy of the surface, the distortion energy of the molecule and the interaction energy) enabled us to rationalise the results obtained.

We also computed the relative stabilities for possible reaction intermediates. To obtain the adsorption energies for reaction intermediates is a key step in the study of the possible reaction pathways.

- Structure of adsorbates

We obtained the geometries and preferred adsorption site for propyne, propylene, 1,3-butadiene and butanes on several metal surfaces. Our results are in good agreement with the experimental data available. Therefore, we conclude that we can use calculations to predict the unknown structures.

Moreover, calculations demonstrated once again to be very useful to characterise weakly adsorbed structures and short-lived reaction intermediates. These species are extremely difficult to isolate and characterise by experiments because it is necessary to work in very restrictive conditions (usually UHV and very low temperatures).

- Nature of the adsorbate-surface interaction

Calculation of the projected density of states (PDOS) allowed us to rationalise the chemisorption energies and corroborate the conclusions obtained from the decomposition of the adsorption energy.

- Computed spectra and assignment of vibrational bands

The simulation of vibrational spectra of adsorbed molecules enabled us to corroborate and complete dubious band assignment and study the effects of the coupling between modes in the spectrum.

Moreover, simulation of vibrational spectra also demonstrated to be useful to determine the adsorption site preference.

The good agreement between the theoretical frequencies and intensities and experimental data available enabled us to predict the vibrational spectra for some molecules.

Frequency calculations also demonstrated to be useful to facilitate the identification of reaction intermediates. The computed values can be used as fingerprint of these short-lived molecules.

- Selectivity control

We confirmed that DFT calculations are a powerful tool to give some insights in the factors that control selectivity. The detailed investigation of all the possible reaction pathways and the calculation of the reaction barriers can play a crucial role in understanding the surface processes.

UNIVERSITAT ROVIRA I VIRGILI

# Modelling unsaturated hydrocarbons on metals: towards understanding catalytic processes

**Ana Valcárcel Ortí**
Departament de Química Física i Inorgànica

Memòria presentada per optar al
grau de Doctor en Química

UNIVERSITAT ROVIRA I VIRGILI

Departament de Química Física i Inorgànica
c/ Marcel·lí Domingo, s/n
43007 Tarragona

**Josep Manel Ricart Pla**, Catedràtic de Química Física, i **Anna Maria Clotet Romeu**, Professora titular de Química Física, del Departament de Química Física i Inorgànica de la Universitat Rovira i Virgili

Fem constar que la present memòria, que porta per títol:

"**Modelling unsaturated hydrocarbons on metals: towards understanding catalytic processes**"

ha estat realitzada sota la nostra direcció al Departament de Química Física i Inorgànica de la Universitat Rovira i Virgili per la llicenciada en Química Ana Valcárcel Ortí per obtenir el grau de Doctor en Química.

Tarragona, Maig de 2005.

Dr. Josep Manel Ricart Pla

Dra. Anna Maria Clotet Romeu

A la meva família

Quando il gioco e’finito,
il Re e la pedina ritornano nella stessa scatola
(Proverbio italiano)

Un vegada s’ha acabat el joc,
el rei i el peó tornen a la mateixa caixa.
(Proverbi italià)

# 5

# Selectivity control over the catalytic hydrogenation of 1,3-butadiene on Pt(111) and Pd(111) surfaces

*We have studied the hydrogenation reaction of 1,3-butadiene on both Pt(111) and Pd(111) to determine why the selectivities to butenes observed experimentally are different. We propose that the distribution of products (60% selectivity on Pt vs. 100% selectivity on Pd) depends on the adsorption strength and the adsorption mode of 1,3-butadiene relative to butenes. In this chapter we show that the different selectivities on Pt and Pd surfaces cannot be satisfactorily explained by simply comparing the relative stabilities of the diene molecule and the monoalkene. Indeed, the same adsorption modes with close adsorption energies have been found for 1,3-butadiene and butene molecules on both metal surfaces. A possible explanation is found by investigating the hydrogenation reaction itself. It seems clear that the key to the selectivity to butene lies in the relative stabilities of radical intermediates on Pt(111) and Pd(111). On the platinum surface, the formation of radical species seems to compete with that of butenes. This could explain its poor selectivity to butenes and the formation of butane as a primary product.*

*This chapter is organised as follows: section 5.1 is a summary of the already published experimental and theoretical results for the selective hydrogenation of 1,3-butadiene to butene on transition metal surfaces; section 5.2 discusses the adsorption energies, adsorption modes and geometries of 1,3-butadiene and the three butene isomers; section 5.3 discusses the relative stabilities and surface structures of different intermediate species; section 5.4 briefly discusses coadsorption with hydrogen; section 5.5 develops the systematic study of the possible reaction pathways and analyses the results, and section 5.6 summarises the main conclusions.*

## 5.1 Introduction

A good catalyst must have both high stability and high activity but its single most important attribute is selectivity. The selective hydrogenation of alkynes and dienes from streams containing chiefly alkenes, $C_2$, $C_3$ or $C_4$, is an important problem in the petrochemical industry. Steam cracking, catalytic cracking and coking lead to traces of alkynes and/or dienes, which have to be selectively hydrogenated into olefinic compounds before alkenes can be further processed by polymerisation or selective oxidation, etc. (see **Scheme 5.1**). In this context, the production of high purity butene ($C_4H_8$) streams for

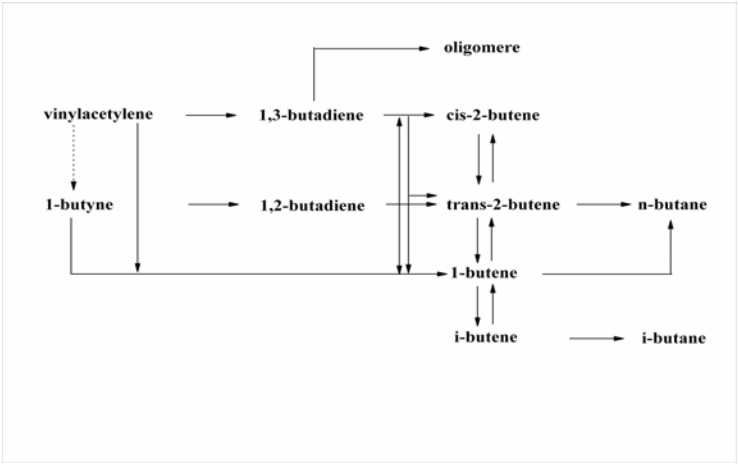


**Scheme 5.1**. Summary of the reactions taking place in the $C_4$ fraction.

polymerisation or copolymerisation processes requires the hydrogenation of the butadiene ($C_4H_6$) impurities contained in the butene cuts. The hydrogenation of 1,3-butadiene can lead to different products: partial hydrogenation yields to butene, while total hydrogenation leads to butane. As the target product is the alkene, the catalyst must not hydrogenate any of the butene moieties and reduce the diolefine to butene rather than butane. One should bear in mind that the traces of diene are hydrogenated in the presence of large amounts of butenes, whose conversion into butane must be kept as low as possible even when all the diene is consumed. The crucial step is then to control the selectivity of this catalytic reaction. It is generally accepted that catalytic hydrogenation processes occur by the generally accepted Horiuti-Polanyi mechanism [1,2]. Indeed, much of the research that has been devoted to acetylene and ethylene hydrogenation strongly supports this mechanism [3,4]. For the 1,3-butadiene hydrogenation, the Horuiti-Polanyi mechanism implies the initial formation of a $C_4H_7$ moiety and subsequent hydrogenation to a $C_4H_8$ species.

$$C_4H_6 \overset{+H}{\longleftrightarrow} C_4H_7 \overset{+H}{\longleftrightarrow} C_4H_8$$

**Scheme 5.2**

The active components of the catalysts for this reaction are usually noble metals, such as palladium or platinum. Palladium is still considered the best catalyst for the partial hydrogenation of alkadienes [5]. Exhaustive experimental studies on single crystal catalytic surfaces have shown that selectivities for the partially hydrogenated product (mainly 1-butene) approach 100% with Pd(111) while Pt(111) is much less selective (up to 60%) [6-11]. The difference between the reaction on the palladium surface and the reaction on the platinum surface was attributed to the different adsorption strengths and adsorption modes of 1,3-butadiene and butenes. It was thought that the strongly adsorbed 1,3-butadiene displaced the more weakly adsorbed butenes from the Pd(111) surface so no further hydrogenation could occur. On the other hand, the adsorption strength of 1,3-butadiene was equivalent to that of butene on the Pt(111) face. A lower selectivity was therefore expected. This hypothesis was supported by EHT calculations [12,13] and experimental studies [14,15]. However, Mittendorfer *et al.* [16] found that the adsorption energy of butadiene was stronger than 1-butene on both Pd and Pt surfaces. These authors suggested that the lower stability of 1-butene on Pd *versus* Pt could explain the higher hydrogenation selectivity observed for Pd. Unfortunately, no detailed results for the reaction mechanism are provided. Note that although much research has dealt with the adsorption of 1,3-butadiene and butene isomers on both Pt and Pd (111) surfaces, a consensus has not been reached. **Scheme 5.3** shows the different adsorption modes proposed in the scientific literature for 1,3-butadiene ($CH_2$=CHCH=$CH_2$). At low temperatures (< 95 K), 1,3-butadiene was found to be loosely bonded to both Pt and Pd surfaces [6,15]. At higher temperatures, Avery and Sheppard [17] suggested by means of EELS the presence of two adsorption modes (1,2-di-σ-adsorption and 1,2,3,4-tetra-σ-adsorption) for this molecule on Pt(111). The di-σ picture of the interaction was supported by some experimental [6,14] and theoretical [12,13] works. Bertolini *et al.* [15] reported a 1,4-di-σ-adsorbed molecule

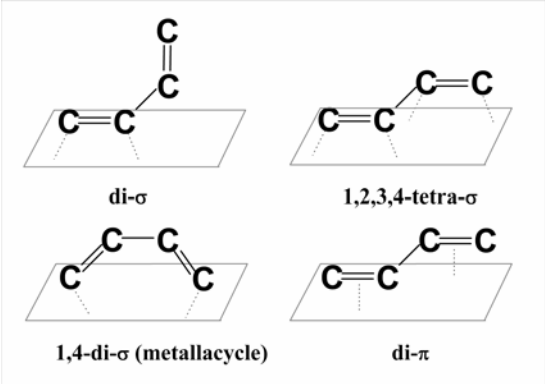


**Scheme 5.3.** Adsorption structures proposed for 1,3-butadiene. For sake of clarity, only C skeleton is shown.

(metallacycle). This structure was in agreement with theoretical considerations provided by qualitative molecular orbital calculations [18]. On the Pd(111) surface, UPS and NEXAFS experiments [6,15] have proposed a di-π-adsorption mode near room temperature. The picture for the various butene isomers is less ambiguous. At low temperatures, 1-butene ($CH_3CH_2CH=CH_2$) and 2-cis/trans-butenes ($CH_3CH=CHCH_3$) are di-σ-bonded to the clean Pt(111) surface, as is suggested by EELS, TDS, UPS and NEXAFS experiments [6,14,15,17,19-21]. Around room temperature, all these species desorb or transform into a more dehydrogenated molecule. On palladium, 1-butene is reported to be π-bonded at temperatures under 200 K. As on Pt(111), at higher temperatures, this molecule desorbs [6,15]. Unfortunately, to our knowledge no data are available for the 2-butene isomers adsorbed onto the Pd(111) surface. Very recent Density Functional (DF) calculations suggested that 1,2,3,4-tetra-σ for the 1,3-butadiene molecule and a di-σ adsorption mode for 1-butene are the most favoured configurations on both metal surfaces [16].

Similar thermodynamic arguments had been used to explain the high selectivity of the Pd catalyst on the hydrogenation of acetylene [2]. It was thought that the strongly adsorbed acetylene ($C_2H_2$) molecule displaced the more weakly bound ethylene ($C_2H_4$) from the Pd surface. Consequently, the surface would be predominantly covered with acetylene. The rate of acetylene hydrogenation is therefore supposed to be faster than for ethylene. However, a later study [22] indicated that these arguments are not complete because they could not explain the noticeable ethylene hydrogenation observed under high pressures of acetylene. Moreover, these classical thermodynamic arguments do not take into account the presence of other intermediate species on the surface. Vinylidene ($CH_2C$), vinyl ($CH_2CH$) and ethylidene ($CH_3CH$) moieties have been found to play a crucial role in ethylene formation [23].

Another interesting point in 1,3-butadiene hydrogenation is the formation of butane observed on platinum surfaces from the beginning of the reaction [24]. Butane is a primary

product of the reaction and is formed in a significant amount relative to butenes. This different behaviour was not ascribed to a very low desorption rate of the intermediate olefin but to the nature of the half hydrogenated species. Additionally, several papers dealt with the reactivity of metallacyclic intermediates that could play an important role in hydrogenation-dehydrogenation reactions [25,26,27].

In this chapter, we investigated the hydrogenation of 1,3-butadiene to several $C_4H_8$ species on both the Pt(111) and the Pd(111) surfaces using DFT methods. First we aimed to determine and compare the geometry, binding site preference and adsorption energies of 1,3-butadiene ($C_4H_6$), 1-butene and 2-*cis/trans*-butenes ($C_4H_8$) on both metal surfaces and discuss any general trends. Our objective was to check if simply thermodynamical arguments are enough to explain the experimental findings and evaluate the necessity of the study of the possible reaction pathways. We then further studied the hydrogenation reaction itself in order to determine the adsorption structures and relative stabilities of the various reaction intermediates ($C_4H_7$ and $C_4H_8$ radical species) and investigate the possible reaction pathways. Our results are analysed and discussed in detail.

## 5.2 Adsorption of 1,3-butadiene ($C_4H_6$) and butenes ($C_4H_8$) on Pt(111) and Pd(111)

### 5.2.1 Gas phase species

First, for the sake of comparison, we optimised the geometry of the gas phase molecules. To avoid lateral interactions between periodic images, a large box (15x15x20 $Å^3$) was taken as unit cell. The results for the 1,3-butadiene ($CH_2$=CHCH=$CH_2$, 13BD) molecule are close to those of previous experimental [28] and theoretical [29] studies. Our calculations predicted a C–C distance of 1.45 Å, a C=C of 1.34 Å and a CCC angle of ~124º for the *trans*-1,3-butadiene molecule. The values for the *cis* isomer are 1.46 Å, 1.34 Å and ~125º, respectively. For the 1-butene ($CH_3CH_2CH$=$CH_2$, 1B) and 2-*cis/trans*-butenes ($CH_3CH$=$CHCH_3$, 2B) the C–C distances are within 1.50-1.52 Å and the double bonds are in the interval 1.33-1.34 Å. Among the butane isomers, our calculation predicted that 2-butenes are thermodynamically more stable than 1-butene by 15 $kJmol^{-1}$.

### 5.2.2 Pt(111) surface

The adsorption energies of 1,3-butadiene and butanes at four different coverages are shown in **Table 5.1** for the species studied. The characteristic bond lengths for the adsorbed structures are given in **Table 5.2**. Only the 3x3 unit cell ($\theta = 1/9$) was used for all the molecules and structures. We studied the influence of the adsorbate coverage for the most stable structures and for the adsorption modes proposed in previous studies. For our purposes, we considered different unit cells: $\sqrt{3}$x$\sqrt{3}$, 2x2 and 3x2 associated with molecular coverages of 1/3, 1/4 and 1/6 ML [30]. We considered and optimised various adsorption structures. We have used the standard notation ($\pi$, di-$\sigma$…) and straightforward extensions. This notation is not directly linked to the hybridisation state of the carbon atoms but

**Table 5.1.** Adsorption energies ($kJmol^{-1}$) for the various chemisorption structures of 1,3-butadiene, 1-butene and 2-cis/trans-butene on Pt(111), as a function of the coverage

| θ | 1/3 | 1/4 | 1/6 | 1/9 |
|---|---|---|---|---|
| **1,3-butadiene** | | | | |
| di-π-cis | | | | −114 (−13) |
| di-π-trans | | | −110(−18) | −122 (−14) |
| di-σ | −45(−15) | −78(−20) | −85(−14) | −89 (−10) |
| 1,2-di-σ-3,4-π | | −75(−19) | −122(−20) | −140 (−16) |
| 1,4-di-σ-2,3-π | | | −137(−23) | −150 (−17) |
| 1,2,3,4-tetra-σ | | | −156(−26) | −163 (−18) |
| **1-butene** | | | | |
| π | | | | −66 (−7) |
| di-σ | −45(−15) | −83(−21) | −91(−15) | −96(−10) |
| **2-cis-butene** | | | | |
| π | | | | −58(−6) |
| di-σ | | | | −80(−9) |
| **2-trans-butene** | | | | |
| π | | | | −48 (−5) |
| di-σ | | | | −81(−10) |

The adsorption modes are those shown in Figures 5.1 and 5.3. The values in parenthesis are the adsorption energies per surface metal atom.

indicates how the double bonds of the molecule are bound to the surface, i.e. Pt-C bonds with the same metal atom for π and with neighbouring ones for di-σ.

We calculated the adsorption energies using the gas phase species $C_4H_x$ (x = 6, 8) as the energy reference using the formula **2.41** (**section 2.10**, **Chapter 2**)

*1,3-butadiene.* The minima obtained for the 1,3-butadiene molecule are shown in **Figure 5.1**. The adsorption structures are named as di-σ (**Figure 5.1a**), di-π-*cis* (**Figure 5.1b**), di-π-*trans* (**Figure 5.1c**), 1,2-di-σ-3,4-π (**Figure 5.1d**), 1,4-di-σ-2,3-π (**Figure 5.1e**) and 1,2,3,4-tetra-σ (**Figure 5.1f**). Only in the di-σ adsorption mode is the carbon chain not parallel to the metal surface. In this mode the molecule interacts with two surface metal atoms through one of its double bonds (parallel to the surface) while the rest of the molecule is tilted away from the metal surface. The two di-π adsorption configurations are bound to the metal surface via their two C=C bonds. The nature of the molecule-surface interaction is the same in both di-π adsorption structures. The difference lies in the conformation of the adsorbed molecule (*cis* vs. *trans*). In the 1,2-di-σ-3,4-π, again the two C=C bonds are involved in the interaction with the metal surface but not in the same way. One of the double bonds interacts with two neighbouring metal atoms while the other is bound to a single surface atom. The nature of the carbon-metal interactions in the 1,4-di-σ-2,3-π is similar to the one described for the 1,2-di-σ-3,4-π adsorption mode but a redistribution of the π electron system takes place during the adsorption process. The

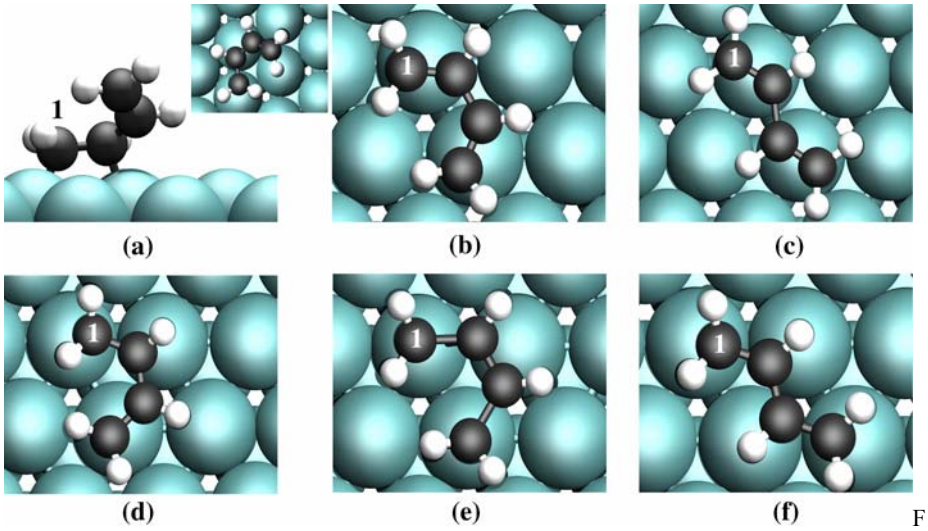


F

**Figure 5.1.** Adsorption modes for 1,3-butadiene on Pd and Pt (111) metal surfaces. di-σ (a), di-π-*cis* (b), di-π-*trans* (c), 1,2-di-σ-3,4-π (d), 1,4-di-σ-2,3-π (e) and 1,2,3,4-tetra-σ (f). Carbon atom number 1 is displayed for sake of clarity.

middle C–C bond gains double bond character at the expense of the terminal ones. The molecule forms two bonds through the terminal C atoms and a π-interaction via its central C–C bond. Finally, in the 1,2,3,4-tetra-σ-adsorption mode, the molecule has a *trans* conformation and interacts with the metal surface via all its C atoms.

Of all the structures tested, the most stable adsorption mode is the 1,2,3,4-tetra-σ one (**Figure 5.1f**). The 1,4-di-σ-2,3-π (**Figure 5.1e**), also called metallacycle [15,18,21], is only 13 kJmol$^{-1}$ less stable, however. So, considering the approximations for evaluating exchange-correlation terms in GGA-DFT, the presence of a metallacycle adsorption mode on the surface cannot be excluded on the basis of total energy. The di-σ-adsorption mode is farther apart (74 kJmol$^{-1}$) from the most stable structure, so it can clearly be rejected. These results contradict EHT calculations made by Minot and co-workers [12] and Sautet *et al.* [13] that indicated that the di-σ adsorption mode was the most stable one on the Pt surface. Three more minima were found for the 1,3-butadiene molecule on the Pt(111) surface: the di-π, *cis* and *trans,* and the 1,2-di-σ-3,4-π adsorption modes (**Figures 5.1b**, **5.1c** and **5.1d**). The two π adsorbed modes (di-π-*cis* and di-π-*trans*) have similar adsorption energies and geometries (see **Tables 5.1** and **5.2**). These surface structures are less stable than the tetra-σ adsorption mode by 49 and 41 kJmol$^{-1}$, respectively. The 1,2-di-σ-3,4-π adsorption mode was only 23 kJmol$^{-1}$ less stable than the 1,2,3,4-tetra-σ mode. Calculation of the adsorption energies per surface atom (**Table 5.1**, numbers in brackets) showed that the most stable adsorbed phase for the 1,3-butadiene at 0 K is the 1,2,3,4-tetra-σ adsorption mode in a 1/6 ML coverage. One should bear in mind that, due to steric effects, flat structures, like 1,2,3,4-tetra-σ or 1,4-di-σ-2,3-π modes, cannot exist at high coverages.

**Table 5.2**. Geometrical parameters for the adsorption structures of 1,3-butadiene, 1-butene and 2-cis/trans-butene on Pt(111) for a coverage of θ = 1/9 ML

| | **Pt–C$^1$** | **Pt–C$^2$** | **Pt–C$^3$** | **Pt–C$^4$** | **C$^1$–C$^2$** | **C$^2$–C$^3$** | **C$^3$–C$^4$** |
|---|---|---|---|---|---|---|---|
| **1,3-butadiene** | | | | | | | |
| di-π-cis | 2.17 | 2.25 | 2.23 | 2.17 | 1.42 | 1.47 | 1.42 |
| di-π-trans | 2.18 | 2.22 | 2.23 | 2.17 | 1.42 | 1.46 | 1.42 |
| di-σ | 2.11 | 2.17 | [2.90] | [3.81] | 1.49 | 1.47 | 1.35 |
| 1,2-di-σ-3,4-π | 2.11 | 2.17 | 2.33 | 2.16 | 1.49 | 1.46 | 1.42 |
| 1,4-di-σ-2,3-π | 2.10 | 2.26 | 2.26 | 2.10 | 1.48 | 1.43 | 1.48 |
| 1,2,3,4-tetra-σ | 2.10 | 2.18 | 2.18 | 2.11 | 1.48 | 1.48 | 1.48 |
| **1-butene** | | | | | | | |
| π | 2.19 | 2.23 | [2.61] | [4.01] | 1.41 | 1.51 | 1.54 |
| di-σ | 2.12 | 2.14 | [3.05] | [4.45] | 1.49 | 1.52 | 1.54 |
| **2-cis-butene** | | | | | | | |
| π | [3.48] | 2.24 | 2.24 | [3.44] | 1.50 | 1.42 | 1.50 |
| di-σ | [3.02] | 2.15 | 2.15 | [3.02] | 1.52 | 1.50 | 1.52 |
| **2-trans-butene** | | | | | | | |
| π | [3.21] | 2.23 | 2.23 | [3.24] | 1.50 | 1.42 | 1.50 |
| di-σ | [3.03] | 2.13 | 2.13 | [3.03] | 1.52 | 1.50 | 1.52 |

Distances are in Å. The numbers in brackets account for the distance between two atoms not directly bound.

For all species studied, the Pt–C bonds are in the range 2.10-2.33 Å, which is the normal range for organometallic complexes [31]. The C–C bonds involved in the adsorption are elongated with respect to the gas phase except for the C–C central bond of the 1,4-di-σ-2,3-π structure, which gains a double bond character and is shortened during the adsorption processes. The C–C bond length is used as a measure of the activation of the adsorbed molecule. We found that the C–C bond is more elongated for the di-σ geometries than for the π ones, in relation to the stronger adsorption. The most stable structure for the 1,3-butadiene on the Pt surface expanded its C–C bonds considerably (1.48 Å). This value is close to the usual distance for a C–C single bond (1.54 Å) and is in good agreement with the C–C distance for the ethene molecule on Pt in previous experimental [32] and theoretical [33,34] studies. This indicates the σ nature of the bonding and an important reduction in the double bond character. The fact that the three C–C bonds are equal indicates that they acquire the same character upon adsorption. The σ interaction is accompanied by a rehybridisation towards $sp^3$ and a C–$CH_2$ angle of ~132º compared to 180º for an alkene, which is close to the characteristic value in alkanes (125º). On the adsorption modes named as di-π, the values of the C-$CH_2$ angles (~157º) are only slightly different from those of the $sp^2$ hybridisation.

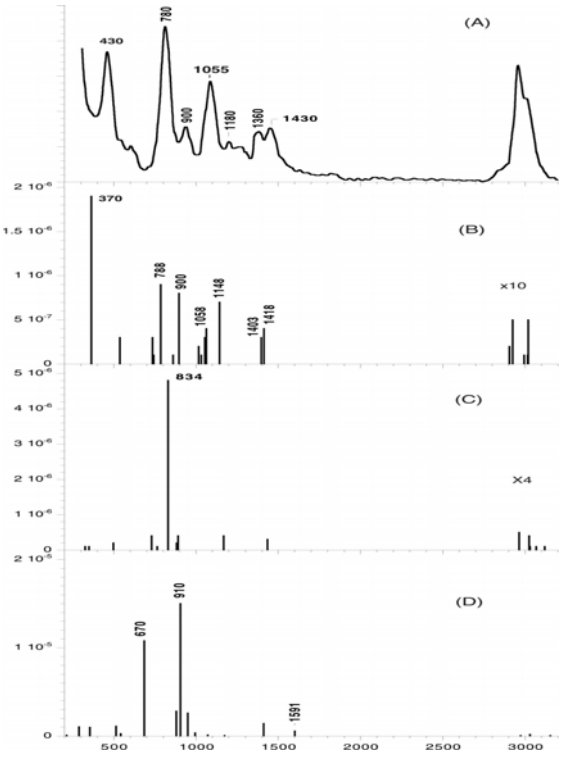


**Figure 5.2.** Vibrational spectra of 1,3-BD on Pt(111). Experimental EELS from ref.17 (a), 1,2,3,4-tetra-σ (b), 1,4-di-σ-2,3-π (c) and di-σ (d). Frequencies in $cm^{-1}$. Intensities in arbitrary units.

Since the total energy calculations did not allow a clear-cut discrimination between the two most stable structures (1,2,3,4-tetra-σ and the metallacycle), the simulation of vibrational spectra from first principles is the key to obtaining further information and direct comparisons between calculated and measured data. There is no information about coverage in the experimental sources [17,19]. We calculated the simulated spectra for the most stable system obtained in our calculations (1/6-ML). As a reference, we also calculated the frequencies of the gas phase 1,3-butadiene (see **Appendix A.4**). The good agreement between the experimental [29,35] and computed values validates the theoretical approach used to calculate the vibrational frequencies (see details of frequency calculations in **section 2.6.2, Chapter 2**). Pure DFT frequencies usually agree very well with experimental frequencies [36] but, due to anharmonic effects, C–H stretching frequencies are slightly overestimated [37,38]. The approximate description of the C–H stretching region is not a hindrance because this part of the spectrum does not hold the subsequent analysis. For our results for free 1,3-butadiene, the errors were below 2% except for the highest $CH_2$ as st and the lowest C=C–C bi and C–C to frequencies.

**Figure 5.2** shows the experimental [17] and calculated vibrational spectra for the adsorbed 1,3-butadiene molecule. **Figures 5.2b, 5.2c** and **5.2d** correspond to 1,2,3,4-tetra-σ, metallacycle and di-σ structures respectively. The experimental EELS spectrum (**Figure 5.2a**) shows a large number of bands with intensities greater than ~1/3 of the most intense one at 780 $cm^{-1}$: the CH stretching bands around 2900–3000 $cm^{-1}$ and several peaks at 1430, 1360, 1180, 1055, 900 and 430 $cm^{-1}$. Later HREELS studies of the same system [6,15] are comparable to this spectrum obtained by Avery and Sheppard [17].

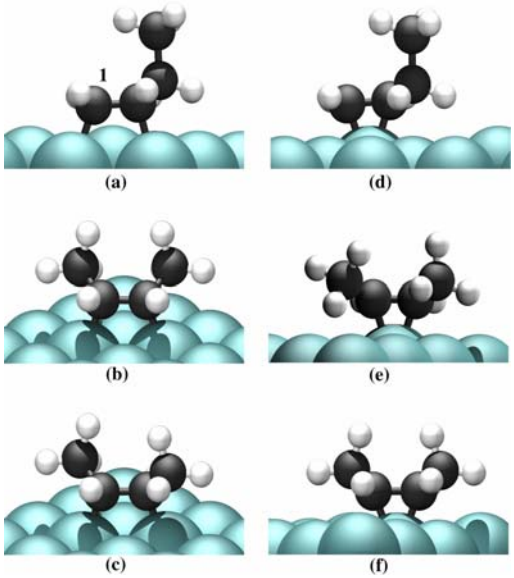


**Figure 5.3.** Adsorption modes for 1-butene and 2-*cis/trans*-butenes on Pd and Pt (111) metal surfaces. (a), (b) and (c) correspond to the di-σ-adsorption mode for 1-butene, 2-*cis*-butene and 2-*trans*-butene, respectively. The π-adsorption mode for the three isomers is depicted in (d), (e) and (f).

The spectrum for the tetra-σ mode (**Figure 5.2b**) matches the experimental data very well, with shifts in the calculated frequencies of 5–30 $cm^{-1}$ and a fair agreement in the intensities. The main peaks present in the experimental spectrum also appear in the theoretical one: 1418, 1403, 1148, 1058, 900, 788 and 370 $cm^{-1}$ assigned to the $CH_2$ sci (scissoring) of $C^1$, $CH_2$ sci of $C^4$, $CH_2$ ro (rocking), C=C st (stretching), CH s bo (deformation out of plane), $CH_2$ as to (torsion) and Pt–C totally symmetric st modes. Only the peak at 370 $cm^{-1}$ is slightly far away from the experimental one, but this could be due to computational limitations for low frequency modes [39]. With regard to intensities, the peak at 1055 $cm^{-1}$ (exp) is formed by the superposition of several calculated bands, and the relative calculated intensity for the main peak at 780 $cm^{-1}$ (exp) appears to be somewhat underestimated.

The spectrum for the metallacycle adsorption mode is much less balanced and shows a dominant peak at 834 $cm^{-1}$ assigned to the CH symmetric bending mode (out-of-plane deformation). Taking into account the finite experimental resolution, this peak may have overlapped with the band at 780 $cm^{-1}$ (exp) and increased its intensity. However, the total absence of intense modes for this metallacycle structure around 1000 $cm^{-1}$ and, more generally, the small relative intensity of all other peaks of the spectrum compared to the dominant one at 834 $cm^{-1}$ indicate that this structure cannot be the majority species on the surface (see **Figure 5.2c**).

The spectrum of the di-σ adsorption mode (**Figure 5.2d**) is clearly dominated by the features at 670 and 910 $cm^{-1}$. Compared to these intense peaks, bands in the regions of 300, 1000 and 3000 $cm^{-1}$ were *quasi*-negligible. For all these reasons, and due to the presence of a peak at 1591 $cm^{-1}$ assigned to the C=C st, the agreement with the experimental spectrum is very poor. Therefore, considering the relative stabilities in the total energy calculations and comparing simulated spectra with experimental ones [6,15,17], we suggest that the 1,2,3,4-tetra-σ mode is the most probable adsorption structure. However, the metallacycle structure could be present on the surface as a minority species. This would explain why the intensity for the peak at 780 $cm^{-1}$ is greater than that simulated for the 1,2,3,4-tetra-σ structure alone.

*Butenes.* For a first insight into the surface processes, we studied the adsorption of 1-butene and 2-cis/trans-butenes on the Pt(111) surface. **Table 5.1** also shows the adsorption energies for the three isomers. The picture is obviously simpler for butenes than for butadiene. Only a π or a di-σ interaction is possible for these molecules (see **Figure 5.3**). For all isomers, the di-σ adsorption mode is unambiguously the preferred one on the Pt(111) surface (the π adsorption mode was 30 $kJmol^{-1}$ less stable than the di-σ mode). We considered various conformations of the 'ethyl group' in the case of the 1-butene. Of all the possibilities we tested, the structure with the 'ethyl group' *quasi* perpendicular to the metal surface was the most stable (see **Figure 5.3a**). All the conformations where the 'ethyl' moiety was almost parallel to the surface were less stable by less than 10 $kJmol^{-1}$. If we compare the most stable adsorption mode for the three butene isomers, we find that the 1-butene is the most stable by ~15 $kJmol^{-1}$. If we consider the energy per surface unit, the 1/4-ML is the best-adsorbed phase for the 1-butene molecule on the Pt surface. The adsorption energies computed for ethylene and propylene are ~ −104 $kJmol^{-1}$ and ~ −87 $kJmol^{-1}$ (see **Chapter 4**), respectively. These values are comparable to the present results of −96 $kJmol^{-1}$ for 1-butene and −80/−81 $kJmol^{-1}$ for 2-butene. Note that the adsorption energy decreased as the number of substituents on the double bond decreased, and that propylene and 1-butene had similar values. Delbecq and Sautet [34] have shown that alkyl substituents have two effects on molecular adsorption. Their electron-donating character raises the energy of the π molecular orbitals of ethylene. The π* orbital therefore moves further away from the top of the d band, thus decreasing the back-bonding interaction and the adsorption strength. The second effect is an increase in Pauli repulsion between occupied orbitals of the molecules and the surface, which results in a larger steric effect. For 1,3-butadiene, the interaction energy is −163 $kJmol^{-1}$. This is less than twice the adsorption energy of 1-butene or ethylene. In this case, in addition to steric effects, the resonance stabilizing the gas phase butadiene lowered the binding energy. This effect has also been reported for the interaction energy of benzene on Pt(111) [40]. The computed binding energy is around −88 $kJmol^{-1}$, which is much lower than three times the adsorption energy of ethylene.

The geometrical parameters in **Table 5.2** observed the same trends as for the 1,3-butadiene molecule. The molecules interact with the metal surface through their C=C bonds, which were longer than the gas phase distance. The geometry of the chemisorbed butenes is reminiscent of the geometry of propylene adsorbed on Pt(111) (**Chapter 4**). In

**Table 5.3.** Adsorption energies (kJmol$^{-1}$) for the various chemisorbed structures of 1,3-butadiene, 1-butene and 2-cis/trans-butene on Pd(111), as a function of the coverage

| θ | 1/3 | 1/4 | 1/6 | 1/9 |
|---|---|---|---|---|
| | | **1,3-butadiene** | | |
| di-π-cis | | | | −138(−15) |
| di-π-trans | | | −123(−21) | −145(−16) |
| di-σ | | −46(−11) | | −91(−10) |
| 1,2-di-σ-3,4-π | | −53(−13) | | −151(−17) |
| 1,4-di-σ-2,3-π | | | −130(−22) | −154(−17) |
| 1,2,3,4-tetra-σ | | | −145(−24) | −163(−18) |
| | | **1-butene** | | |
| π | −25(−8) | −41(−10) | −62(−10) | −75(−8) |
| di-σ | −25(−8) | −57(−14) | −70(−12) | −87(−10) |
| | | **2-cis-butene** | | |
| π | | | | −64(−7) |
| di-σ | | | | −74(−8) |
| | | **2-trans-butene** | | |
| π | | | | −56(−6) |
| di-σ | | | | −69(−8) |

The adsorption modes are those shown in Figures 5.1 and 5.3. The values in parenthesis are the adsorption energies per surface metal atom.

both cases, the unsaturated C=C bond lay almost parallel to the metal surface and the alkyl groups pointed outwards from the surface.

Unlike previous studies [6-8,13-15], which have indicated that stability is similar for 1,3-butadiene and 1-butene, our calculations predicted a smaller adsorption energy for the monoalkene than for the diene molecule at low coverages (-96 vs. –163 kJmol$^{-1}$). At high coverages (θ > 1/4 ML), repulsive interactions between adsorbed molecules forced the diene to adopt a more 'vertical' structure. The di-σ adsorption mode is the most likely. In this case, both 1,3-butadiene and 1-butene have similar adsorption structures and very similar adsorption energies (see **Table 5.2**). Similar results have been obtained by Mittendorfer *et al.* [16] using the same method and analogous models. These authors predict a decrease of ~70 kJmol$^{-1}$ in the energy difference between the diene and the monoalkene (-79 vs. -150 kJmol$^{-1}$ for 1-butene and 1,3-butadiene at 1/7 ML and ~-70 kJmol$^{-1}$ for both molecules at 1/4ML coverage).

### 5.2.3 Pd(111) surface

We characterised the adsorption (nature and strength) of 1,3-butadiene, 1-butene and 2-butenes on the Pd(111) surface in parallel. The adsorption structures on the Pd surface are

**Table 5.4**. Geometrical parameters for the adsorption structures of 1,3-butadiene, 1-butene and 2-cis/trans-butene on Pd(111) for a coverage of θ = 1/9-ML

| | **Pd–C$^1$** | **Pd–C$^2$** | **Pd–C$^3$** | **Pd–C$^4$** | **C$^1$–C$^2$** | **C$^2$–C$^3$** | **C$^3$–C$^4$** |
|---|---|---|---|---|---|---|---|
| **1,3-butadiene** | | | | | | | |
| di-π-cis | 2.17 | 2.25 | 2.25 | 2.17 | 1.41 | 1.46 | 1.41 |
| di-π-trans | 2.18 | 2.22 | 2.22 | 2.18 | 1.41 | 1.45 | 1.41 |
| di-σ | 2.11 | 2.17 | [2.81] | [3.64] | 1.45 | 1.46 | 1.35 |
| 1,2-di-σ-3,4-π | 2.11 | 2.19 | 2.34 | 2.15 | 1.45 | 1.45 | 1.42 |
| 1,4-di-σ-2,3-π | 2.11 | 2.26 | 2.26 | 2.11 | 1.45 | 1.43 | 1.45 |
| 1,2,3,4-tetra-σ | 2.12 | 2.23 | 2.25 | 2.11 | 1.45 | 1.45 | 1.45 |
| **1-butene** | | | | | | | |
| π | 2.20 | 2.22 | [3.20] | [4.61] | 1.40 | 1.51 | 1.54 |
| di-σ | 2.13 | 2.14 | [2.98] | [4.98] | 1.45 | 1.52 | 1.54 |
| **2-cis-butene** | | | | | | | |
| π | [3.29] | 2.24 | 2.24 | [3.29] | 1.50 | 1.41 | 1.50 |
| di-σ | [2.99] | 2.15 | 2.15 | [2.99] | 1.51 | 1.46 | 1.51 |
| **2-trans-butene** | | | | | | | |
| π | [3.09] | 2.23 | 2.23 | [3.05] | 1.51 | 1.41 | 1.51 |
| di-σ | [2.98] | 2.14 | 2.14 | [2.98] | 1.52 | 1.46 | 1.52 |

Distances are in Å. The numbers in brackets account for the distance between two atoms not directly bound.

the same as those on Pt (see **Figure 5.1** and **5.3**). **Table 5.3** shows the adsorption energies calculated for the various molecules. We also computed the adsorption energies using the **equation 2.41**. Generally, the Pd surface clearly stabilises the π modes better than the Pt surface (the differences in adsorption energy were less than 10–25 kJmol$^{-1}$).

*1,3-butadiene.* For 1,3-butadiene, the most favoured surface structure is again the 1,2,3,4-tetra-σ adsorption mode. Surprisingly, despite the different geometrical parameters the binding energy (-163 kJmol$^{-1}$) is equal to the one obtained on the Pt surface. The main structural details of the adsorption structures are shown in **Table 5.4**. The diene molecule is much less distorted on the Pd(111) surface than on the Pt surface and its geometry is closer to the gas phase. The terminal C–C bonds are only elongated by 0.11 Å, and the C–$CH_2$ angle was ~144º. This molecule contained two activated double bonds rather than two di-σ type interactions. This illustrates that the nomenclature π and σ is not directly related to the hybridisation of the organic molecule but to the nature of the molecule-surface interaction. Such a weakly distorted tetra-σ-adsorption mode with a remaining partial π character of the molecule could explain the NEXAFS results [6,15], which were previously assigned to a di-π mode. This weaker distortion of the molecular geometry on Pd(111) than on Pt(111) has been observed in previous calculations by Sautet and co-workers for the ethylene molecule [13]. It is useful to analyse the vibrational spectrum of adsorbed alkenes to determine the

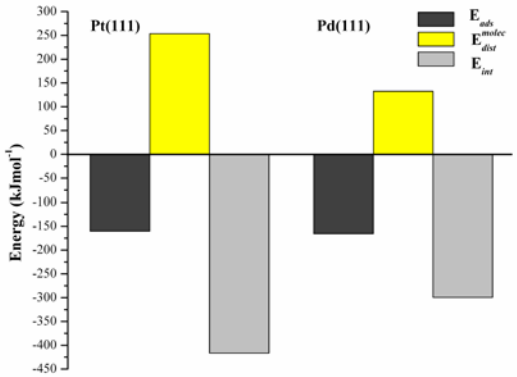


**Figure 5.4.** Decomposition of the adsorption energy for the most stable adsorption mode on the (111) surfaces of Cu, Pd, Pt, and Rh. Adsorption energy (dark grey), distortion energy of the molecule (yellow) and interaction energy (light grey).

state of hybridisation due to the sensitivity of the C=C stretching frequency to the hybridisation of the C atoms. In fact, in the calculated vibrational spectrum the C=C st mode appeared at 1120/1123 $cm^{-1}$ for 1,3-butadiene adsorbed on Pd compared with 1058/1068 $cm^{-1}$ for adsorption on Pt and 1600/1647 $cm^{-1}$ for gaseous $C_4H_6$. The closer the C=C st frequency of the adsorbed molecule to the value of the gas phase, the more $sp^2$ hybridised the C atoms. Differences between Pt and Pd are in agreement with the periodic trends for the adsorption of ethylene on Pt-group metals [41].To explain why the adsorption strength is the same when the geometry is so different, we broke up the adsorption energy into its main components (see **Figure 5.4)**. When the molecule interacted with the metal surface, new bonds are created and the geometry of the molecule and the surface changed. The adsorption energy is therefore partitioned into the distortion energy of the molecule, the distortion energy of the surface (a minor contribution not shown in the figure) and the interaction energy between the molecule and the surface. On the Pt(111) surface, the stronger distortion of the molecule led to a higher energy cost to reach the adsorption geometry (253 $kJmol^{-1}$ on Pt compared with 132 $kJmol^{-1}$ on Pd). The molecular distortion favours the interaction between the molecule and the metal surface. If we analyse the projected density of states (PDOS, **Figure 5.5**) of 1,3-butadiene in its most favoured configuration on both metal surfaces, we can see the bonding of the π states with the metal *d*-band. The interaction mainly takes place between the $p_z$ and the $dz^2$ band. The adsorbate-metal overlap is larger for Pt because the d states are more expanded (see the dotted line in **Figure 5.5**). The stabilisation due to molecule-surface interaction was greater on the Pt surface than on the Pd surface (–419 *vs.* –296 $kJmol^{-1}$). The greater elongation of the C=C bonds on Pt(111) compared to Pd(111) is clearly reflected in the PDOS. While peaks are discernible for the adsorption on Pd (arrows in **Figure 5.5**), the broadening of the corresponding states on Pt made it more difficult for peaks to be identified. As overall adsorption energy is a compromise between the distortion energy of the molecule and stabilisation due to the interaction between the molecule and the metal surface, the higher

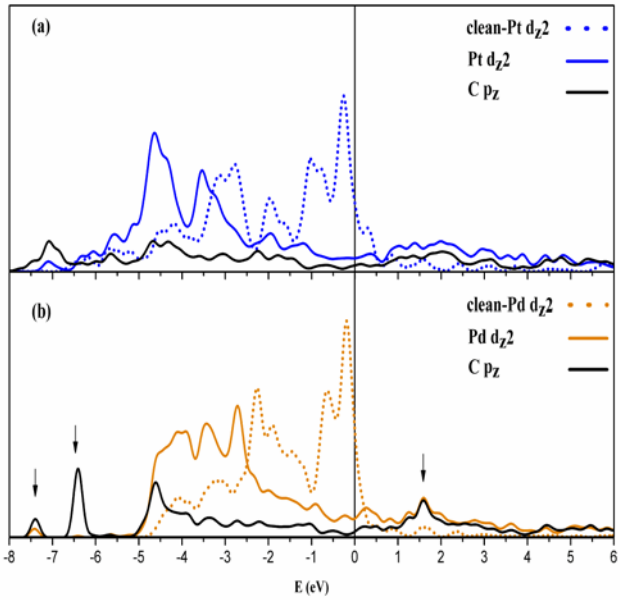


**Figure 5.5**. Projected density of states (PDOS) of 1,3-butadiene on Pt(111) (a) and Pd(111) (b).

energy cost needed to distort the molecule from its gas phase geometry on Pt(111) than on the Pd surface led to a similar adsorption energy on both metal surfaces. This explains why the adsorption energies of 1,3-butadiene on the Pt and Pd (111) surfaces are similar even though the adsorption geometries are quite different. Pt is clearly a case of strong interaction but also strong molecular distortion, while Pd is clearly a case of weaker interaction but with an overall adsorption that is at least as efficient.

*Butenes*. For all butene isomers, the preferred mode is the di-σ adsorption mode, but the difference in stability between this mode and the π mode is clearly smaller than on Pt(111) (**Table 5.3**). As with the 1,3-butadiene molecule, the adsorption geometry is closer to the gas phase than on Pt(111) and the differences between the di-σ and π adsorption geometries were clearly smaller (0.05 Å on Pd *vs*. 0.08 Å on Pt). Therefore, this moderately distorted di-σ structure on Pd kept a partial π character for the C–C bond, which is in agreement with the experimental data. These experiments have previously referred to a π adsorption mode for the molecule [6,15]. However, these results can be interpreted in a different way. Our results suggest that the molecule adsobs on the metal surface in a slightly distorted di-σ mode. We calculated the adsorption energy at different coverages for the 1-butene and 1,3-butadiene molecules. If we consider the adsorption energy per surface unit, again the preferred surface structures were the 1,2,3,4-tetra-σ adsorption mode with a coverage of 1/6-ML for the 1,3-butadiene and the di-σ mode with a coverage of 1/4-ML for the 1-butene molecule.

We need to consider two situations regarding the relative stabilities of butadiene and 1-butene. At low coverage ($\theta$ =1/9 ML), we predict a considerable difference (76 kJmol$^{-1}$) in the adsorption strength of the two molecules. Our calculations favour the butadiene. However, the increased coverage ($\theta$ =1/4 ML) destabilises the 1,3-butadiene molecule more than the 1-butene molecule. As observed on Pt(111), the difference in energy between these two molecules is dramatically reduced. The same findings have been previously reported by Mittendorfer *et al*. [16].

### 5.2.4 Pt(111) vs. Pd(111)

Although the electronic behaviour of the Pt and Pd surfaces is different, the adsorption modes are the same, with close adsorption energies for 1,3-butadiene and butenes on both metal surfaces. For the 1,3-butadiene molecule, the preferred adsorption structure is a tetra-$\sigma$ mode with the four C atoms bound to four neighbouring Pt atoms. In this surface structure the carbon chain remains almost parallel to the surface. The most stable adsorption mode for the butenes is the di-$\sigma$-mode. In the optimised geometry, the C=C bond lay parallel to the metal surface and the alkyl groups pointed outwards from the surface. However, on Pd(111) the molecules are less distorted than on the Pt surface. Moreover, the $\pi$ adsorption modes are less destabilised than the $\sigma$ modes on Pd(111). The difference in energy between the di-$\sigma$ and $\pi$ modes is therefore clearly smaller on palladium. If we compare the strength of the 1-butene adsorption to that of 1,3-butadiene on the Pt and Pd surfaces, we find almost no difference. In the low coverage situation, the energy gap between the most stable adsorption modes for both molecules is 67 kJmol$^{-1}$ on Pt(111) *vs.*76 kJmol$^{-1}$ on Pd(111). It is therefore difficult to relate the different selectivity only to this slight tendency (only 9 kJmol$^{-1}$) of Pd to provide a more facile butene desorption by competition with butadiene adsorption. Indeed it is unclear why Pt could not produce the same result. If we analyse the high coverage situation, we find that adsorption energy is very similar for 1-butene and 1,3-butadiene on both metal surfaces (see **Tables 5.1** and **5.3**). The desorption of butene is therefore no longer favoured and selectivity in butenes is expected to be poor on both Pt(111) and Pd(111).

In order to complete our results, we calculated the temperature-pressure phase diagrams using the approach proposed in **section 2.9**, **Chapter 2**. At UHV conditions (P= $1\cdot10^{-13}$ Pa), the most stable surface structure for 1,3-butadiene on Pt(111) is always the 1,2,3,4-tetra-$\sigma$ mode. Around 150–200 K the favoured phase corresponds to a 1/6 ML coverage (2x3 unit cell). This phase is the most stable one up to ~380 K. At this temperature, the 1/9 ML (3x3 unit cell) becomes the most favourable superstructure. Above T= 430 K no molecule remains on the surface. At reaction conditions (P= $1.10^{2}$ Pa), we observe the same behaviour but both the transition from the 2x3 phase to the 3x3 surface structure and the desorption take place at higher temperatures. For 1-butene adsorbed on Pt(111) the most stable adsorption mode is always the di-$\sigma$. At UHV conditions, the 1/4 ML superstructure is the most stable one up to 180 K. As the temperature increases, the 2x3 phase and the 3x3 superstructure stabilise. The temperature-pressure diagrams confirm that at a given pressure (UHV or reaction conditions from ref. [10,11]) the 1,3-butadiene is

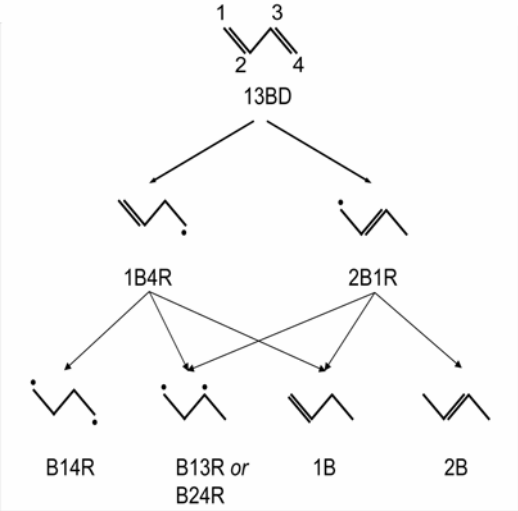


**Scheme 5.4.** 1,3-butadiene hydrogenation to $C_4H_8$ species via the Horiuti-Polanyi mechanism.

always more strongly adsorbed than 1-butene (see **Appendix A.5**). Thus, 1-butene will desorb until all the diene is not consumed.

The adsorption on the Pd(111) surface occurs in a similar way (see also **Appendix A.5**). At reaction conditions [7,9], temperature-pressure phase diagrams also predict that 1,3-butadiene more stabile than 1-butene and, consequently, a good selectivity to butenes.

To answer the problem of selectivity, it seems necessary to further study the hydrogenation reaction itself.

## 5.3 Hydrogenation of 1,3-butadiene on Pt(111) and Pd(111)

We carried out all the calculations presented in this section using a 3x3 unit cell (1/9 ML coverage).

### 5.3.1 $C_4H_x$ (x=7, 8) radical species

**Scheme 5.4** shows the network of steps by which 1,3-butadiene can be di-hydrogenated to a $C_4H_8$ species. We considered only the reaction pathways starting from the most stable surface structure (1,2,3,4-treta-σ). This is not a real limitation because the molecule can re-adapt its geometry before hydrogenation with the transition state research method used here [42]. The Horiuti-Polanyi mechanism (see **Scheme 5.4**) involves the

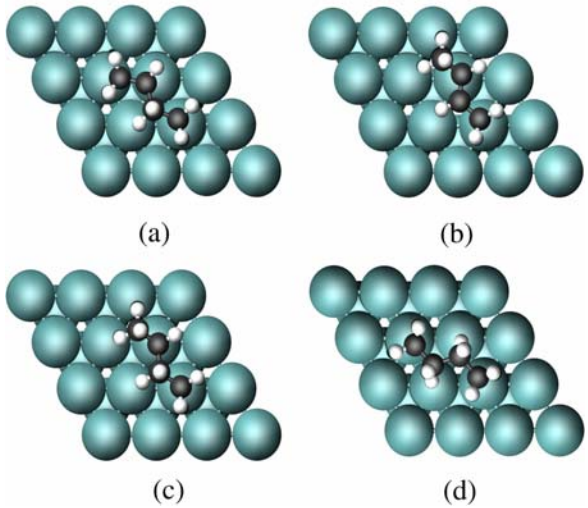


**Figure 5.6**. Adsorption modes for 1-buten-4-yl (1B4R, a), 2-buten-1-yl (2B1R,b), butan-1,3-diyl (B13R, c), butan-1,4-diyl (B14R, d) on Pd and Pt (111) metal surfaces.

initial formation of a $C_4H_7$ moiety and the subsequent hydrogenation to a $C_4H_8$ species. Addition of the first hydrogen atom produces only two intermediate radicals because the 1,3-butadiene molecule in the trans form belongs to the $C_2h$ point group. The H-addition on the $C^3$ (or $C^2$) atom produces the 1-buten-4-yl ($CH_2$=$CHCH_2CH_2^*$, 1B4R) and the H-addition on the $C^4$ (or $C^1$) produces the 2-buten-1-yl radical ($CH_2^*CH$=$CHCH_3$, 2B1R). For the sake of simplicity, the nomenclature used here follows the IUPAC conventions for gas phase radicals. In the abbreviated nomenclature, the first number accounts for the position of the 'remaining' double bond and the second one account for the number of the radical C atom, R simply indicates that the fragment is a radical in the gas phase. For both radicals (1B4R and 2B1R), there are three ways to add a second hydrogen atom. For 1-buten-4-yl, the addition on $C^1$ produces the butan-2,4-diyl ($CH_3CH^*CH_2CH_2^*$, B24R), the addition on $C^2$ produces a butan-1,4-diyl radical ($CH_2^*CH_2CH_2CH_2^*$, B14R) and the addition on $C^4$ produces the 1-butene species. The 2-buten-1-yl radical gives 2-butene, butan-1,3-diyl ($CH_2^*CH_2CH^*CH_3$, B13R) and 1-butene from $C^1$, $C^2$ and $C^3$ hydrogenation, respectively. Although they are obtained in different ways, the butan-2,4-diyl and the butan-1,3-diyl species are strictly equivalent. We will name this moiety butan-1,3-diyl (B13R) in accordance with the current nomenclature.

**Figure 5.6** shows the most stable adsorption modes for 1-buten-4-yl, 2-buten-1-yl, butan-1,3-diyl and butan-1,4-diyl radicals. These structures can be characterised as 1,2,4-tri-σ (**Figure 5.6a**), 1-σ-2,3-π (**Figure 5.6b**), 1,3-di-σ (**Figure 5.6c**) and 1,4-di-σ (**Figure 5.6d**). Both di-radicals form a so-called metallacycle. This adsorption structure is common for di-haloalkanes of general formula $CH_3CHX(CH_2)_nCH_2X$ (n=1,2) dissociatively adsorbed in ultrahigh vacuum [25-27]. The most important geometrical parameters and the relative adsorption energies are shown in **Table 5.5**. Obviously, a radical moiety cannot

**Table 5.5.** Relative adsorption energies ($E_{ads}$ , kJmol$^{-1}$) and relevant geometrical parameters (metal-carbon, M-C, and carbon-carbon, C-C, distances in Å) for the different $C_4H_x$ (x= 7–8) species adsorbed on Pt(111) and Pd(111)

| molecule | $E_{ads}$ | M–C$^1$ | M–C$^2$ | M–C$^3$ | M–C$^4$ | C$^1$–C$^2$ | C$^2$–C$^3$ | C$^3$–C$^4$ |
|---|---|---|---|---|---|---|---|---|
| | | | | **Pt(111)** | | | | |
| 1-buten-4-yl | –131 | 2.10 | - | 2.14 | 2.13 | 1.49 | 1.52 | 1.52 |
| 2-buten-1-yl | –148 | 2.10 | 2.33 | 2.19 | - | 1.46 | 1.42 | 1.50 |
| butan-1,3-diyl | –125 | 2.09 | - | 2.12 | - | 1.52 | 1.52 | 1.52 |
| butan-1,4-diyl | –80 | 2.11 | - | - | 2.11 | 1.53 | 1.54 | 1.53 |
| | | | | **Pd(111)** | | | | |
| 1-buten-4-yl | –86 | 2.07 | - | 2.15 | 2.14 | 1.45 | 1.52 | 1.52 |
| 2-buten-1-yl | –128 | 2.10 | 2.34 | 2.17 | - | 1.44 | 1.42 | 1.50 |
| butan-1,3-diyl | –48 | 2.07 | - | 2.10 | - | 1.51 | 1.51 | 1.51 |
| butan-1,4-diyl | –18 | 2.09 | - | - | 2.09 | 1.52 | 1.54 | 1.52 |

exist as such in gas phase. Adsorption energies are expressed with respect to the 1,3-butadiene molecule in the gas phase and the adsorbed hydrogen in order to compare the adsorbed species.

$$E_{ads} = (E_{C_4H_x/surface} - E_{surface} - E_{C_4H_{6(g)}}) - (x-6)(E_{H/surface} - E_{surface}) \quad (5.1)$$

Especially for butan-1,3-diyl, the Pt(111) surface stabilises the radical species more than the Pd surface, i.e. the adsorptions energies are higher on Pt(111) than on Pd. However, the trends are similar on both metal surfaces. The most stable species is the 2-buten-1-yl intermediate, followed by 1-buten-4-yl, butan-1,3-diyl and the butan-1,4-diyl radical. Note that 2-buten-1-yl is stabilised by 42 kJmol$^{-1}$ with respect to the 1-buten-4-yl on the Pd surface while the difference is only 17 kJmol$^{-1}$ on the Pt(111). The di-radical species are much less stable than the mono-radical moieties on Pd(111), while the difference is much smaller on the Pt(111) surface. However, we should take into account that this difference also includes the difference in the adsorption energy of the hydrogen atom on these metals (–48 kJmol$^{-1}$ on Pt vs. –67 kJmol$^{-1}$ on Pd). This value (~20 kJmol$^{-1}$) helps to explain the marked gap between $C_4H_6$ and the mono- and di-hydrogenated species found on Pd(111). As our aim is to study the hydrogenation of 1,3-butadiene to the different $C_4H_8$ species, we compare the adsorption energy of the di-radicals to that of the butene molecules (e.g. 1-butene). The relative adsorption energies for 1-butene are –136 kJmol$^{-1}$ and –89 kJmol$^{-1}$ on Pt(111) and Pd(111), respectively. The butan-1,3-diyl radical is only 11 kJmol$^{-1}$ less stable than 1-butene on platinum while on palladium the difference is 40 kJmol$^{-1}$. The energy difference increases dramatically if we consider the 1,4-di-radical (55 kJmol$^{-1}$ and 71 kJmol$^{-1}$ on Pd). We will therefore not consider the butan-1,4-diyl radical in our study of the possible reaction pathways.

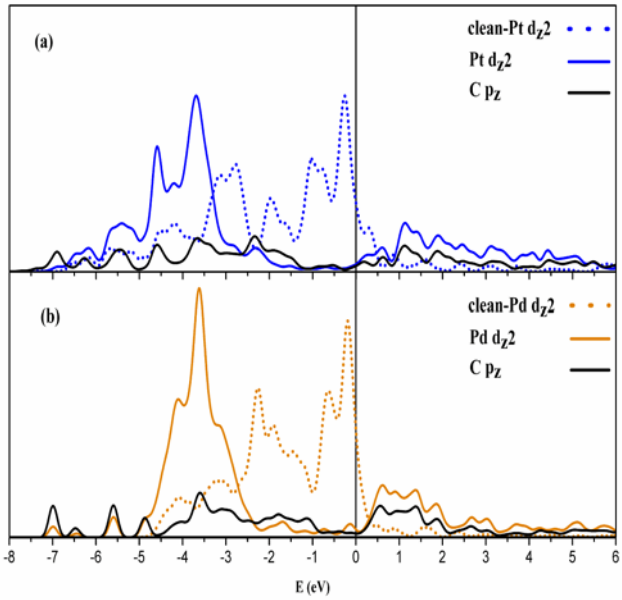


**Figure 5.7.** Projected Density of States (PDOS) for butan-1,3-diyl on Pt(111) (a) and Pd(111) (b).

The adsorption geometries of the radical intermediates follow the same trends as those of 1,3-butadiene and butenes. In general, there is no clear difference between the metal-carbon (M–C) and C–C bond distances of the two metal surfaces except for C–C bonds that directly interacted with the metal surface of the mono-radical species. In fact, the $C^1$–$C^2$ bond distance of the 1-buten-4-yl molecule is 1.45 Å on Pd and 1.49 Å on Pt. The same result is found for 1,3-butadiene in its di-σ adsorption mode. Moreover, the $C^1$–$C^2$ bond of the 2-buten-1-yl intermediate is also shorter on Pd than on Pt and, more importantly, the difference between the $C^1$–$C^2$ bond and the $C^2$–$C^3$ bond is smaller in Pd than in Pt which indicates a more allylic adsorption mode. Similarly, the difference in the $C^1$–$C^2$ and $C^2$–$C^3$ bond distances increases from 0.02 Å on Pd to 0.05 Å on the Pt surface for 1,3-butadiene di-σ-π adsorbed. The allylic character of the adsorption structure could be responsible for the extra stabilisation for the 2-buten-1-yl radical on Pd (see above discussion on adsorption energies). No significant differences are observed for the C–H distances (~1.10 Å). All the C–C distances in the di-radical species are within the 1.52-1.54 Å range. Clearly, all the C atoms had an $sp^3$ hybridisation. The C–H distances are ~1.10 Å except for the $C^3$–H and $C^4$–H bonds of the butan-1,4-radical that pointed directly to the metal surface (1.13 Å). This suggests that these bonds are slightly activated due to agostic interaction with the metal surface (the M–H distance was only about 2.12 Å).

Before continuing the study of the reaction mechanism itself, we will analyse the interaction of butan-1,3-radical and 1-butene in greater detail. The adsorption energy of the butan-1,3-diyl radical with respect to the molecule in the gas phase is –365 $kJmol^{-1}$ on

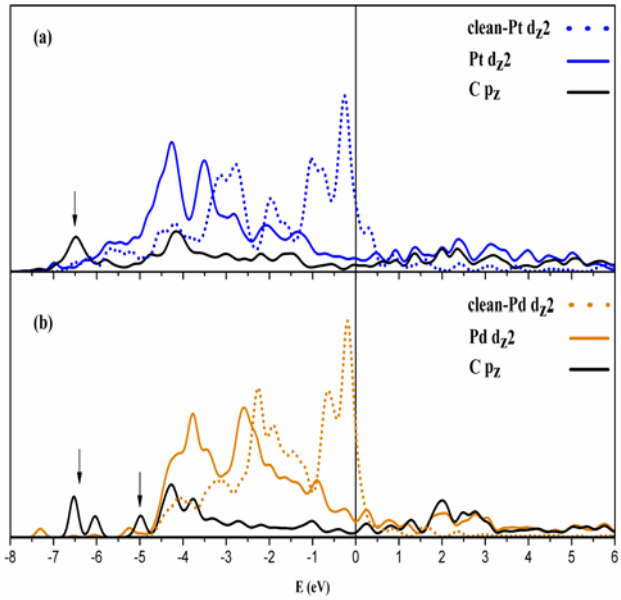


**Figure 5.8.** Projected Density of States (PDOS) for 1-butene on Pt(111) (a) and Pd(111) (b). Here, arrows show the peaks resulting from the interaction of the $Cp_z$ orbital with the $Md_{xz}$ and $Md_{yz}$.

Pt(111) and –327 kJmol$^{-1}$ on Pd(111). For the 1-butene molecules it is –96 and –87 kJmol$^{-1}$ on Pt and Pd, respectively. The di-radical species on the Pt(111) surface clearly stabilises. Comparing the projected density of states (PDOS) curves (see **Figure 5.7** and **5.8**) helps us to understand these differences. The di-radical intermediate adsorbs on both metal surfaces to form a five-atom metallacycle structure. In this adsorption mode, the carbon atom directly points to a surface metal atom. Therefore, the interacting orbitals are mainly $d_z^2$ for the metal atoms and $p_z$ for the carbon. On interaction, there is a splitting of the $dz^2$ band (see **Figure 5.7**). The occupied part of the band is pushed downward and the empty part appears above the Fermi level (taken as zero). The d-band centre below the Fermi level is placed at –4.08 eV and –3.56 eV for platinum and palladium, respectively. Above the Fermi level, the d-band centre is located at 2.49 eV (2.17 eV) for the Pt (Pd) surface. Obviously, these values produce a larger splitting on Pt(111) (6.57 eV) than on Pd (5.73 eV). This result is consistent with the greater stability of the di-radical species on Pt(111) than on Pd(111). Two reasons can explain this difference: first, the smaller 4d orbital expansion of Pd, as seen from the narrower d-band in bulk, leads to a smaller surface-molecule overlap; second, the higher energy of the d states for Pd (more electropositive metal) increases the energy difference between them and C:$p_z$, which decreases the interaction.

The picture for butene species is quite similar. The interaction takes place primarily between the $p_z$ orbital of the C atom and the $d_z^2$ band of the metal surface (see PDOS, **Figure 5.8**). However, there is a non-negligible contribution by $d_{xz}$ and $d_{yz}$ (peaks marked

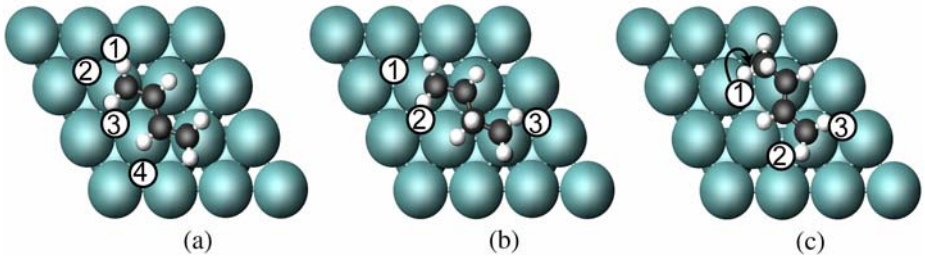


**Figure 5.9.** Initial hydrogen position in the co-adsorbed system. 13BD + H (a), 1B4R +H (b) and 2B1R +H (c).

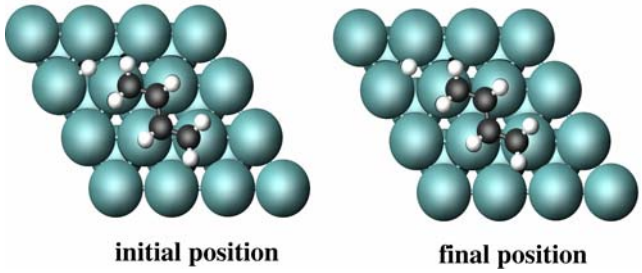


**Figure 5.10.** Movement of the hydrogen atom during the geometry optimisation.

with an arrow in the PDOS curves are due to these interactions, **Figure 5.8**). The $C^1$–$C^2$ bond is parallel above a metal-metal bond. This allows for a better overlap between C:pz and these bands. A considerable splitting is observed in the $d_z^2$ band upon adsorption of the butene molecule, though this is not as obvious as with the di-radical adsorption. Again the difference in energy between the centre of the $d_z^2$ band above and below the Fermi level is larger on the platinum surface (by 0.9 eV). Electronic interaction is therefore again greater on Pt than on Pd. However, the adsorption energy of 1-butene on Pt(111) and Pd(111) differed by only 9 $kJmol^{-1}$ compared with a difference of 38 $kJmol^{-1}$ for the di-radical. To explain these differences we break up the adsorption energy into its main components. These are the distortion energy of the molecule, the distortion energy of the surface and the interaction between adsorbate and substrate. For the butan-1,3-diyl radical, the difference in the distortion of the species and the surface on both metal surfaces is less than 9 $kJmol^{-1}$. The interaction energy between the di-radical and the surface is therefore higher on Pt (–434 $kJmol^{-1}$) than on Pd (–380 $kJmol^{-1}$). For 1-butene, the energy cost for distorting the molecule from its geometry in the gas phase to its adsorption geometry is 51 $kJmol^{-1}$ lower on Pd(111). The higher distortion energy on Pt is consistent with the stronger hybridisation and the greater elongation of the $C_1C_2$ bond on adsorption (see **Tables 5.2** and **5.5**). This is also observed in the PDOS curve (**Figure 5.8**) where the broadening of the C:pz states is greater on Pt than on Pd. As the distortion energy of the surface is similar for both surfaces, the energy interaction is 66 $kJmol^{-1}$ stronger on platinum than on palladium (–260 *vs.* –194 $kJmol^{-1}$, respectively).

### 5.3.2 Co-adsorption of $C_4H_x$ (x=6,7) species and hydrogen

The next step towards understanding the hydrogenation of 1,3-butadiene was to examine the interaction between the hydrocarbon and the hydrogen atom. We calculated the co-adsorption of 1,3-butadiene, 1-buten-4-yl and 2-buten-1-yl and hydrogen for several configurations on both metal surfaces. **Figure 5.9** depicts the hydrocarbon adsorption geometries and shows the initial hydrogen positions. The $C_4H_x$ species was placed in its more stable adsorption site and hydrogen was placed in a neighbouring 3-fold hollow site close to the C atom to be hydrogenated. On co-adsorption there are no significant changes in the geometry of the $C_4H_x$ moiety. However, the picture for the H atom is quite different. On palladium, all the positions surrounding the organic molecule are stable. On the other hand, in the case of platinum, the hydrogen atom moves on the metal surface from the 3-fold hollow site closest to the hydrocarbon moiety (the H atom and the $C_4H_x$ species shared at least one of the surface metal atoms) to a *quasi* bridge position (one of the metal-hydrogen bonds is elongated by about 0.15 Å) or to a neighbouring hollow site. In **Figure 5.10**, we plot the adsorption geometry for the co-adsorption of 1,3-butadiene and hydrogen on position 2, before and after the optimisation process. We can clearly see that the hydrogen atom moves towards a bridge position. In fact, the height of H above the surface is ~0.9 Å. This value is in between of those for hollow (0.8 Å) and bridge (1.0 Å) positions. This is a consequence of the well-known high mobility of H atom on both metal surfaces [43].The energy differences of the co-adsorption state with respect to the individual adsorptions of the hydrocarbon and hydrogen [44] are not negligible (around 15–30 $kJmol^{-1}$). These results are very similar to those for ethylene [23] and acetylene [45] hydrogenation.

Among the positions tested, the most stable ones were used as initial configurations for the reaction pathway searches (see **Appendix A.6**). For the sake of comparison, in the next section we provide some geometrical parameters of the co-adsorbed states.

### 5.3.3 Reaction pathways and activation barriers

**Figure 5.11** shows the reaction profiles starting from the reactant ($C_4H_6$) to provide the product species ($C_4H_8$) on the Pt(111) surface. The reference line (zero level) is the adsorbed 1,3-butadiene and two adsorbed hydrogen atoms (without interaction). We did not consider zero point energy (ZPE) corrections to calculate the activation barriers. Some test calculations showed that the contribution of ZPE to the activation energies is less than 1 $kJmol^{-1}$ on both metal surfaces. The only noticeable effect is the destabilisation of the second hydrogenation transition states (by 30 $kJmol^{-1}$) compared to the first hydrogenation saddle points. Geometries of the transition states determined are shown in **Figure 5.12a-g**. In all cases the basic structure of the activated complex is a three-centre Pt–C–H intermediate. Whereas the C–H bond is formed, both the Pt–H and Pt–C are broken. Somehow the hydrogen atom is inserted into the C–Pt bond. Obviously, the Pt–C, C–H and

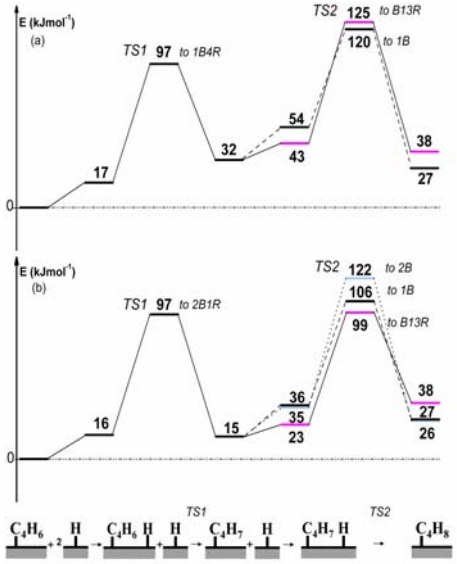


**Figure 5.11.** Butadiene hydrogenation energy profile on the Pt(111) surface via 1-buten-4-yl (1B4R, a) and 2-buten-1-yl (2B1R, b) intermediates. For sake of clarity, the second hydrogenation step is drawn in a different colour depending on the final product: butan-1,3-diyl radical (pink), 1-butene (black) and 2-butene (light blue).

Pt–H bond distances characterise the activated complex (see **Table 5.6**). Generally, the shorter is the C–H distance the later is the transition state.

As we explained in **section 5.3.1**, this reaction can take place via two intermediate $C_4H_7$ species: 1-buten-4-yl (**Figure 5.11a**) and 2-buten-1-yl (**Figure 5.11b**). For the hydrogenation of 1,3-butadiene to 1-buten-4-yl (13BD → 1B4R, see **Figure 5.12a**), as the C–H bond formed, the C–H distance decreased from 2.83 Å in the co-adsorption state to 1.65 Å. The Pt–C distance in the saddle point increased from 2.19 Å to 2.42 Å, which indicates that a clear weakening of the Pt–C bond. The computed TS energy is 97 kJmol$^{-1}$ above the zero level, and the reaction barrier with respect to the co-adsorbed reactants (intrinsic barrier) is 80 kJmol$^{-1}$. For 13BD → 2B1R (see **Figure 5.12b**), the transition state is relatively early with respect to the C–H stretch (1.57 Å). Moreover, the hydrocarbon moiety remains quite flat while the hydrogen atom is inserted into the Pt–C bond. While the C–H bond forms, the Pt–C is broken (the Pt–C distance in the TS is 2.28 Å compared with 2.19 Å in the initial state). The calculated energy for the saddle point is again 97 kJmol$^{-1}$, with an intrinsic activation barrier of 81 kJmol$^{-1}$. No preference for one of the possible 'first steps' can be inferred from these results.

**Table 5.6.** Energy ($E_{TS}$, kJmol$^{-1}$) and the most outstanding structural parameters (metal-hydrogen, M-H, carbon-hydrogen, C-H, and metal-carbon, M-C, distances in Å) of the transition states for the 1,3-butadiene hydrogenation on Pt(111) and Pd(111)

| Transition State | $E_{TS}$ | M–H | C–H | M–C |
|---|---|---|---|---|
| **Pt(111)** | | | | |
| 1,3-butadiene → 1-buten-4-yl | 97 | 1.60 | 1.65 | 2.42 |
| 1,3-butadiene → 2-buten-1-yl | 97 | 1.61 | 1.57 | 2.28 |
| 1-buten-4-yl → butan-1,3-diyl | 125 | 1.61 | 1.60 | 2.32 |
| 1-buten-4-yl → 1-butene | 120 | 1.64 | 1.49 | 2.30 |
| 2-buten-1-yl → 2-butene | 122 | 1.65 | 1.49 | 2.27 |
| 2-buten-1-yl → butan-1,3-diyl | 99 | 1.63 | 1.62 | 3.04 |
| 2-buten-1-yl → 1-butene | 106 | 1.93 | 1.42 | 2.46 |
| **Pd(111)** | | | | |
| 1,3-butadiene → 1-buten-4-yl | 132 | 1.61 | 1.57 | 2.38 |
| 1,3-butadiene → 2-buten-1-yl | 96 | 1.73 | 1.50 | 2.31 |
| 1-buten-4-yl → butan-1,3-diyl | 175 | 1.72 | 1.52 | 2.34 |
| 1-buten-4-yl → 1-butene | 155 | 1.71 | 1.57 | 2.24 |
| 2-buten-1-yl → 2-butene | 134 | 1.75 | 1.49 | 2.31 |
| 2-buten-1-yl → butan-1,3-diyl | 159 | 1.72 | 1.40 | 3.06 |
| 2-buten-1-yl → 1-butene | 120 | 1.81 | 1.46 | 2.36 |

The second hydrogenation is rather more complex. Butan-1,3-dyil and 1-butene species are obtained from the 1-buten-4-yl radical. The energy of the activated complex for 1B4R → B13R (**Figure 5.12c**) is 125 kJmol$^{-1}$ and 82 kJmol$^{-1}$ from the co-adsorbed state. In the Pt–C–H intermediate, the C–H distance is 1.49 Å, the Pt–H distance is 1.64 Å and the Pt–C bond length is 2.30 Å. The TS that connects 1-buten-4-yl to 1-butene (1B4R → 1B) is shown in **Figure 5.12d**. The structure is similar to that for the butan-1,3-diyl radical. Here, the C–H, Pt–H and Pt–C bond lengths are 1.49, 1.64 and 2.30 Å, respectively. The 1-butene transition state is only 5 kJmol$^{-1}$ more stable than for the di-radical (120 *vs.* 125 kJmol$^{-1}$). Therefore, both reaction pathways may be competitive. The picture for the second hydrogenation from the 2-buten-1-yl radical has strong similarities with the above transition states above. From 2-butem-1-yl radical, we can obtain three different products: 2-butene, butan-1,3-diyl and 1-butene. For 2B1R → 2B (see **Figure 5.12e**), the Pt–C bond length increases from 2.11 Å to 2.27 Å while the C–H distance decreases from 2.43 to 1.49 Å. Although the TS is late with respect to the C–H stretch (1.49 Å), its adsorption site is closer to the initial sate. To reach the final state (2-butene in a di-σ adsorption mode), the molecule has to rearrange itself (the methyl group has to move upwards) and change its adsorption site (from the π to the di-σ adsorption mode). The energy of the TS is 122

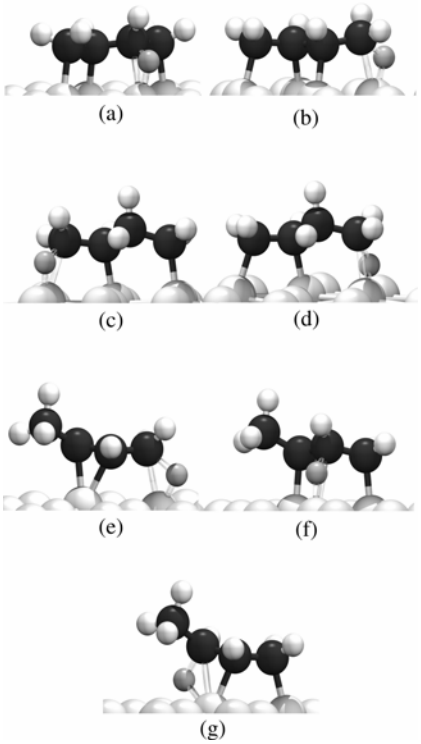


**Figure 5.12.** Transition state structures for the 1,3-butadiene hydrogenation on Pt(111): 13BD to 1B4R (a), 13BD to 2B1R (b), 1B4R to B13R (c), 1B4R to 1B (d), 2B1R to 2B (e), 2B1R to B13R (f), 2B1R to 1B(g). The reactive H atom is drawn in gray.

kJmol$^{-1}$. If we consider the barrier from the reactant state, the energy decreases to 87 kJmol$^{-1}$. For 2B1R → B13R (**Figure 5.12f**), the TS is near to the final adsorption site, though the C–H bond length is quite long (1.62 Å). The absolute energy of this saddle point is 99 kJmol$^{-1}$ (intrinsic barrier: 76 kJmol$^{-1}$). Finally, the transition state for 2B1R → 1B (**Figure 5.12g**) is also a late saddle point. The structure of the hydrocarbon moiety is close to the final state. The Pt–C distance is 2.42 Å and the C–H is only 1.42 Å (compared to 2.17 and 2.65 Å in the initial state). The saddle point energy is 106 kJmol$^{-1}$ above the zero level (or 70 kJmol$^{-1}$ with respect to the co-adsorption state).

A clear trend emerges from the structure of the transition states. TS leading from a radical to a closed-shell fragment are late, with a short C–H bond (1.42–1.49 Å) and an already broken Pt–H bond (1.64–1.93 Å). The C–H bond formation process stabilises the radical fragment and overall this step is exothermic or neutral. On the other hand,

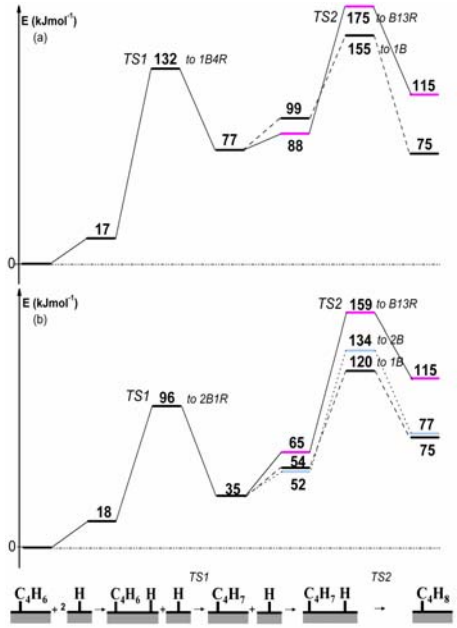


**Figure 5.13.** Butadiene hydrogenation energy profile on the Pd(111) surface via 1-buten-4-yl (1B4R, a) and 2-buten-1-yl (2B1R, b) intermediates. For sake of clarity, the second hydrogenation step is drawn in a different color depending on the final product: butan-1,3-diyl radical (pink), 1-butene (black) and 2-butene (light blue).

transitions from closed-shell fragments to radicals are early and endothermic, although this effect is reduced for the formation of 2-buten-1-yl since the radical is stabilised by conjugation. Radical to di-radical transition states are intermediate.

From these results we can conclude that no reaction pathway on the Pt(111) surface is favoured. The hydrogenation may take place via both the 1-buten-4-yl and the 2-buten-1-yl intermediates. Similar energies are found for all second hydrogenation transition states (the differences are less than 26 kJmol$^{-1}$). In the case of the pathways leading to butenes, the TS energies are consistent with a predominant formation of 1-butene (106 and 122 kJmol$^{-1}$ for the formation of 1-butene and 2-butene, respectively). We have only calculated the pathways leading to *trans*-2-butene. Experimentally, *cis*-2-butene is obtained in almost equal quantities and the relative amount of the two isomers depends on the reaction conditions [10,11]. One could assume that the hydrogenation pathways leading to the *cis* isomer are very similar to those described above. Moreover, butene isomers are not the only surface species possible in the 1,3-butadiene hydrogenation: the butan-1,3-diyl radical is also a possibility. In fact, the saddle point leading to butan-1,3-diyl from 2-buten-1-yl (

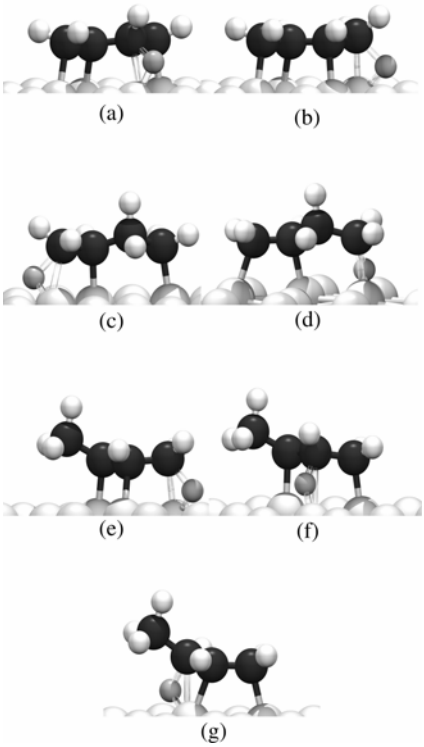


**Figure 5.14.** Transition state structures for the 1,3-butadiene hydrogenation on Pd(111): 13BD to 1B4R (a), 13BD to 2B1R (b), 1B4R to B13R (c), 1B4R to 1B (d), 2B1R to 2B (e), 2B1R to B13R (f), 2B1R to 1B(g). The reactive H atom is drawn in gray.

2B1R → B13R) is the most stable one (99 kJmol$^{-1}$). This di-radical species may continue to react, which explains the primary formation of butane observed on platinum surfaces [24].

We characterised the reaction pathways (**Figure 5.13**) on Pd(111) in parallel. The transition state structures for 1,3-butadiene hydrogenation on Pd have some strong similarities with those on the Pt surface (see **Table 5.6**), though important differences are also found. In all cases, the basic structure of the transition state is again a three-centre cyclic intermediate (Pd–C–H).

For the first hydrogenation step, the TS states to the mono-radical intermediates are similar to those for Pt(111). The hydrocarbon moiety remains flat on the metal surface and the C–H and Pd–C distances are about 1.60 and 2.30 Å, respectively (**Table 5.6**). However, the difference in energy between these two transition states is 36 kJmol$^{-1}$ (**Figure 5.13**).

Obviously, the pathway via the 2-buten-1-yl (intrinsic barrier, 78 $kJmol^{-1}$) intermediate seems to be more favoured than the one through the 1-buten-4-yl (intrinsic barrier, 115 $kJmol^{-1}$). This important difference could be due to the poorer stability of the 1-buten-4-yl intermediate on the Pd(111) surface.

The same trends found for the first hydrogenation are also found for the second stage. The structures of the transition states are analogous to the ones obtained on Pt. There are minor differences in the C–H and M–C bond lengths i.e. under 0.1 Å (see **Table 5.6** for comparison). Only the activated complex for 2B1R → 2B is slightly shifted from its π coordination on Pt (**Figure 5.12e**) to a more di-σ co-ordination on Pd (**Figure 5.14e**). The main differences involve the saddle point energies. Clearly, the paths leading to the butene isomers (especially to 1-butene) are quite favoured on the palladium surface. The minimum energy profile occurs via the 2-buten-1-yl intermediate and leads to the 1-butene molecule. The path to the 2-butene species requires 14 $kJmol^{-1}$ more to overcome the second hydrogenation barrier. Although we may consider that hydrogenation to the *cis*-2-butene species is similar to the reaction leading to the *trans* isomer, the *trans/cis* ratio observed experimentally is quite high. The clear difference has been attributed to the low conformational interconversion of adsorbed species [9]. Both transition states leading to the butan-1,3-diyl radical are less stable than the most stable state by 39–55 $kJmol^{-1}$ (120 $kJmol^{-1}$ for the 2B1R → 1B transition state). If we take into account the possible limitations of the DFT approach, this difference is large enough to be conclusive. On the Pd(111) surface the formation of the di-radical species seems unlikely. Therefore, no alternative path to obtain butane is possible and this alkane can be obtained only by subsequent hydrogenation of butene species formed as an initial product.

## 5.4 Conclusions

In conclusion, we determined binding modes for 1,3-butadiene and butene isomers on Pt(111) and Pd(111). For 1,3-butadiene on Pt(111), by combining total energy calculations and simulations of the vibrational spectra, we observed that the most favoured molecular adsorption mode is 1,2,3,4-tetra-σ and reconciled the divergent proposals in the literature. On the Pd(111) surface, previuous studies suggested a di-π adsorption mode. Our calculations yielded a σ-type interaction with moderate molecular distortion, which is fully compatible with the experimental results. For butenes, our calculations indicated a di-σ adsorption mode on both metal surfaces. From experiments this has been anticipated for Pt but not for Pd, where a π mode has been predicted. As with the 1,3-butadiene molecule, the fact that molecular geometry is only slightly distorted on adsorption on Pd(111) shows that our calculations are compatible with the experimental results.

This study shows that the different selectivities for the butadiene hydrogenation on Pt(111) and Pd(111) cannot be explained only by a competition between 1,3-butadiene and 1-butene. If we compare the strength of the 1-butene adsorption to that of 1,3-butadiene on Pt and Pd, only small differences are observed. These results provided us a good starting point for the study of the reactivity.

The natural chemical pathway to hydrogenate butadiene is to conserve a double bond by forming butene (1-butene from 1-2 attack or 2-butene by 1-4 attack). The 1-3 (or 2-4) attack leads to a di-radical species, butan-1,3-diyl, which is very unstable in the gas phase. Our calculations show that this di-radical is strongly stabilised by the interaction with the catalytic surface (especially on the Pt(111) surface).

The pathway towards the butan-1,3-diyl radical becomes competitive with those leading to butenes in the case of Pt catalyst. The transformation (13BD → 2B1R → B13R) is indeed associated with the lowest activation barrier (99 $kJmol^{-1}$), but the pathway to 1-butene (13BD → 2B1R → 1B) is only 7 $kJmol^{-1}$ higher. From the typical error bars in such calculations, it is only possible to conclude here that these two pathways are equally probable. The formed butene will desorb as long as butadiene is present in the gas phase since the adsorption of butadiene is strongly favored. The di-radical species will be further hydrogenated, leading to the formation of butane as primary product and to an incomplete selectivity to butene. This is in good agreement with the partial selectivity (60%) to butene observed on Pt(111) and with the presence of butane right from the beginning of the reaction.

Although the butan-1,3-diyl is also stabilised on Pd(111), this effect is smaller than on Pt(111) and the pathway toward this radical is not accessible, with a transition state 39 $kJmol^{-1}$ less stable than that of 1-butene. Taking into account all possible sources of error, this energy difference is large enough to categorically exclude this transformation (13BD → 2B1R → B13R) on Pd(111). Calculations hence predict a full selectivity to butene in agreement with the experiment.

Moreover, the pathway to 1-butene has a lower activation energy than the one to 2-butene on both metals, in agreement with the observed distribution of products.

The smaller stabilization of the 1-3 di-radical on Pd(111) compared to Pt(111) can be qualitatively explained by the analysis of the one-electron states and related to the smaller expansion of the 4d orbitals of Pd (*vs*. 5d of Pt).

These results on the example of butadiene shed light on the factors which control activity and selectivity of a catalyst. It is well known that the key role of a catalyst is to stabilise unstable gas phase species, such as intermediates or transition states, in order to allow a lower energy profile transformation. Here, the key step is to stabilise the mono-hydrogenated intermediates 1-buten-4-yl and 2-buten-1-yl radicals. However by the same mechanism, the catalyst can also stabilise the di-radical isomers of the butene product. A selective reaction implies that the consecutive elementary steps must occur in a controlled way. Otherwise, the occurrence of side reactions leads to a poor selectivity. Therefore, an optimum catalyst for the 1,3-butadiene hydrogenation must reach a compromise between the stabilization of key intermediates and transition states and the strength of chemisorption of the unwanted di-radical intermediates.

## 5.5 References and Notes

[1] J. Horiuti, M. Polanyi, *Trans. Faraday Soc.* 30 (1934) 1164; J. Horiuti, M. Polanyi, *J. Mol. Catal. A Chem.* 199 (2003) 185.

[2] G.C. Bond *Catalysis by Metals*; Academic Press: London ,1962.
[3] G.C. Bond, P.B. Wells, *J. Catal*. 6 (1966) 397.
[4] J. Margitfalvi, L. Guczi, A.H. Weiss 15 (1980) React. *Kinet. Catal. Lett*. 475.
[5] Cosyns, in: *Catalyse par les Métaux*, Eds. B. Imelik, G.A. Martin, A. J. Renouprez, (Edition du CNRS, Paris, 1984) 371.
[6] G. Tourillon, A. Cassuto, Y. Jugnet, J. Massadier, J.C. Bertolini, *J. Chem. Soc. Faraday Trans*. 92 (1996) 4835.
[7] J. Massadier, J.C. Bertolini, A. Renouprez, Proc. 9th Int. Congress on Catalysis, Calgary, 1988, Eds. M.J. Phillips, M. Ternan, Vol. III, p. 1222.
[8] T. Ouchaib, J. Massadier, A. Renouprez, *J. Catal*. 119 (1989) 517.
[9] J. Goetz, D. Y. Murzin, R.A. Touroude, *Ind. Eng. Chem. Res*. 35 (1996) 703.
[10] C. Yoon, M.X. Yang, G.A. Somorjai, *Catal. Lett*. 46 (1997) 37.
[11] C-M. Pradier, E. Margot, Y. Berthier, J. Oudar, *Appl. Catal*. 43 (1988) 177.
[12] V. Maurice, C. Minot, *Langmuir* 5 (1989) 734.
[13] P. Sautet, J.-F. Paul, *Catal. Lett.* 9 (1991) 245.
[14] M. Abon, J. C. Bertolini, B. Tardy, *J. Chim. Phys.* 85 (1988) 711.
[15] J. C. Bertolini, A. Cassuto, Y. Jugnet, J. Massardier, B. Tardy, G. Tourillon, *Surf. Sci*. 349 (1996) 88.
[16] F. Mittendorfer, C. Thomazeau, P. Raybaud, H. Toulhoat, *J. Phys. Chem. B* 107 (2003) 12287.
[17] R. Avery, N. Sheppard, *Proc. R. Soc. Lond. A* 405 (1986) 27.
[18] R. C. Baetzold, *Langmuir* 3 (1987) 189.
[19] R. Avery, N. Sheppard, *Proc. R. Soc. Lond. A* 405 (1986) 1.
[20] A. Cassuto , G. Tourillon, *Surf. Sci*. 307-309 (1994) 65.
[21] Y. Tsai, B.E. Koel, *J. Phys. Chem. B* 101 (1997) 2895.
[22] W.T. McGrown, C. Kemball, D. Whan, *J. Catal.* 51 (1978) 173.
[23] M. Neurock, R. A. van Santen, *J. Phys. Chem. B* 104 (2000) 11127.
[24] J.P. Botiaux, J. Cosyns, E. Roberts, *Appl. Catal*. 35 (1987) 193.
[25] B.E. Bent, R. G. Nuzzo, B. R. Zegarski, L. H. Dubois, *J. Am. Chem. Soc.* 113(1991) 1143.
[26] T.B. Scoggins, J.M. White, *J. Phys. Chem. B* 101 (1997) 7958.
[27] D. Chrysostomou, A. Chou, F. Zaera, *J. Phys. Chem. B* 105 (2001) 5968.
[28] W. Caminati, G. Grassi, A. Bauder, *Chem. Phys. Lett*. 148 (1988) 13.
[29] G. R. De Maré, Y. N. Panchenko, J. Vander Auwera, *J. Phys. Chem. A,* 101 (1997) 3998.
[30] The 2D Brillouin integrations have been performed on a 5x5x1 grid for the √3x√3 and 2x2 structures, on a 3x5x1 grid for the 3x2 and on a 3x3x1 grid for the 3x3 unit cells.
[31] P. Ganis, I. Orabona, F. Ruffo, A. Vitagliano, *Organometallics* 17 (1998) 2646.
[32] J. Stöhr, F. Sette, A. L. Jonhnsons, *Phys. Rev. Lett*. 53 (1984) 1684.
[33] Q. Ge, D. A. King, *J. Chem. Phys*. 110 (1999) 4699.
[34] F. Delbecq, P. Sautet, *J. Catal.* 211 (2002) 398.
[35] K.W. Wiberg, R.E. Rosenberg, *J. Am. Chem. Soc*. 112 (1990) 1509.
[36] M. Saeys, M. F. Reyniers, G. B. Marin, M. Neurock, *Surf. Sci*. 513 (2002) 315.
[37] A.P. Scott, L. Radom, *J. Phys. Chem. B* 100 (1996) 16502.
[38] G. Rauhut, P. Pulay, *J. Phys. Chem.* 99 (1995) 303.
[39] Note that the coupling of the molecular vibrations and the surface phonons has been neglected
[40] C. Morin, D. Simon, P. Sautet, *J. Phys. Chem B* 107 (2003) 2995.
[41] N.F. Mrozek, M. J. Weaver, *J. Phys. Chem. B* 105 (2001) 8931.
[42] H. Jonsson, G. Mills, K. W. Jacobsen, *Nudged elastic band method for finding minimum energy path of transitions, Classical and Quantum Dynamics in condensed Phase Simulations*, J. B.

Berne, G. Ciccotti, D. F. Coker Eds, World Scientific, Singapore, 1998, 385; G. Henkelman, H. Jonsson, *J. Chem. Phys.* 111 (1999) 7010.
[43] P. Légaré, *Surf. Sci.* 559 (2004) 169.
[44] We calculated the reference energies for a 1/9 ML coverage in the same computational set up (k-points, cut-off …).
[45] P.A. Sheth, M. Neurock, C.M. Smith, *J. Phys. Chem. B* 107 (2003) 2009.

# 4

# Analysis of the reaction intermediates for propylene dehydrogenation on clean and sulphated Pt(111) surfaces

*We have investigated the thermodynamics of the dehydrogenation of propylene to propylidyne on Pt(111) for a 0.25 ML coverage. We have determined the adsorption energies and most favourable adsorption sites for propylene, propylidyne and all the $C_3H_x$ (x=3–7) intermediates (1-propyl, 2-propyl, propylidene, 1-propenyl, 2-propenyl, propenylidene and propynyl). All the surface species are more stable than gas phase propylene. Propylidyne is the most stable one in agreement with experiments. All of the surface moieties adsorb on sites where the number of metal atoms replace the missing hydrogen and preserve a $sp^3$ hybridisation. We used the adsorption energies to compute the overall reaction energies for a number of elementary C–H bond activation and isomerisation reactions that are likely to be involved in the dehydrogenation of propylene. The combination of energy and vibrational frequency calculations allowed us to propose some species as possible intermediates of the decomposition process.*

*We also studied the co-adsorption of propylene and sulphate species and the formation of an alkyl-sulphate intermediate. We proposed a structure for this intermediate and demonstrated the activation of the propylene molecule via its formation.*

*This chapter is organised as follows: section 4.1 is a brief review of the literature published on the adsorption of propylene and its subsequent decomposition to propylidyne on clean and sulphated Pt(111); section 4.2 discusses the adsorption and analyses the simulated vibrational spectra of propylene and the various $C_3H_x$ dehydrogenation intermediates and compares the results obtained with the experimental data available; section 4.3 deals with the co-adsorption of propylene and sulphate and investigates the formation of alkyl-sulphate intermediates; section 4.4 recaptures the main conclusions from foregoing sections.*

## 4.1 Introduction

Fundamental studies of alkene chemistry over catalytically active transition metal surfaces play a key role in efforts to understand and improve diverse catalytic processes ranking from pollution control to fine chemicals synthesis. Consequently, the chemisorption of olefins has extensively been investigated with a view to determining adsorption geometries and the nature and stability of reaction intermediates and products [1]. With this aim several experimental techniques have been developed. Infrared spectroscopy has widely demonstrated its ability to identify atoms and molecules at the metal surface and probe their immediate environment in 'real' reaction conditions. Despite the high performance of this technique, the low concentrations and short lifetimes of reaction intermediates make their identification quite challenging. The determination of vibrational frequencies by *ab initio* computational methods is becoming increasingly important in many areas of the chemistry. Such an area is the identification of reactive intermediates for which the theoretically predicted frequencies can serve as a fingerprint.

The interaction of ethylene ($CH_2$=$CH_2$) with Pt (111) has been extensively used as a model system to understand alkene hydrogenation-dehydrogenation processes. At low temperatures ethylene adsorbs on the Pt(111) surface in a di-σ mode forming a (2x2) pattern. Upon heating above 300 K it transforms into a new more stable species, ethylidyne [2,3,4], also with a (2x2) structure (after exposure to the electron beam of a LEED gun). This molecule is stable roughly between 300 and 420 K. The ethylene-to-ethylidyne transition represents the whole class of reactions, namely, the dehydrogenation of alkenes to alkylidynes. This reaction is believed to be involved in catalytic hydrogenation and dehydrogenation processes. In order to obtain ethylidyne, one H atom has to migrate from one C atom to the other and another one has to be abstracted from the molecule. Then, it is reasonable to assume that the mechanism consists of at least two steps and involves the formation of one or more intermediates. The details of this surface process have been source of an intense debate. Several simple mechanisms have been proposed with intermediates ethyl ($CH_3CH_2^*$), vinyl ($CH_2CH^*$), ethylidene ($CH_3CH^*$) and/or vinylidene ($CH_2C^*$) [5-11].

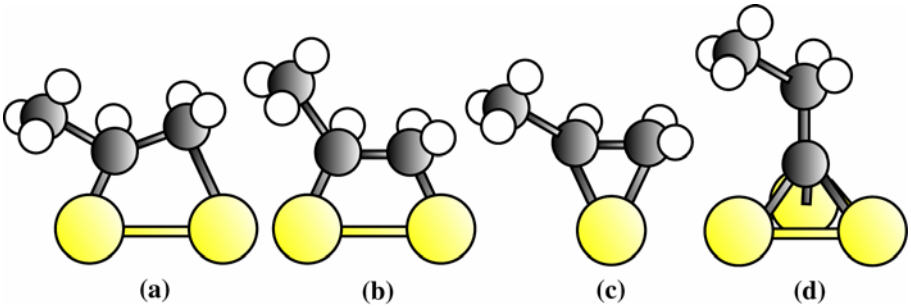


**Scheme 4.1.** Surface structures for the adsorption of propylene on Pt(111): propylene di-σ (V-shape) (a), propylene di-σ (b), propylene π (c), propylidyne (d).

The attempt to extend the preceding conclusions to all olefins has been unsuccessful because much less work has been carried out for bigger alkenes. Higher alkenes are also postulated to decompose via corresponding alkylidyne intermediates. After ethylene, propylene ($CH_3CH=CH_2$) is the most important raw material used in the production of organic chemicals. Early in 1982, Salmerón and Somorjai have shown that propylene adsorbs easily on the Pt(111) surface and remains stable without any chemical decomposition up to around 280 K [12]. Using Thermal Desorption Spectroscopy (TDS) these authors have estimated an adsorption energy of –51 $kJmol^{-1}$ at low coverages. Koestner *et al.* [4], using Low Energy Electron Diffraction (LEED), have proposed that propylene binds to two surface Pt atoms through its unsaturated C=C unit (di-σ-bond) and forms a disordered monolayer. Their results are in agreement with other experimental works [13,14] and with the results issued from qualitative molecular orbital calculations [15]. Besides, Koel and co-workers have also investigated the adsorption and decomposition of propylene on Pt(111) [16]. They have determined an adsorption energy of ~ –70 $kJmol^{-1}$. However, this rather simple picture of the interaction of propylene with Pt(111) contrasts with the complexity that emerges from the complete reflection-absorption (RAIRS) studies of Zaera *et al.* [17]. These authors have proposed that at least four species derive from adsorbed propylene as a function of coverage and the temperature (see **Scheme 4.1**). At T < 230 K this molecule adsorbs undissociated on Pt(111), in an analogous way to ethylene [18]. Below half-saturation, propylene binds to the metal surface in a di-σ fashion preferentially through its central C atom (V-shape). As the coverage increases up to saturation, the molecule rearranges. The C=C bond becomes more horizontal and the methyl group tilts towards a more vertical orientation. Comparison of infrared data from propylene ligands in osmium organometallic complexes to EELS and RAIRS data for propylene on Pt(111) and on Ni (111) [19] corroborates the di-σ-adsorption mode with a large degree of rehybridisation of the C towards $sp^3$ but does not provide further information on the structure of the adsorbed molecule. Above saturation coverage, a second layer of weakly adsorbed molecules grows (π-bonded). They have observed a clear transformation between about 230 and 270 K. Actually, the 275 K RAIRS spectrum is consistent with the formation of an alkylidyne moiety: propylidyne ($CH_3CH_2C^*$). Koestner *et al.* [4] have also detected the formation of this species. They have found that the LEED-

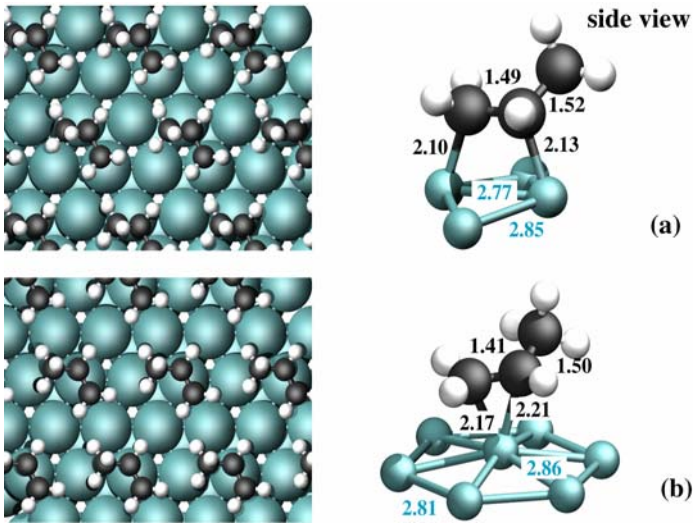


**Figure 4.1.** Stable adsorption modes for propylene on clean Pt(111) surface for a 2x2 unit cell: bridge (a) and top (b).

IV spectra of ethylene and propylene are roughly identical between 280 K and 400 K. This has been interpreted to imply that the room temperature propylene has a structure similar to room temperature ethylene. Data are consistent with the presence of an alkylidyne species. Contrasting with the non-spontaneous ordering of ethylidyne, propylidyne forms spontaneously a 2x2 pattern due to steric considerations. The formation of an intermediate during the transformation from propylene-to-propylidyne seems to be evident according to the new 2890 $cm^{-1}$ feature observed in the 256 and 268 K RAIRS spectra. This signal cannot be associated with propylene nor propylidyne but may be matched with 2-propyl ($CH_3(CH_3)CH^*$) or propylidene ($CH_3CH_2CH^*$) species. Clearly, the accurate description of the structure of propylene and the possible reaction intermediates seems a necessary step towards understanding subsequent surface processes. No unequivocal determination of the mechanism has been accomplished. The best guess is the initial isomerisation of the adsorbed alkene to propylidene (1,2 hydrogen shift) and dehydrogenation to the alkylidyne moiety. Moreover, previous TDS experiments [20] have suggested that the propylene-to-propylidyne conversion may be accompanied by other decomposition reactions since more than one H atom per molecule are desorbed in the TDS spectra.

Especially interesting is the interaction of propylene with poison or promoter species present on the metal surfaces during the hydrogenation-dehydrogenation processes. Sulphoxy species are commonly occurring poisons during hydrocarbon combustion [21]. Exhaustive studies have investigated the influence of surface sulphoxy species in the hydrocarbon oxidation over platinum single-crystal surfaces and practical catalysts [22-26]. Lee *et al.* [25,26] have suggested that pre-adsorbed surface sulphate promotes room temperature propylene combustion associated with the decomposition of a thermally

**Table 4.1.** Computed adsorption energies ($kJmol^{-1}$) and geometries (distances in Å and angles in degrees) for propylene at a 1/4 and 1/9 ML coverage

| **Slab model** | **bridge** | | **top** | |
|---|---|---|---|---|
| Unit cell | **2x2** | **3x3** | **2x2** | **3x3** |
| $E_{ads}$ | –87 | –100 | –51 | –74 |
| distance $C^1$–$C^2$ | 1.49 | 1.49 | 1.41 | 1.41 |
| distance $C^2$–$C^3$ | 1.52 | 1.52 | 1.50 | 1.50 |
| angle $C^2$–$C^1H_2$ | 129 | 131 | 153 | 153 |
| distance $C^1/C^2$–Pt | 2.10/2.13 | 2.11/2.14 | 2.17/2.21 | 2.20/2.22 |

unstable surface alkyl-sulphate complex. This complex decomposes to liberate $CO_2$ and $SO_2$. Nevertheless, the structure and properties of such adsorbed complex remain unknown. As on clean Pt(111), propylidyne is also formed.

Our main goal was to perform a systematic study of the adsorption structures and energetics of the propylene molecule and the possible intermediates of the dehydrogenation reaction. We used periodic DFT calculations to determine the geometry, adsorption site preference and adsorption energy for these species. We carried out a detailed analysis of vibrational spectra and focused our discussion on the comparison with experimental data. Finally, we explored the co-adsorption with sulphate to investigate possible formation of alkyl-sulphate intermediates during the dehydrogenation processes.

## 4.2 Clean Pt(111) surface

### 4.2.1 Adsorption of propylene

We explored several adsorption sites (top, bridge, hollow) for propylene on the clean Pt(111) surface. We found two stable surface structures. **Figure 4.1** shows these adsorption modes: bridge (**Figure 4.1a**) and top (**Figure 4.1b**). In both minima, the molecule binds to the metal surface through its $C^1$–$C^2$ bond, which sits almost parallel to the metal surface. The methyl group and hydrogen atoms are in some extend tilted away from the metal surface. In the bridge adsorption mode the $C^1$–$C^2$ bond axis is aligned along a Pt–Pt bond whereas in the top structure the $C^1$–$C^2$ midpoint is above a Pt surface atom. These surface structures are in good agreement with those predicted from experiments [12,13,14,17]. The bridge structure corresponds to the di-σ adsorption mode and the top to the weakly adsorbed π mode.

We present the computed adsorption energies ($E_{ads}$) for these adsorption modes at 1/4 ML coverage in **Table 4.1**. The bridge (di-σ) surface structure is the most stable one with an adsorption energy of –87 $kJmol^{-1}$. The adsorption on top (π) is relatively close in energy at 36 $kJmol^{-1}$. The computed adsorption energy for the di-σ or bridge mode is higher than the value estimated by TDS experiments (~ –50 $kJmol^{-1}$ and –70 $kJmol^{-1}$ from refs. [12] and [16], respectively). This is not surprising if we take into account the tendency of PW91 to overestimate adsorption energies [27]. Moreover, it is difficult to compare the calculated

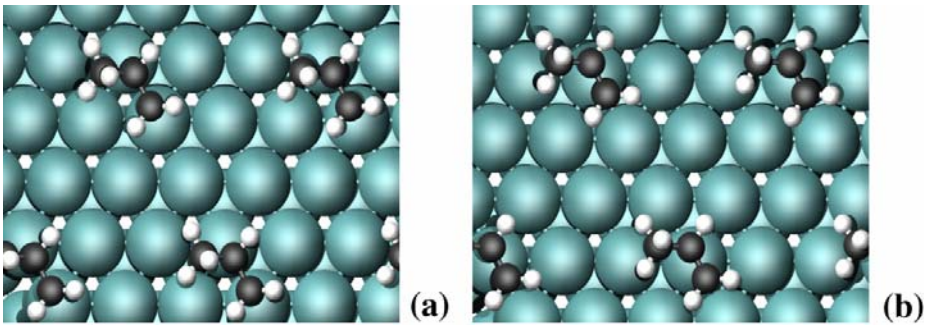


**Figure 4.2.** Stable adsorption modes for propylene on clean Pt(111) surface for a 3x3 unit cell: bridge (a) and top (b).

value with the experimental adsorption energy from TDS curves since propylene decomposition may occur before desorption takes place around 270–280 K [17]. Zaera and co-workers [17] proposed that at low coverages the hydrogen atom released in the dehydrogenation reaction (230–250 K) remains on the surface and weakens the adsorption of propylene. We computed the adsorption energy of the system propylene plus H atom at infinite distance (i.e. we calculated the $E_{ads}$ of the hydrocarbon and the H separately. That is, the two fragments do not interact) and co-adsorbed on the same unit cell. Our calculations predict a decrease in the adsorption energy of 33 kJmol$^{-1}$ on co-adsorption. Actually, the $E_{ads}$ of the system molecule plus H atom at infinite distance is –144 kJmol$^{-1}$ while for the co-adsorbed system is of –111 kJmol$^{-1}$.

We also investigated the coverage effects. We increased the size of the unit cell to 3x3, which corresponds to a molecular coverage of 1/9 ML (see **Table 4.1** and **Figure 4.2**). The adsorption energy increases from –87 kJmol$^{-1}$ (2x2) to –100 kJmol$^{-1}$(3x3) and from –51 kJmol$^{-1}$ (2x2) to –74 kJmol$^{-1}$ (3x3), for the bridge and top structures, respectively. The energy difference (~ 13–23 kJmol$^{-1}$) is indicative of the existence of a slight repulsion between the propylene molecules at a 1/4 ML coverage. Despite the changes in $E_{ads}$, the bridge adsorption mode is still the more stable. Moreover, our results for the bridge adsorption site at a 1/9 ML coverage are in good agreement with the adsorption energy (–90 kJmol$^{-1}$) obtained by Delbecq and Sautet [28] using US-PP.

We summarise the distortion of propylene and the changes in the Pt–Pt bond distances upon adsorption in **Table 4.1** and **Figure 4.1** (side view). Gas phase propylene has a calculated $C^1$–$C^2$ bond distance of 1.33 Å and a $C^2$–$C^1H_2$ angle of 180º [29]. The bond of chemisorbed species to the surface metal atoms usually tends to decrease the internal bond strengths of the molecules, leading to longer internal bond distances. On adsorption, the $C^1$–$C^2$ distance increases significantly. Clearly, we found the most substantial increase for the bridge structure. The $C^1$–$C^2$ bond length is 1.49 Å. Interestingly enough, this bond distance is close to the obtained for di-σ adsorbed ethylene on Pt(111) using similar computational approaches [30,31]. This represents an elongation of 0.16 Å with respect to the free propylene, thus approaching a single C–C bond length as in propane (1.54 Å) with the concomitant reduction of the double bond character. Similar elongation has also been

**Table 4.2.** Computed adsorption energies ($kJmol^{-1}$) and geometries (distances in Å and angles in degrees) for propylene on a $Pt_{33}$ cluster model

| **Cluster model** | **bridge** | | |
|---|---|---|---|
| Basis set[a] | 3-21G/$7Pt_l$-$26Pt_o$ | 6-31G**/$7Pt_l$-$26Pt_o$ | 6-31G**/$33Pt_l$ |
| $E_{ads}$ | –49(9) | –23(8) | –61(–26) |
| distance $C^1$–$C^2$ | 1.49 | 1.50 | 1.50 |
| distance $C^2$–$C^3$ | 1.53 | 1.52 | 1.52 |
| angle $C^2$–$C^1H_2$ | 130 | 129 | 129 |
| height $C^1/C^2$ | 2.11/2.16 | 2.07/2.12 | 2.07/2.12 |

[a]Basis set for adsorbate/substrate units. Results in parenthesis stand for the values corrected for the BSSE.

reported for different alkene molecules upon adsorption on Pt(111) [32,33]. For the top mode, the $C^1$–$C^2$ distance is 1.41 Å, which indicates that the $sp^2$ to $sp^3$ hybridisation is smaller. Another indicator of the degree of re-hybridisation of the C atoms is the $C^2$–$C^1H_2$ angle. Propylene loses its 'planarity' on adsorption as the CH bonds bend away from the surface plane. The angle between the H–$C^1$–H plane and the $C^1$–$C^2$ bond (parallel to the surface) for the bridge configuration (~ 130º) is larger than the angle for the top configuration (~ 153º). This fact confirms that the C atoms in the bridge structure have a higher degree of rehybridisation to $sp^3$.

For both minima, all the CH bond distances are 1.10 ± 0.01 Å. The rotation of the methyl group is almost free well in line with the results of propyne on different (111) metal surfaces (see **Chapter 3**).

As expected, the changes on the substrate are rather small. The relaxation of the surface metal atoms mainly involves an outwards movement of the Pt atoms directly bonded to the C ones. This produces a small corrugation of the surface (< 4%) with the simultaneous change of the Pt–Pt bond distances (< 0.16 Å).

We do not observe significant changes in the adsorption geometry when the coverage decreases (see **Table 4.1**).

Next we turn our attention to the description of the interaction of propylene on Pt(111) arising from the cluster model approach. We carried out these calculations using the Gaussian98 program [34] and the well-known hybrid B3LYP functional [35]. We represented the Pt(111) surface by a $Pt_{33}$(14,12,7) cluster model (the numbers in parenthesis indicate the number of atoms in each atomic layer ) having $Pt_7$(4,3) as the *local* region and the remaining atoms defining the *outer* region [36]. The platinum atoms in the *local* region have been treated with the Hay-Wadt relativistic effective core potential [37] (RECP) which explicitly includes the $5s^25p^6$ semi-core electrons and the $5d^96s^1$ valence electrons and a (8s6p3d/3s3p2d) basis set. The remaining platinum atoms in the cluster have been treated with a one-electron RECP and a double-zeta basis set [38]. Let us recall that here the use of a cluster model is mainly aimed to investigate the limitations of the cluster model for the description of the propylene chemisorption. We corrected the adsorption energies for the Basis Set Superposition Error (BSSE), inherent to localised basis sets, using the standard Boys-Bernardi counterpoise method [39].

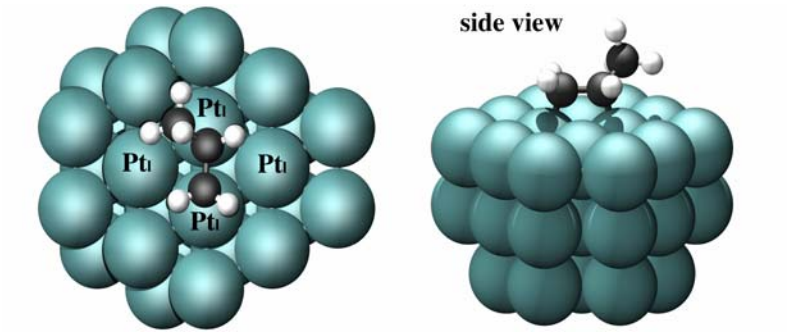


**Figure 4.3.** Adsorbed propylene on a $Pt_{33}$ cluster model. $Pt_l$ accounts for the Pt atoms in the *local* region.

We took the optimised geometry found in the slab calculations as starting point and re-optimised, maintaining the substrate frozen at the bulk geometry. Hence, the Pt-Pt distances were kept at the experimental bulk value of 2.77 Å [40]. In a preliminary set of calculations, we employed the 3-21G basis set for propylene. The calculated adsorption energy is –49 $kJmol^{-1}$. However, this value drops to 9 $kJmol^{-1}$ once corrected for the BSSE (**Table 4.2**). To further improve the quality of this calculation, we re-optimised the structure with the more extended 6-31G** basis set for propylene. The adsorption energy decreases to –23 $kJmol^{-1}$ but the BSSE corrected value of 8 $kJmol^{-1}$ is still quite similar to the previous value. Finally, we improved the cluster model by treating all Pt atoms at the same level, i.e. explicitly including 18 electrons per Pt atom and the LANL2 basis set, using the geometry of the preceding point. The final BSSE corrected adsorption energy is –26 $kJmol^{-1}$. In all the cases, the adsorption geometry (**Figure 4.3** and **Table 4.2**) is in good agreement with the one obtained with the slab approach. Notice that the differences in C–C and C–Pt bond distances are rather small (<0.04 Å).

From this set of calculations, two important conclusions emerge. The most accurate cluster result for the adsorption energy is only ~ 30% of the one obtained in slab calculations. There are two reasons for this difference. First, a smaller value of the adsorption energy in the cluster model approach is not surprising; it arises from a too large Pauli repulsion between the cluster and the adsorbate. The overestimation of the Pauli repulsion comes from artificially confining the metal electron density in a reduced region, which reduces electron delocalisation. Second, the surface relaxation is not taken into account in the cluster calculations. Indeed, if one compares the cluster adsorption energy (–26 $kJmol^{-1}$) with the non-relaxed slab result (–39 $kJmol^{-1}$) the difference is reduced significantly.

Moreover, it is necessary a good description of the metal atoms (high quality basis set) with the concomitant increase of the computational cost.

Despite its good results for adsorption geometries, the poor description of adsorption energies and, more important, its high computational cost make cluster models not suitable to perform the study of the thermochemistry.

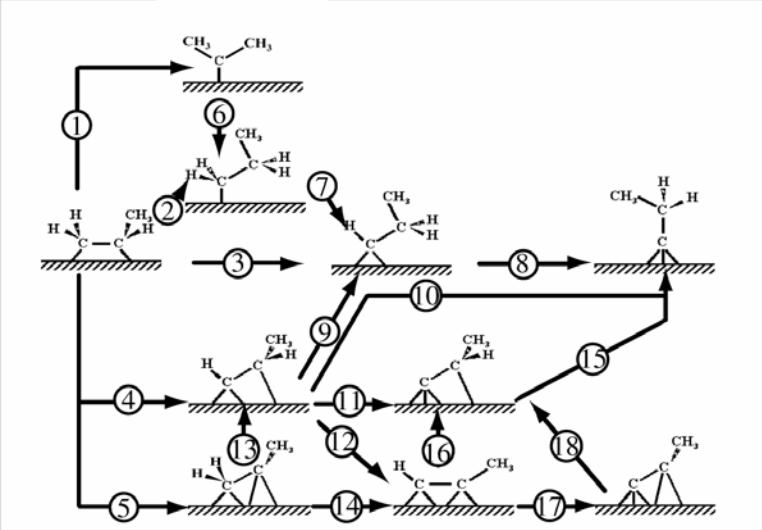

**Scheme 4.2**. Elementary paths for the decomposition of propylene to propylidyne on Pt(111).

### 4.2.2 Adsorption of $C_3H_x$ (x=3–7) species

**Scheme 4.2** shows the elementary paths for the dehydrogenation of di-σ bonded propylene to propylidyne. We did not consider the C–C bond breaking and we neglected the dehydrogenation of the methyl group. We determined the adsorption modes and the corresponding adsorption energies for all $C_3H_x$ (x= 3–7) species using a 2x2 unit cell. The possible reaction intermediates are: 1-propyl ($CH_3CH_2CH_2^*$), 2-propyl ($CH_3(CH_3)CH^*$), propylidene ($CH_3CH_2CH^*$), propylidyne ($CH_3CH_2C^*$), 1-propenyl ($CH_3CH{=}CH^*$), 2-propenyl ($CH_3C^*{=}CH_2$), propyne ($CH_3C{\equiv}CH$), propenylidene ($CH_3CH{=}C^*$) and propynyl ($CH_3C{\equiv}C^*$). As for propylene, we explored different adsorption sites. Here, we show only the most stable identified configuration for each intermediate. The relative stabilities for each of the surface species are shown in **Figure 4.4**. We computed them with the formula

$$E_{ads} = (E_{C_3H_x/surface} - E_{surface} - E_{C_3H_{6(g)}}) - (x-6)(E_{H/surface} - E_{surface}) \qquad (4.1)$$

**Equation (4.1)** allowed us to obtain adsorption energies of the surface intermediates comparable with the adsorption energy of propylene. All the surface intermediates are more stable than the gas phase propylene. However, only four moieties are more stable than adsorbed propylene (1-propenyl, propylidyne, propenylidene and propyne, see **Figure 4.4**). Among them, the most stable one is the propylidyne species. Indeed, this species is –59 $kJmol^{-1}$ more stable than adsorbed propylene. In agreement with the experimental evidence [4,17,20], our calculations confirm that it is thermodynamically favourable for propylene to

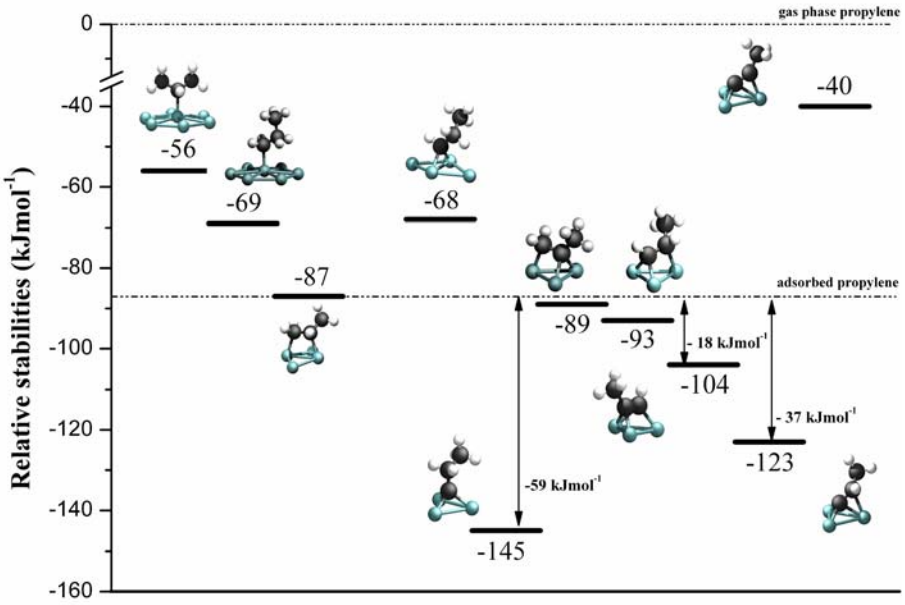


**Figure 4.4** Energy profile for all the $C_3H_x$ (x= 3–7) fragments on Pt(111) at1/4 ML coverage.

dehydrogenate to form propylidyne and surface hydrogen. 2-propenyl is almost isoenergetic with propylene (the energy difference is only 2 $kJmol^{-1}$). 1-propyl, 2-propyl, propylidene and propynyl are less stable by 18, 31, 19 and 47 $kJmol^{-1}$, respectively.

The calculated optimised structural parameters are illustrated in **Figures 4.5a-h**. For sake of clarity, we only represented the Pt atoms directly below the hydrocarbon fragment. Here, we do not present the adsorption geometry of propyne on Pt(111) because we have discussed it in the previous chapter ( **§ 3, section 3.3.1**). 1-propyl (**Figure 4.5a**) and 2-propyl (**Figure 4.5b**) prefer the top adsorption site where the surface metal atom essentially replaces the missing hydrogen atom in order to form a 'propane-like' surface intermediate which preserves its $sp^3$ symmetry. This is consistent with concepts derived from Hoffmann [41] and Schustorovich and Baetzold [42] orbital interaction scheme. The balance between the Pauli repulsion and the orbital overlap dictates the adsorption site preference. For metals that lie to the right in the periodic table, Pauli repulsion dominates [43] and favours the top adsorption site for alkyl groups. Neurock and van Santen [44] have yet utilised these arguments to explain the adsorption site preference of ethyl groups on Pd(111). Propylidene (**Figure 4.5c**) is missing two hydrogen atoms in $C^1$ and therefore favours adsorption at a bridge site or $\eta^2$ ($C^1$)-adsorption mode (here, $\eta^2$ denotes the number of Pt atoms bind to a C atom). The $C_3H_5$ intermediates adsorb preferentially on hollow fcc sites. Propylidyne (**Figure 4.5d**) is missing three hydrogen atoms in $C^1$ and prefers to bind to three Pt atoms ($\eta^3$ ($C^1$) fashion). Our results are in good agreement with the experimental results of

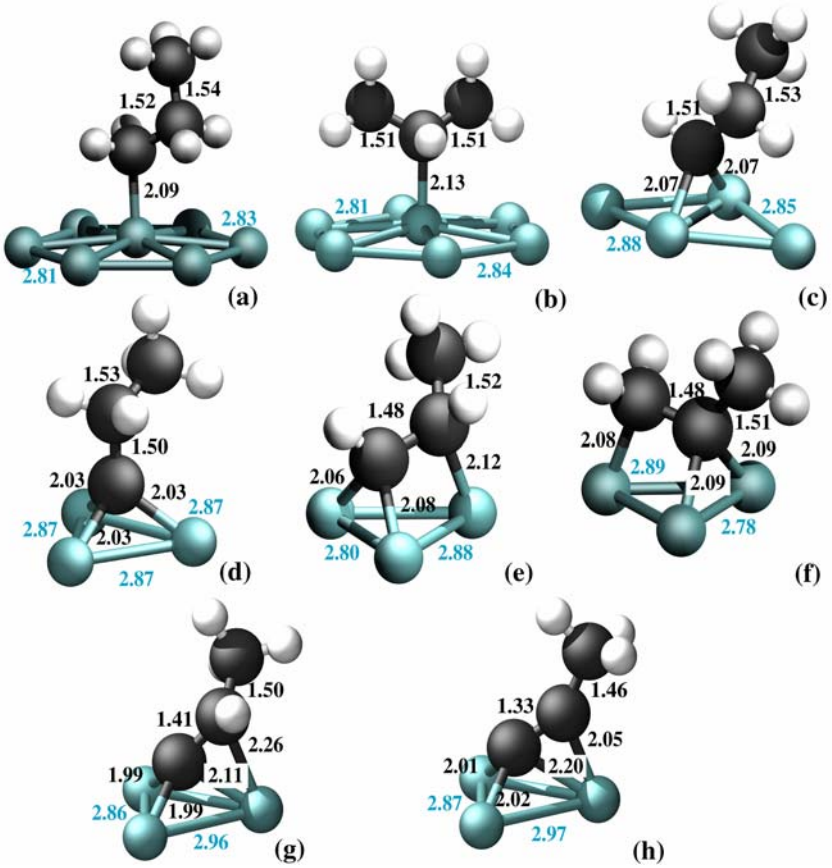


**Figure 4.5.** Adsorption geometries for the $C_3H_x$ (x= 3-7) fragments on Pt(111) at 1/4 ML coverage. (a) 1-propyl, (b) 2-propyl, (c) propylidene, (d) propylidyne, (e) 1-propenyl, (f) 2-propenyl, (g) propenylidene and (h) propynyl. Distances in Å. Only the atoms directly below the hydrocarbon moiety are shown here for sake of visual clarity.

Koestner *et al.* [4]. These authors have determined that the propylidyne species is most likely adsorbed in the fcc hollow site on Pt(111). The 1-propenyl moiety (**Figure 4.5e**) is missing two H atoms in $C^1$ and one in $C^2$ and, therefore, it prefers the $\eta^2\eta^1(C^1,C^2)$-adsorption mode. The adsorption geometry of 2-propenyl (**Figure 4.5f**) is equivalent to the one obtained for 1-propenyl. There appears to be a general trend that Pt(111) prefers $sp^3$ bound intermediates. Actually, all the C–C bond distances are within the range 1.48-1.54 Å.

The picture for propenylidene (**Figure 4.5g**) and propynyl (**Figure 4.5h**) is quite different. Similarly to the $C_3H_5$ species, both surface intermediates adsorb preferentially on a 3-fold hollow site (fcc). The propenylidene moiety is missing three H atoms from $C^1$ and

**Table 4.3.** Calculated surface reaction energies ($E_{reac}$, $kJmol^{-1}$) for the decomposition of propylene on Pt(111)

| step | Surface reaction | reaction | $E_{reac}$ |
|---|---|---|---|
| 1 | propylene +H → 2-propyl | hydrogenation | 31 |
| 2 | propylene +H → 1-propyl | hydrogenation | 18 |
| 3 | propylene → propylidene | isomerisation | 18 |
| 4 | propylene → 1-propenyl +H | dehydrogenation | –6 |
| 5 | propylene → 2-propenyl +H | dehydrogenation | –2 |
| 6 | 2-propyl → 1-propyl | isomerisation | –13 |
| 7 | 1-propyl → propylidene +H | dehydrogenation | 1 |
| 8 | propylidene → propylidyne +H | dehydrogenation | –77 |
| 9 | 1-propenyl +H → propylidene | hydrogenation | 25 |
| 10 | 1-propenyl → propylidyne | isomerisation | –52 |
| 11 | 1-propenyl → propenylidene +H | dehydrogenation | –30 |
| 12 | 1-propenyl → propyne +H | dehydrogenation | –11 |
| 13 | 2-propenyl → 1-propenyl | isomerisation | –4 |
| 14 | 2-propenyl → propyne +H | dehydrogenation | –16 |
| 15 | propenylidene +H → propylidyne | hydrogenation | –22 |
| 16 | propyne → propenylidene | isomerisation | –19 |
| 17 | propyne → propynyl +H | dehydrogenation | 64 |
| 18 | propynyl +H → propenylidene | hydrogenation | –83 |

one from $C^2$ and, therefore, it prefers to sit on $\eta^3\eta^1$ ($C^1$,$C^2$) fashion. However, the $C^1$–$C^2$ bond distance (1.41 Å) is rather short compared to the $C_3H_x$ (x=5–7) hydrocarbon fragments (see above). Dumesic and co-workers have obtained the same adsorption site and geometry for vinylidene ($CH_2$=$C^*$) on Pt(111) [45]. However, propynyl binds clearly in a $sp^2$ fashion. This molecule is missing three H atoms from $C^1$ and two from $C^2$ to form a surface intermediate of $sp^3$ symmetry. However, it binds to the Pt(111) surface in a $\eta^3\eta^1$ ($C^1$,$C^2$) adsorption mode. $C^2$ only forms a bond with a metal atom. Moreover, the $C^1$–$C^2$ distance (1.31 Å) is obviously closer to a double bond (1.33 Å, propylene) than to a simple one (1.54 Å, propane).

**Table 4.3** summarises the reaction energies for the various elementary steps depicted in **Scheme 4.2**. We computed the reaction energy ($E_{reac}$) by subtracting the energies of initial from the final state. For example, we calculated the energy for the propylene dehydrogenation to propylidyne by subtracting the energy of the adsorbed propylidene from the energy of the system propylidyne plus H adsorbed. In all the hydrogenation/dehydrogenation reactions, we assumed that the hydrocarbon moiety and the H atom do not interact.

Most of the steps listed in **Table 4.3** are either slightly endothermic or exothermic and would therefore still be possible in the mechanism of propylene decomposition. The formation of the propylidyne intermediate is always exothermic. This reaction can take place via dehydrogenation (8), isomerisation (10) or hydrogenation (15). The most favourable way to obtain this species is from propylidene (–77 $kJmol^{-1}$). Moreover, the surface reaction energetics suggests that the formation of propynyl is unlikely at this

**Table 4.4.** Calculated frequencies (in $cm^{-1}$) and intensities ($kmmol^{-1}$) for propylene on Pt(111)

| experimental assignment | RAIRS[a] $\nu_i$ | 2x2[b] $\omega_i$ | $I_i$ | 3x3[b] $\omega_i$ | $I_i$ | theoretical assignment |
|---|---|---|---|---|---|---|
| $CH_2$ as st | 2915(s) | 3013 | 2.2 | 3053/3009 | 0.2/1.6 | $CH_3$ as st |
| CH st | 2883(s) | 2986 | 0.1 | 2995 | 1.0 | CH st |
| $CH_3$ s st+2x$CH_3$ as df | 2860(m) | 2933 | 9.9 | 2933 | 8.7 | $CH_3$ s st |
| $CH_2$ s st | 2830(w) | 2982 | 2.0 | 2987 | 1.3 | $CH_2$ s st |
| - | - | 1434/1421 | 0.4/0.2 | 1434/1423 | 2.4/0.1 | $CH_3$ as df |
| $CH_2$ sci | 1437(m) | 1400 | 0.1 | 1401 | 0.4 | $CH_2$ sci |
| $CH_3$ s df | 1375(w) | 1337 | 0.1 | 1347 | 0.2 | $CH_3$ s df |
| CH b | 1309(w) | 1296 | 0.3 | 1301 | 1.0 | CH b |
| $CH_2$ wag | 1260(w) | 1161 | 0.2 | 1158 | 0.3 | $CH_2$ twi |
| $C^2$–$C^3$ st | 1088(s) | 1092 | 0.9 | 1092 | 0.8 | $C^1$–$C^2$ st/ $C^2$–$C^3$ st |
| $CH_2$ twi | 1037(s) | 1030 | 1.4 | 1033 | 1.9 | $CH_2$ wag |
| $CH_3$ ro | 1015(s) | 1007 | 2.9 | 1008 | 7.5 | $CH_3$ ro |

key: as, asymmetric; s, symmetric; st, stretching; df, deformation; sci, scissoring; twi, twisting; wag, wagging; ro, rocking; b, bending; s, strong; m, medium; w, weak.
[a]values from ref 17; [b] this work.

coverage. The formation of this species by dehydrogenation of propyne is 64 uphill by $kJmol^{-1}$. Besides, its hydrogenation to propenylidene is highly exothermic (–84 $kJmol^{-1}$). Therefore, we suspect that propynyl is unlikely to be involved in the direct decomposition of propylene to propylidyne.

### 4.2.3 Analysis of vibrational spectra

To shed light on the nature of the surface intermediate of the propylene dehydrogenation to propylidyne, we computed the RAIRS spectrum for propylene (**Table 4.4**), propylidyne (**Table 4.5**) and all the possible reaction intermediates (1-propyl, 2-propyl, propylidene, 1-propenyl, 2-propenyl, propenylidene and propynyl, see **Appendix A.3**) on Pt(111) at 1/4 ML coverage. We analysed the spectrum of propyne on Pt(111) in **Chapter 3** (**section 3.3.3**).

**Table 4.4** shows the frequencies along with the intensities for the di-σ propylene on Pt(111). We also computed the spectrum at 1/9 ML coverage (3x3 unit cell). The differences between these two models are not significant. Only the intensity of the bands at ~ 1430 and ~ 1000 $cm^{-1}$ increases as the coverage decreases. We found that almost all the normal modes are coupled. This makes the description of the vibrations somewhat arduous and, in some cases, the assignment may be ambiguous. Our objective is not to analyse in detail the normal modes but to establish the differences among the surface species spectra that can help us to identify the possible reaction intermediates. Thus, the theoretical assignment accounts for the main vibrations for each feature. The experimental spectrum [17] presents four bands in the C–H stretching region (two of them quite intense); four medium or weak peaks in the 1500–1200 $cm^{-1}$ range and three intense features in the 1000–1100 $cm^{-1}$ region. Despite some differences in intensities and band assignment, our results

**Table 4.5.** Calculated frequencies (in $cm^{-1}$) and intensities ($kmmol^{-1}$) for propylidyne on Pt(111)

| experimental assignment | RAIRS[a] $\nu_i$ | EELS[b] $\nu_i$ | RAIRS[c] $\nu_i$ | 2x2[d] $\omega_i$ | $I_i$ | theoretical assignment |
|---|---|---|---|---|---|---|
| $CH_3$ as st | 2960(s) | 2980(m) | 2961(vs) | 3044 | 5.2 | $CH_3$ as st |
| $CH_3$ s st | 2917(s) | 2920(m) | 2921(w)/2865(mw) | 2970 | 4.4 | $CH_3$ s st |
| 2x$CH_3$ as df | 2860(m) | - | - | - | - | - |
| $CH_3$ as df | 1450(m) | 1465(s) | 1450(s) | 1454 | 1.0 | $CH_3$ as df |
| $CH_2$ sci | 1408(m) | - | 1407(m) | 1399 | 0.4 | $CH_2$ sci |
| $CH_3$ s df | 1374(w) | - | - | 1349 | 0.0 | $CH_3$ s df |
| $CH_2$ wag | - | 1295(w) | 1303(w) | 1265 | 0.1 | $CH_2$ wag |
| C–C st | 1104(m) | 1115(s) | 1103(s) | 1087 | 4.1 | $C^1$–$C^2$ st |
| $CH_3$ ro | 1079(w) | 1055(s) | 1055(w) | 1033 | 0.2 | $CH_3$ ro |
| $CH_3$ ro | 1041(m) | - | 1039(s) | 1026 | 0.0 | $CH_3$ twi |
| C–C st | - | 920(s) | 929(s) | 921 | 1.4 | $C^2$–$C^3$ st |

key: as, asymmetric; s, symmetric; st, stretching; df, deformation; sci, scissoring; twi, twisting; wag, wagging; ro, rocking; b, bending; s, strong; m, medium; w, weak.
[a]from ref 17; [b] from ref 13; [c]from ref 47; [d]this work.

are quite consistent with the experimental observations. The differences in the 2800–3100 $cm^{-1}$ region arise from the poor description of the CH stretching modes [46]. Besides, both the experimental coverage and the experimental periodicity are not well reproduced. The arrangement of the molecules on the surface changes the orientation of the methyl groups and its environment. Zaera and co-workers [17] have pointed out that these changes strongly influence the band intensities.

**Table 4.5** presents the calculated frequencies and intensities for propylidyne on Pt(111). For sake of comparison, **Table 4.5** also summarises the corresponding features in the RAIR [17,47] and EEL spectra [13] of propylene at ~ 300 K and saturation coverage. By analogy with the ethylene case, these studies have determined that these spectra arise from the propylidyne species. Our results fully confirm the experimental assignment (see **Table 4.5**). The agreement between the experimental and simulated spectra is fairly good. The main difference appears in the region around 900–1100 $cm^{-1}$. We assign the features at 1033, 1026 and 921 $cm^{-1}$ to the $CH_3$ ro, $CH_3$ twi and the $C^2$–$C^3$ st, respectively. Only the peaks at 1033 and 920 $cm^{-1}$ are intense. In the experimental RAIR spectrum, three intense peaks appear in this region. The bands at 1079[17]/1055[47], 1041[17]/1039[47] and 920 [47] $cm^{-1}$ have been assigned to the $CH_3$ ro, $CH_3$ ro and C–C st, respectively. These differences may arise from the orientation of the neighbouring methyl groups. In our calculation all the methyl groups are oriented in the same direction. However, Koestner *et al*. [4] have suggested that the methyl groups tend to minimise the steric repulsions and, therefore, there are some orientations sterically not possible. Obviously, the one reproduced with the 2x2 unit cell is not the most favoured one.

The spectroscopic information available for the possible intermediates of the propylene-to-propylidyne transformation is scarce. Zaera *et al.* [17] have investigated the changes in the RAIR spectrum of propylene on Pt(111) as a function of the temperature

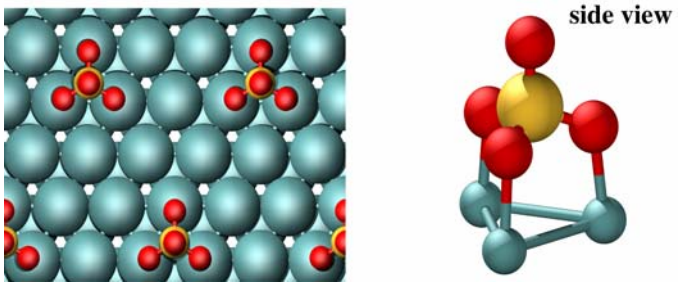


**Figure 4.6.** Sulphate on Pt(111) for a 3x3 unit cell.

(230–300 K). The formation of an intermediate seems to be evident. They have found that the spectrum at ~ 260 K includes a new signal at 2890 $cm^{-1}$. Moreover, this spectrum has no new peaks in deformation IR region. Actually, in the 1000–1500 $cm^{-1}$ range, all the bands can be assigned to either propylene or propylidyne. They have proposed that these features may belong to the 2-propyl or to the propylidene species. We simulated and analysed the RAIRS spectra for all the proposed surface intermediates (see **Appendix A.3**). Unfortunately, the CH stretching region (2800–3100 $cm^{-1}$) is not well described with the harmonic model. Moreover, all the features lie in a small range and the differences are not big enough to be conclusive. We focused our attention in the deformation region (more specifically, on the features that can help us to rule out some species). The 1-propyl species has two signals at 1125 and 1350 $cm^{-1}$ that are not visible either in the propylene spectrum or in the one of propylidyne. The features can be assigned to the $CH_3$ s df and to the $CH_2$ wag, respectively. 2-propyl has a quite strong feature at 1162 $cm^{-1}$ (CH b mixed with the $CH_3$ ro). The propyne molecule, the 2-propenyl and the propenylidene moieties have some important peaks around 1350 $cm^{-1}$ that are associated to the $CH_3$ s df. The propynyl intermediate has a strong feature at 1599 $cm^{-1}$, which can be assigned to the C=C st. However, the spectrum may be matched with those from propylidene or from 1-propenyl because these species have no important signals in the 1100–1400 $cm^{-1}$ region. Unluckily, it is not possible to unequivocally identify the intermediate.

## 4.3 Sulphated Pt(111) surface

We investigated the formation of an alkyl-sulphate complex on co-adsorption of propylene and $SO_4$ on Pt(111) using a 3x3 unit cell (1/9 ML coverage). In the first place, we considered the adsorption of $SO_4$ on Pt(111). After a systematic exploration of the different adsorption modes (top, bridge, hollow), we conclude that $SO_4$ adsorbs on a three-fold hollow site, with a $C_{3v}$ local symmetry. The three equivalent oxygen atoms are directly bound to three neighbouring Pt atoms while the fourth oxygen points upward (see **Figure 4.6**). All the Pt–O bond lengths are 2.11 Å; the internal S–O distances are 1.54 Å and 1.43 Å for the three equivalent oxygen atoms and the apical oxygen atom, respectively. The O–

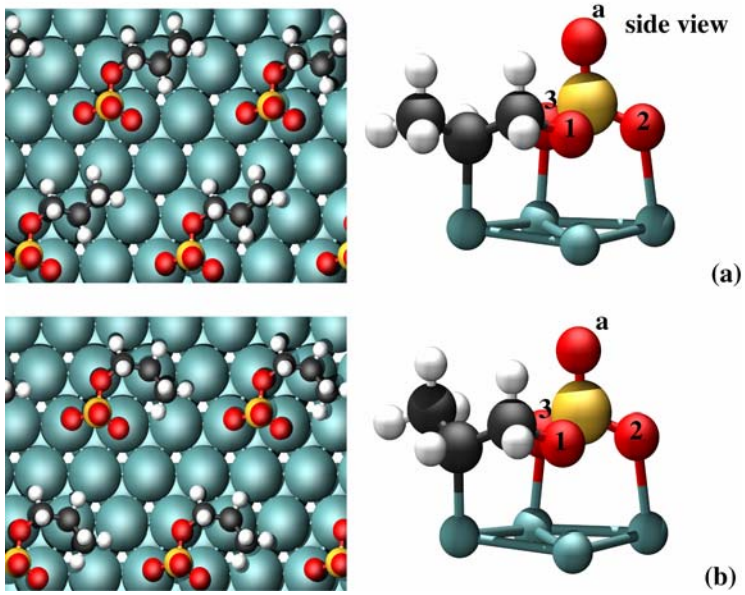


**Figure 4.7.** Alkyl-sulphate complex adsorbed on Pt(111) for a 3x3 unit cell: *trans* (a) and *cis* (b).

S–O angle involving two oxygen atoms directly bonded to the metal surface is 108º while the one related to the non-surface oxygen atom is 110º. The present results fully agree with those recently reported by Lin et al. [48] in their systematic theoretical study of sulphur oxides on Pt(111). Lee et al. [24,25] obtained surface sulphate adsorbing $SO_2$ onto oxygen pre-saturated Pt(111). Thus, we calculated the adsorption energy for $SO_4$ on Pt (111) with respect to the 2O/Pt(111) system (two adsorbed oxygen atoms per Pt unit cell) and the $SO_2$ molecule in gas phase. Following this procedure we obtained an adsorption energy of –127 $kJmol^{-1}$. If the reference is $SO_2 + O_2$ in the gas phase, the adsorption energy is –352 $kJmol^{-1}$, which is close to the value of –342 $kJmol^{-1}$ reported by Lin et al. [48] at the same coverage.

On co-adsorption with the propylene molecule a new alkyl-sulphate species may form. We found two different 'conformations' for this intermediate (see **Figure 4.7**). For sake of simplicity we named these structures *cis* (the methyl group and the sulphate lie in the same side of the $C^1$–$C^2$ bond) and *trans* (the $SO_4$ and the methyl group are in the opposite side of the $C^1$–$C^2$ bond). The energy difference between these two adsorption modes is quite small. Indeed, the *trans* surface structure is only 11 $kJmol^{-1}$ more stable than the *cis* adsorption mode. Experimentally propylene is adsorbed on sulphate pre-covered Pt(111) surface [25,26]. The energy gain due to the formation of this complex with respect to the sulphated surface and the free propylene is -70 $kJmol^{-1}$. Besides, the alkyl-sulphate complex and the co-adsorbed system (propylene and $SO_4$ adsorbed in the same unit cell) have the same relative stability. These results indicate that the formation of such a complex is quite

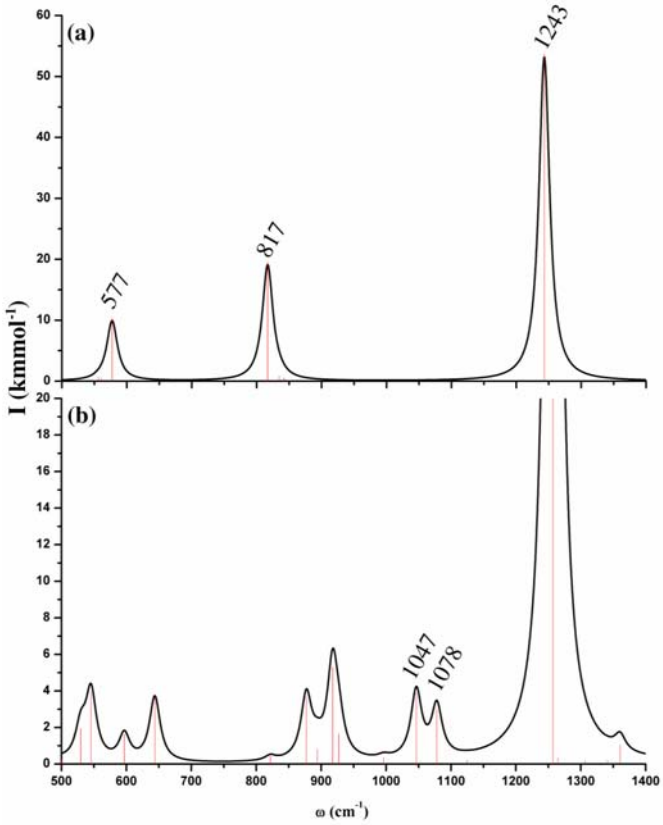


**Figure 4.8.** Simulated IR spectra for sulphate (a) and the alkyl-sulphate complex on Pt(111) for a 3x3 unit cell.

favourable on the Pt(111) surface.

The formation of the alkyl-sulphate complex changes significantly the surface geometry of both sulphate and propylene (see **Figure 4.7**). The $SO_4$ molecule binds to the $C^1$ of the hydrocarbon through one of its 'surface' oxygen atoms $O^1$. Hence, the additional C–O bond (1.47 Å) created may be the 'fingerprint' of this new species. As a consequence of the interaction, the sulphate moiety loses its $C_{3v}$ symmetry. In the new structure only two oxygen atoms ($O^2$ and $O^3$) remain bound to the surface (see **Figure 4.7, side view**). Note that the oxygen atom that directly interacts with the propylene fragment ($O^1$) moves up to 2.51 Å. Moreover, we observe an important elongation of the two remaining Pt–O distances. On the $SO_4$/Pt(111) system, the Pt–$O^2$ and Pt–$O^3$ are equivalent. On co-adsorption, they increase to 2.31 Å (Pt–$O^2$) and 2.21 Å (Pt–$O^3$). The different Pt–O bond distances results from a small rotation of the sulphate fragment (~5º). Only the S-$O^1$

changes significantly (1.65 Å). The internal O-S-O angles vary as well: 112º ($O_2$–S–$O_3$), 105º ($O^1$–S–$O^3$) and 101º ($O^1$–S–$O^2$). The angles related to the apical oxygen atom are now 115º ($O^2$–S–$O^a$), 112º($O^3$–S–$O^a$) and 108º ($O^1$–S–$O^a$).

The changes in geometry of the propylene molecule are more important than those observed for the sulphate species. The molecule is now adsorbed in a V-shape through its central $C^2$ atom. The $C^1$–$C^2$ bond length is 1.53 Å. This value is far away from those of gas-phase propylene (1.33 Å) and propylene on Pt (1.49 Å). Moreover, the H–$C^1$–H angle (109º). Clearly, the formation of this new species activates the propylene molecule.

**Figure 4.8a-c** illustrates the calculated vibrational spectra for the sulphate molecule (**Figure 4.8a**), and the alkyl-sulphate complex (**Figure 4.8b**) on Pt(111). Three peaks at 1243, 817 and 577 $cm^{-1}$ dominate the spectrum of the $SO_4$ molecule. Our results are in good agreement with the experimental HREELS spectrum of $SO_2$ on oxygen-precovered Pt(111) [49] and previous DFT calculations of $SO_4$ on Pt(111) [48]. We assign the peak at 1243 $cm^{-1}$ to the S-$O^a$ stretching. The feature at 817 $cm^{-1}$ corresponds to the $SO_3$ symmetric stretching of the three equivalent oxygen atoms vibrating in phase. Finally, we assign the band at 577 $cm^{-1}$ to the $SO_3$ symmetric deformation of the oxygen atoms directly interacting with the metal surface. All these features also appear in the spectrum of the alkyl-sulphate complex (**Figure 4.8b**). We do not observed significant changes in the peak at 1243 $cm^{-1}$, well in line with the absence of major geometrical changes in the S-$O^{(a)}$ bond upon formation of the complex. However, the 817 and 577 $cm^{-1}$ signals split because the three O atoms are not equivalent any more. Several weak features appear around 900 and 600 $cm^{-1}$. These bands correspond to the $SO_3$ stretch and the $SO_3$ deformation modes mixed with different modes of the hydrocarbon molecule. The two features at 1078 and 1047 $cm^{-1}$ have some contribution of the new C–O bond formed (especially the 1047 $cm^{-1}$ feature). Actually, these peaks are the 'fingerprint' of the alkyl-sulphate complex, since they appear in a region where there is no signal in the $SO_4$/Pt(111) spectrum and the peaks in the adsorbed propylene spectrum are very weak (see **section 4.2.3**). Values between 1000 and 1200 $cm^{-1}$ are common in species where the oxygen atom is single-bonded to a sulphur atom. We computed the vibrational frequencies for dimethylsulphate in gas phase using the Gaussian98 code [34]. Indeed, for this molecule the C–O stretching appears at 1023 $cm^{-1}$.

## 4.4 Conclusions

We investigated the adsorption of propylene on Pt(111) by DFT. We found two stable surface structures: bridge (di-σ) and top (π). Our calculations indicate that the di-σ-bounded propylene is more stable than the π species. Actually, the computed adsorption energy for the di-σ-adsorption mode is –87 $kJmol^{-1}$ while that for the π mode is –51 $kJmol^{-1}$. The study of the coverage effects showed that the adsorption energy increases with decreasing the coverage (1/4 → 1/9 ML), but that the energy difference between the bridge and top structures remains roughly the same, with the former still more stable.

Moreover, we examined the adsorption modes and energies for 1-propyl, 2-propyl, propylidene, propylidyne, 1-propenyl, 2-propenyl, propenylidene and propynyl at a surface coverage of 0.25 ML corresponding to a 2x2 unit cell. We determined the relative stabilities

and the most favourable adsorption sites for all the above species. For the $C_3H_x$ (x=3–7) fragments, there appears to be a general trend that Pt(111) prefers $sp^3$ bound intermediates. The relative stabilities of 1-propyl, 2-propyl, propylidene, propylidyne, 1-propenyl, 2-propenyl, propyne, propenylidene and propynyl are –69, –56, –68, –145, –93, –89, –104, –123 and –40 $kJmol^{-1}$, respectively. Propylidyne is the most stable surface species on Pt(111) well in line with the experimental evidence.

We computed the reaction energies for 18 elementary steps that may potentially be involved in the propylene-to-propylidyne transformation. Our calculations clearly indicate that the dehydrogenation of propylene to propylidyne is thermodynamically favourable. Besides, the formation of propynyl is energetically unfavourable and we concluded that is species may not be involved in the direct reaction of dehydrogenation.

Moreover, we simulated the vibrational spectra for propylene, propylidyne and the possible reaction intermediates. Our results for propylene and proplidyne are quite consistent with the experimental data. Unfortunately, the experimental data available for the reaction intermediate is not enough for an unequivocal identification. Our best guesses are: propylidene and 1-propenyl.

We also studied the surface structure and stability of a propylene-sulphate complex. We showed that the formation of this intermediate is energetically favoured and provided a theoretical support to the experimental observations. We proposed the surface structure for this alkyl-sulphate complex and demonstrated that the interaction of propylene with sulphate species activates the hydrocarbon molecule up to a large extent. Moreover, we showed that the simulated IR spectrum of the adsorbed alkyl-sulphate can be very useful to the identification of this surface species. The peaks at 1078 and 1047 $cm^{-1}$ and the splitting of the $SO_4$ group frequencies of the sulphate unit are the fingerprint of this intermediate.

## 4.5 References and Notes


[1] F. Zaera, *Chem. Rev.* 95 (1995) 2651.
[2] P.C. Stair, G.A. Somorjai, *Chem. Phys. Lett.* 41 (1976) 391.
[3] L.L. Kesmodel, L.H. Dubois, G.A. Somorjai, *Chem. Phys. Lett.* 56 (1978) 267.
[4] R.J. Koestner, J.C. Frost, P.C. Stair, M.A. van Hove, G.A. Somorjai, *Surf. Sci.* 116 (1982) 85.
[5] L.L. Kesmodel, L.H. Dubois, G.A. Somorjai, *J.Chem. Phys.* 70 (1979) 2180.
[6] X.-Y. Zhou, X.-Y. Zhu, J.M. White, *Surf. Sci.* 193 (1988) 387.
[7] D.B. Kang, A.B. Anderson, *Surf. Sci.* 155 (1985) 639.
[8] A.B. Anderson, S.J. Choe, *J. Phys. Chem.* 93 (1989) 6145.
[9] E.A. Carter, B.E. Koel, *Surf. Sci.* 226 (1990) 339.
[10] D. Godbey, F. Zaera, R. Yeates, G. A. Somorjai, *Surf. Sci.* 167 (1986) 150.
[11] F. Zaera, *J. Am. Chem. Soc.* 111 (1989) 4240.
[12] M. Salmerón, G. A. Somorjai, *J. Phys. Chem.* 86 (1982) 341.
[13] N. R. Avery, N. Sheppard, *Proc. R. Soc. Lond. A* 405 (1986) 1.
[14] A. Cassuto, M. Mane, G. Tourillon, P. Parent, J. Jupille, *Surf. Sci.* 287/288 (1993) 460.
[15] A. B. Anderson, D.B. Kang, Y. Kim, *J. Am. Chem. Soc.* 106 (1984) 6597.
[16] Y.-L. Tsai, C. Xu, B.E. Koel, *Surf. Sci.* 385 (1997) 37.
[17] F. Zaera, D. Chrysostomou, *Surf. Sci.* 457 (2000) 71; ibid. 457(2000)89.

[18] H. Steininger, H. Ibach, S. Lewald, *Surf. Sci.* 117 (1982) 685.
[19] C. E. Anson, N. Sheppard, B. R. Bender, J.R. Norton, *J. Am. Chem. Soc.* 121 (1999) 529.
[20] K.M. Ogle, J.R. Creighton, S. Akhter, J.M. White, *Surf. Sci.* 169 (1986) 246.
[21] S. Brunet, D. Mey, G. Perot, C. Bouchy, F. Diehl, *Appl. Catal. A General* 278 (2005) 143.
[22] K. Wilson, C. Hardacre, R.M. Lambert, *J. Phys. Chem.* 99 (1995) 13755.
[23] K. Wilson, A.F. Lee, C. Hardacre, R.M. Lambert, *J. Phys. Chem. B* 102 (1998) 1736.
[24] A.F. Lee, K. Wilson, R.M. Lambert, C.P. Hubbard, R.G. Hurley, R.W. McCabe, H.S. Ghandi, *J. Catal.* 184 (1999) 491.
[25] A.F. Lee, K. Wilson, A. Goldoni, R. Larciprete, S. Lizzit, *Surf. Sci.* 513 (2002) 140.
[26] A.F. Lee, K. Wilson, A. Goldoni, R. Larciprete, S. Lizzit, *Catal. Lett.* 78 (2002) 379.
[27] B. Hammer, L. B. Hansen, J. Nørskov, *Phys. Rev. B* 59 (1999) 7413.
[28] F. Delbecq, P. Sautet, *J. Catal*. 211 (2002) 398.
[29] Angle between the $C^1$–$C^2$ bond and the $C^1H_2$ plane.
[30] Q. Ge, D. A. King, *J. Chem. Phys.* 110 (1999) 4699.
[31] G. W. Watson, R. P. K. Wells, D. J. Willock, G. J. Hutchings, *J. Phys. Chem. B* 104 (2000) 6439.
[32] A. Valcárcel, A. Clotet, J.M. Ricart, F. Delbecq, P. Sautet, *Surf. Sci.* 549 (2004) 121.
[33] Q. Ge, D.A. King, *J. Chem. Phys.* 110 (1999) 4699.
[34] M. J. Frisch et al., Gaussian 98 revision A6, Gaussian Inc., Pittsburgh, PA, 1998
[35] A.D. Becke, *J. Chem. Phys.* 98 (1993) 5648.
[36] D. Curulla, A. Clotet, J.M. Ricart and F. Illas, *J. Phys. Chem. B* 103 (1999) 5246.
[37] P. Hay and W. R. Wadt, *J. Chem. Phys.* 82 (1985) 299.
[38] S. Zurita, F. Illas, J. C. Barthelat, J. Rubio, *J. Chem. Phys*. 104 (1996) 8500.
[39] S. F. Boys, F. Bernardi, *Mol. Phys.* 19 (1970) 553.
[40] R. W. G. Wyckoff, *Crystal Structures*, 2nd ed., vol. 1, Interscience Publishers, New York (1965).
[41] R. Hoffmann, *Solids and surfaces*, VCH, New York (1988).
[42] E. Schustorovich, R.C. Baetzold, *Science* 227 (1985) 876.
[43] R. A. van Santen, *Cat. Lett.* 16 (1992) 59.
[44] M. Neurock, R. A. van Santen, *J. Phys. Chem. B* 104 (2000) 11127.
[45] S. G. Podkolzin, R. Alcalà, J.A. Dumesic, *J. Molec. Catal. A* 218 (2004) 217.
[46] These modes are strongly affected by the anharmonicity.
[47] M.A. Chesters, C. de la Cruz, P. Gadner, E. M. McCash, P. Pudney, G. Shahid, N. Sheppard, *J. Chem. Soc. Faraday Trans.* 86 (1990) 2757.
[48] X. Lin, W.F. Schneider, B.L. Trout, *J. Phys. Chem. B* 108 (2004) 250.
[49] K. Wilson, C. Hadacre, C.J. Baddeley, J. Lüdecke, D.P. Woodruff, R.M. Lambert, *Surf. Sci.* 372 (1997) 279.

# Appendix A

**A.1.** Main IR peaks (in $cm^{-1}$) for $CH_3CCD$ and $CD_3CCH$ on Pt(111): 2x2 unit cell

| vibrational | $CH_3CCD$ | | vibrational | $CD_3CCH$ | |
|---|---|---|---|---|---|
| mode | $\omega_i$ | $I_i$[a] | mode | $\omega_i$ | $I_i$[a] |
| CD st | 2246 | 0.6 | CH st | 3048 | 1.2 |
| $CH_3$ as st | 3028 | 0.7 | $CD_3$ as st | 2241 | 0.5 |
| $CH_3$ as-s st | 3011 | 2.1 | $CD_3$ as-s st | 2228 | 1.1 |
| $CH_3$ s st | 2943 | 7.2 | $CD_3$ s st | 2113 | 2.8 |
| $CH_3$ as-s df + $C^1$–$C^2$ st | 1432 | 0.7 | $C^1$–$C^2$ st | 1361 | 0.8 |
| $CH_3$ as df | 1407 | 2.0 | $CD_3$ as df | 1011 | 1.3 |
| $C^1$-$C^2$ st – $CH_3$ as-s df | 1346 | 0.1 | $CD_3$ as-s df | 1023 | 0.0 |
| $CH_3$ s df | 1330 | 1.6 | $CD_3$ s df[b] | 1066 | 1.4 |

Key: as, asymmetric; s, symmetric; st, stretching; df, deformation; ro, rocking; b, bending.
[a]Intensities in $Kmmol^{-1}$. [b]tnis mode mixes with the CH bi and $C^2$–$C^3$ st modes.

**A.2.** Main IR peaks (in $cm^{-1}$) for $CH_3CCD$ and $CD_3CCH$ on Pd(111): 2x2 unit cell

| vibrational | $CH_3CCD$ | | vibrational | $CD_3CCH$ | |
|---|---|---|---|---|---|
| mode | $\omega_i$ | $I_i$[a] | mode | $\omega_i$ | $I_i$[a] |
| CD st | 2246 | 0.3 | CH st | 3045 | 0.7 |
| $CH_3$ as st | 3016 | 0.7 | $CD_3$ as st | 2231 | 0.4 |
| $CH_3$ as-s st | 3004 | 2.7 | $CD_3$ as-s st | 2223 | 1.5 |
| $CH_3$ s st | 2935 | 9.1 | $CD_3$ s st | 2106 | 3.7 |
| $CH_3$ as-s df + $C^1$–$C^2$ st | 1436 | 0.7 | $C^1$–$C^2$ st | 1410 | 0.1 |
| $CH_3$ as df | 1403 | 1.0 | $CD_3$ as df | 1010 | 1.2 |
| $C^1$-$C^2$ st – $CH_3$ as-s df | 1385 | 0.4 | $CD_3$ as-s df | 1025 | 0.1 |
| $CH_3$ s df | 1327 | 0.8 | $CD_3$ s df | 1061 | 1.3 |

Key: as, asymmetric; s, symmetric; st, stretching; df, deformation; ro, rocking; b, bending.
[a]Intensities in $Kmmol^{-1}$.

**A.3.** Simulated vibrational spectra for the possible $C_3H_x$ (x= 3–7) intermediates on Pt(111): 2x2 unit cell

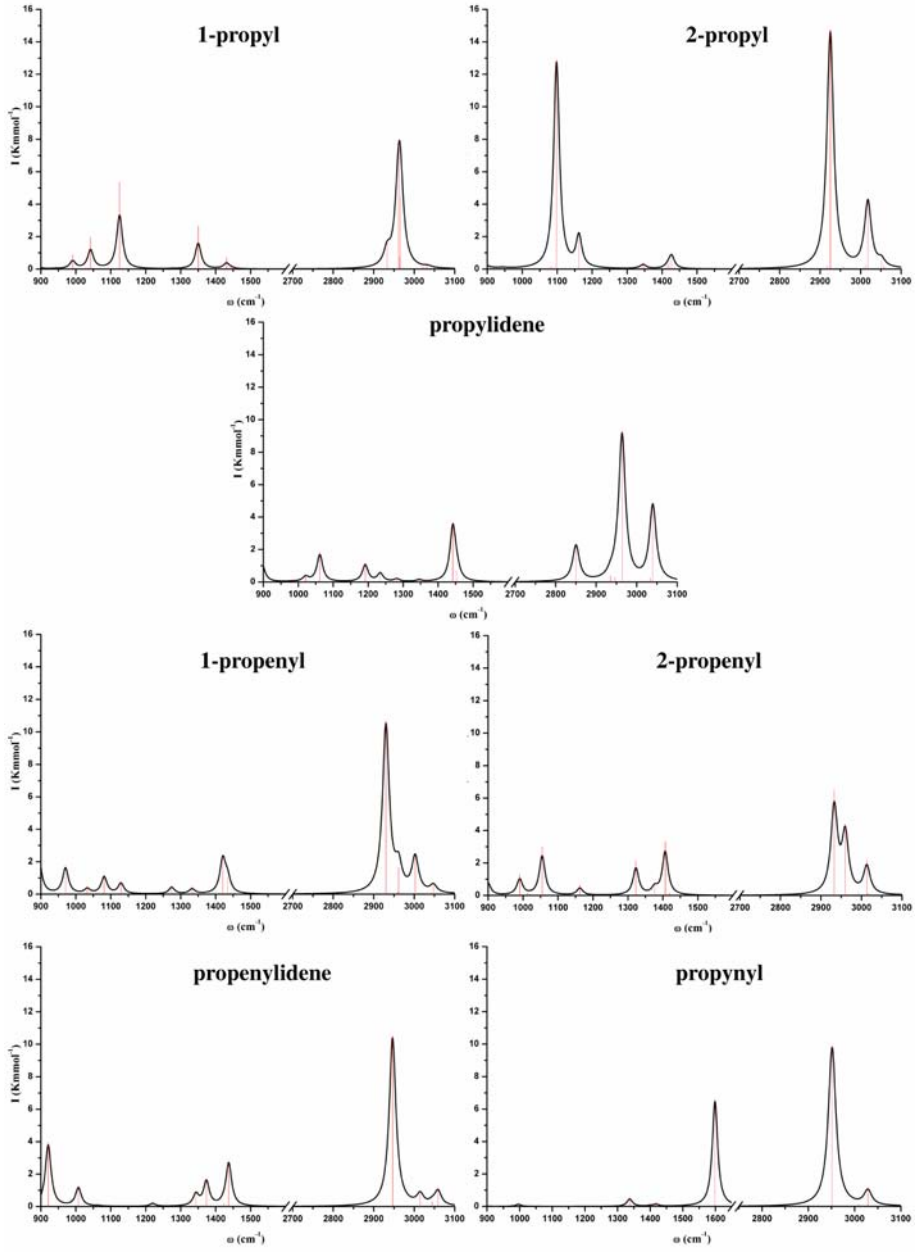

**A.4** Vibrational frequencies (in $cm^{-1}$) for the gas phase 1,3-butadiene molecule

| Exp.[a] | Computed | Assignment |
|---|---|---|
| 3100 | 3217 | $CH_2$ as st |
| 3100 | 3179 | $CH_2$ as st |
| 3055 | 3122 | CH st |
| 3013 | 3049 | $CH_2$ s st |
| 3010 | 3035 | $CH_2$ s st |
| 3013 | 3007 | CH st |
| 1644 | 1647 | C=C s st |
| 1597 | 1600 | C=C as st |
| 1441 | 1428 | $CH_2$ s sci |
| 1381 | 1372 | $CH_2$ as sci |
| 1291 | 1286 | CH bi |
| 1295 | 1272 | CH bi |
| 1203 | 1196 | C-C st |
| 1014 | 1029 | CH bo |
| 965 | 970 | CH bo |
| 990 | 968 | $CH_2$ as ro |
| 908 | 905 | $CH_2$ as wag |
| 908 | 901 | $CH_2$ s wag |
| 888 | 877 | $CH_2$ s ro |
| 752 | 762 | $CH_2$ as twi |
| 525 | 535 | $CH_2$ s twi |
| 512 | 502 | C=C-C bi |
| 291 | 270 | C=C-C bo |
| 163 | 184 | C-C to |

Key: as, asymmetric; s, symmetric; st, stretching; sci, scissoring; bi, bending in plane; bo, bending out of plane; ro, rocking; wag, wagging; twi, twisting.
[a] values from G.R. De Maré *et al. J. Chys. Chem* A 148 (1988) 13.

**A.5.** Temperature-pressure phase diagrams for 1,3 butadiene and 1-butene on Pt(111) and Pd(1111)

A.5.1. Pt(111)

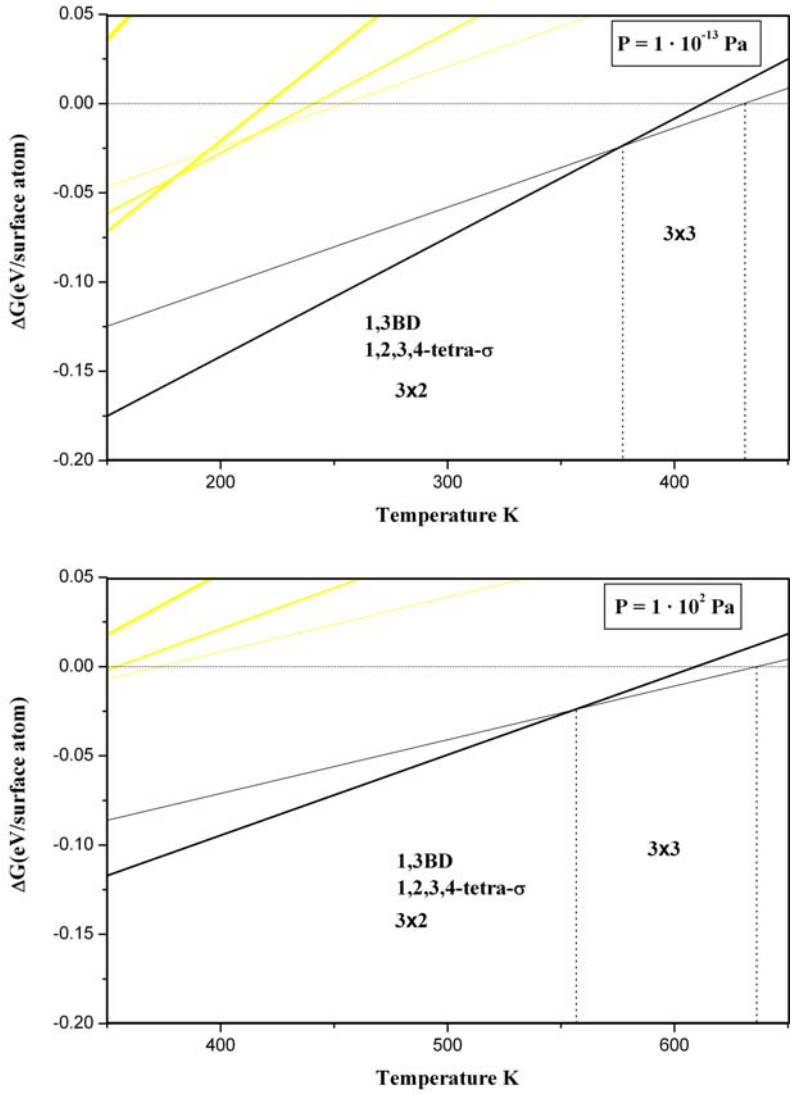

A.5.2. Pd(111)

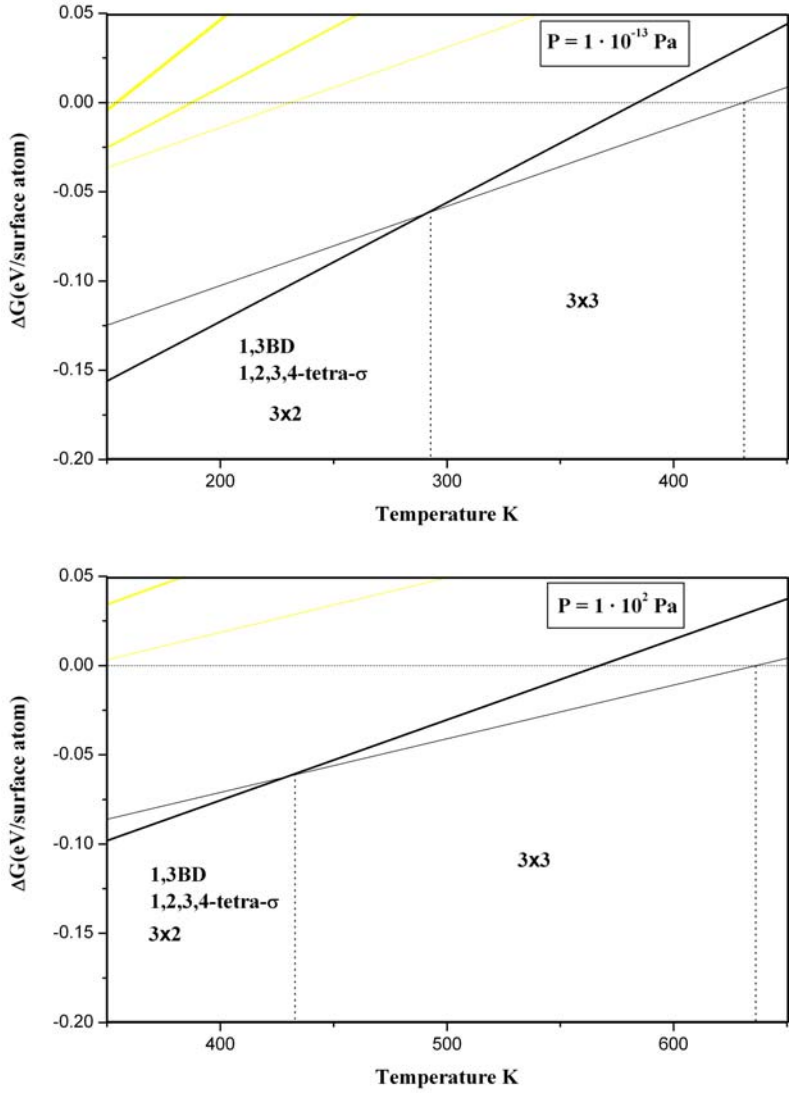


1,3BD (1,3-buradiene, black) and 1B (1-butene, yellow) on Pt(111) (A.5.1) and Pd(111) (A.5.2). Here, we depicted only the most stable adsorption modes (1,2,3,4-tetra-σ for 13BD and di-σ for 1B). The thicker the line the higher the coverage.

**A.6.** Co-adsorption of hydrogen and $C_4H_x$ species (x= 6,7) on Pt(111) and Pd(111)

| species | H position[a] | ΔE(kJmol$^{-1}$)[b] |
|---|---|---|
| | **Pt(111)** | |
| 13BD | 1 | 30 |
| | 2 | 16 |
| | 3 | 32 |
| | 4 | 17 |
| 1B4R | 1 | 11 |
| | 2 | 24 |
| | 3 | 26 |
| 2B1R | 1 | 21 |
| | 2 | 8 |
| | 3 | 20 |
| | **Pd(111)** | |
| 13BD | 1 | 25 |
| | 2 | 18 |
| | 3 | 54 |
| | 4 | 17 |
| 1B4R | 1 | 11 |
| | 2 | 29 |
| | 3 | 22 |
| 2B1R | 1 | 19 |
| | 2 | 30 |
| | 3 | 17 |

[a] H position from Figure 5.9 (Chapter 5). [b]Energy difference between the co-adsorbed system ($C_4H_x$ and H adsorbed on the same unit cell) and the two species at infinite distance. On co-adsorption the system is destabilised.

# 1

# General introduction

*In this chapter we discuss the motivation for the research presented in this thesis. We would like to emphasise the importance of a detailed knowledge of surface processes at a molecular level. In this thesis we deal with the interaction between unsaturated hydrocarbons (adsorbates) and metal surfaces. Adsorbate is the general term for a molecule that establishes an attractive interaction with a surface. After interacting, the molecule can diffuse, react with other molecules, decompose or finally desorb. The detailed characterisation of surface overlayers, the accurate assignment of vibrational spectra of adsorbed molecules, and the exhaustive scan of the possible reaction pathways are not only of fundamental importance but also of interest for many applications such as heterogeneous catalysis. Computational Chemistry can be a valuable experimental partner for understanding surface processes.*

*This chapter is organised as follows: section 1.1 discusses the importance and the fast and amazing development of surface science and heterogeneous catalysis; section 1.2 briefly explains the uses of unsaturated hydrocarbons in the chemical industry; section 1.3 discusses the role of vibrational spectroscopies in surface science and heterogeneous catalysis; section 1.4 briefly describes the evolution of theoretical tools to simulate surface phenomena; section 1.5 justifies the use of single crystals to model catalysts; and section 1.6 discusses the scope of this theses and provides an outline of it.*

## 1.1 Introduction

Though surface science touches on a wide range of applications and basic science, its traditional realm has always been heterogeneous catalysis. From a historical perspective, the contributions of surface science to catalysis are obvious. Technologies based on surface-catalysed chemistry first emerged between 1870 and 1912 when key processes were developed such as the oxidation of hydrochloric acid to chlorine (Deacon process, 1871), the oxidation of sulphur dioxide to sulphur trioxide (Messel, 1875), the reaction of methane with carbon dioxide and hydrogen (Mond, 1888), the oxidation of ammonia (Oswald, 1901), the oxidation of ethylene (Sabatier, 1902) and the synthesis of ammonia (Haber, Mittasch, 1905–1912) [1].

Surface chemistry has become the centre of chemistry development thanks to its importance in the chemical industry. It has progressed very quickly, particularly in the production areas of commodity chemicals (e.g. olefins, methanol, ethylene glycol) and petroleum refining.

Along with the discovery of numerous processes relevant to the industry, new instrumentation and surface techniques have been developed [2]. The emphasis has been on surface probes that enable the study of various surface properties, such as structure, chemical composition, oxidation states, vibrations of adsorbates, heats of adsorption. Some of the most popular surface science techniques of the last four decades are: Low Energy Electron Diffraction (LEED), Photoelectron Diffraction (PhD), Reflection Absorption Infrared Spectroscopy (RAIRS), High Resolution Electron Energy Loss Spectroscopy (HREELS) and Thermal Desorption Spectroscopy (TDS), to name but a few. None of these techniques provides all the information needed and the tendency is to use a combination of them.

Parallel to the improvement of the structural determination methods, the development of *ab initio* calculations based on electronic structure theory has greatly improved our understanding of surface processes at a molecular level. In the 1990s, periodic first-principle calculations within the Density Functional Theory (DFT) framework became affordable. These methods have emerged as a helpful partner for researching reactivity on surfaces because they provide detailed information of surface phenomena for systems of considerable size.

The amazing growth of surface chemistry has continued uninterrupted to the present day. Today, heterogeneous catalysis is the basis of the chemical industry. In fact, more than 90% of chemical manufacturing processes use catalysts in one form or another, and new technologies involving catalysts are introduced every year [3]. The economic importance of catalyst development is obvious.

## 1.2 Unsaturated hydrocarbons and their importance in the chemical industry

The catalytic conversion of hydrocarbons is at the heart of many important industrial processes such as oil refining, commodity chemicals manufacturing, pharmacological synthesis and the abatement of polluting by-products [4].

The study of the structure, properties and reactivity of molecules such as propylene, butadiene or butene and propyne over metal surfaces on simple models and ideal conditions is not just of academic interest, it is also useful for understanding intricate industrial processes. The importance of these molecules in our everyday lives is unquestionable. In fact, propylene (or propene) is one of the major building blocks of the petrochemical industry. This molecule is usually obtained as a co-product of the catalytic cracking process to obtain gasoline, as a co-product of the steam cracking process used to make ethylene, or by dehydrogenation of propane. The materials derived from propylene include: polypropylene, acrylonitrile, propylene oxide, oxo alcohols, cumene and isopropyl alcohol. This species is therefore a key constituent of innumerable products: CDs and optical disks; clear film food wrap; eyeglasses flexible foams used in furniture; rigid foam insulation; bullet-proof windows; car headlights, disk brake pads and bumpers; and a huge amount of moulded plastic goods such as food containers and kitchen utensils. Butenes (1-butene and 2-butene), 1,3-butadiene and propyne are also valuable raw materials. These compounds are primarily obtained from refinery gases ($C_4$ fraction) or as by–products of ethylene and propylene production. Most butenes are used for the production of octanes, which are important constituents of gasoline. 1-butene also fills an important role in the production of low-density polyethylene. The largest use of 1,3-butadiene is in the production of styrene-butadiene rubber, which is used to manufacture tyres, adhesives, sealants, coatings and the soles of shoes. Propyne (methylacethylene) is also a product of naphtha cracking. This molecule (together with propadiene) is one of the main components of a fuel gas used in gas welding (to manufacture metal and thermoplastics).

## 1.3 Experimental techniques relevant to research on metal surfaces

Detailed knowledge of the adsorbate-surface interaction is crucial to understanding the subsequent surface processes. Various spectroscopies (UPS, TDS, NEXAFS, RAIRS, EELS) and other techniques (LEED, PhD) have already provided information on surface species generated by adsorption. **Table 1.1** presents some of these surface science techniques and gives a short explanation of the information we can obtain.

There is no doubt that vibrational spectroscopies (RAIRS and HREELS) have been a prime analytical tool in heterogeneous catalysis for half a century. They have played a crucial role in surface science thanks to their enormous versatility. This is not surprising and the reasons are not hard to find: both RAIRS and HREELS are non–destructive techniques; spectra can be obtained using inexpensive commercial spectrometers; and there is invaluable literature to help interpret the spectra. Moreover, infrared spectroscopy can operate under conditions of pressure and temperature that are not far removed from those for catalytic reactions. On the other hand, while HREELS employs low energy electrons and is necessarily restricted to ultra-high vacuum (UHV), the use of such low energy electrons ensures that it is highly sensitivity. We offer a more detailed description of these techniques in **section 2.6, Chapter 2.**

**Table 1.1** Some of the methods available for studying surfaces

| Acronym | Name | Information gained |
|---|---|---|
| HREELS *or* VEELS | High Resolution Electron Energy Spectroscopy *or* Vibrational Electron Energy Spectroscopy | Adsorbate vibrations |
| LEED | Low Energy Electron Diffraction | Structure of the near surface region |
| NEXAFS *or* XANES | Near Edge X-ray Absorption Fine Structure Spectroscopy *or* X-ray Absorption Near Edge Spectroscopy | Orientation of the adsorbed molecules |
| PhD | Photoelectron Diffraction | Structural information around each atomic species |
| RAIRS | Reflection Absorption Infrared Spectroscopy | Adsorbate vibrations |
| UPS | Ultraviolet Photoemission Spectroscopy | Bonding of adsorbates to the surface |
| TPD *or* TDS | Temperature Programmed Desorption *or* Thermal Desorption Spectroscopy | Adsorption energies; natures of the adsorbed species |

Hydrocarbons can suffer isomerisation or decomposition reactions on the surface. In such cases, vibrational spectroscopy usually fails. Also, band assignment is too complex and the structural information obtained is often incorrect. To obtain all the information we need, we can use a combination of techniques. The information provided by 'real' quantitative techniques such as PhD and LEED can help us to interpret vibrational spectra. Unfortunately, these techniques require very expensive instrumentation, cumbersome procedures and complex mathematical treatments of the data. Theoretical calculations can provide a rigorous way to assign all the observed frequencies unambiguously and at no extra cost.

## 1.4 Contributions from computational chemistry

Many of the advances in heterogeneous catalysis have been achieved serendipitously or, at best, by trial and error. The key question is how electronic structure calculations can help us in the rational design of catalysts. Experimental characterisation of active sites and the detection of reaction intermediates are always challenging. Simulation can allow specific questions to be asked and focus costly experimental work on solving particular problems. Besides, short-lived transition states are extremely difficult or impossible to study by direct experiment. One hopes that reliable calculations will reveal insights into otherwise inaccessible reaction pathways.

Researchers have been trying to develop a general theoretical framework for understanding the processes that occur on surfaces and predict molecular structures, bond energies, molecular properties, transition state structures and energies for systems of

increasing size. Unfortunately, the lack of hardware (powerful computers) and software (efficient algorithms) has for years hindered the application of first-principles theory in catalysis.

In the 1970s and 1980s, quantum chemistry methods were already very successful. The Hartree-Fock (HF) method and simplified techniques such as the Extended Hückel (EH) method became standard tools for studying organic and main-group inorganic molecules. More sophisticated techniques based on the HF method, the so-called post-HF methods, were also developed. These post-HF methods improved the description of the electronic structure and provided highly accurate results. Although these methods have contributed considerably to our understanding of surface processes, their applications have been restricted to rather small systems. Catalytic systems are generally too big to be handled. The Density Functional Theory (DFT) based methods were an alternative way to study heterogeneous catalytic processes. The theoretical chemistry community was averse to accepting DFT for a long time because it believed the methods were not accurate enough [5]. Thanks to developments in the formulation of DFT algorithms, the accuracy reached by these methods is now comparable to that of expensive post-HF methods. Since the 1990s, DFT-based methods have become more and more popular among computational chemists. For the large and medium systems, DFT is the optimal tool for achieving a good accuracy in the results with modest computational demands.

Today, theoretical calculations have reached the point where molecular structures are predicted to an accuracy comparable to that of the most sophisticated experiments [6,7]. Moreover, as calculated vibrational spectra are usually close to the experimental values, they provide a rigorous way to assign all the observed frequencies in an unambiguous way.

There have been dramatic advances in hardware along with the development of new algorithms and theoretical methods. Improved computer performance has also been crucial to the advances in quantum chemistry. Faster single processors and parallel architectures with many lower cost processors have made the treatment of larger problems affordable. At the same time, the introduction of user-friendly graphical interphases has made high-performance computing available to a wider community.

The increasing number of papers and the Nobel Prizes awarded to Professors John A. Pople and Walter Khon are obvious indicators that computational chemistry has reached a significant point in its development. Modelling, theory and simulation can improve our understanding of known systems, provide qualitative (and even quantitative) insights into experimental results and guide the design of new systems [8].

## 1.5 Model catalysts

A catalyst is an active chemical spectator. The catalyst speeds up a reaction by lowering the activation barrier. However, the acceleration of the reaction is not the key factor. The catalysts must speed up the right reaction (i.e. it has to be *selective*) [9].

The first step in each heterogeneous catalytic process is the adsorption of the reactants on the active phase of the catalysts, which usually consists of metal particles. The complexity of the ‘real’ catalysts makes it demanding to establish a molecular level

understanding of the surface processes. A first approach to studying the surface chemistry of hydrocarbons is obtained by modelling single-crystal surfaces [10,11] and therefore avoiding the complexities of the actual catalysts. The basic idea behind the use of single-crystals is that the small metal particles of the 'real' catalysts exhibit the same or similar crystalline phases and the same or similar electronic structure. Although these studies neglect the effect of the support and particle size, they do reveal certain aspects of how surface reactions proceed and can significantly contribute to our understanding of heterogeneous catalytic processes.

### 1.6 Scope and outline of this thesis

The aim of this thesis is to study the structure and reactivity of several unsaturated hydrocarbons on metal surfaces using Density Functional Theory methods. We have studied three systems: propyne on the (111) surface of Cu, Pt, Pd and Rh; propylene on Pt(111) and 1,3-butadiene and butenes on Pt(111) and Pd(111).

In the following Chapters, we will show that first-principle calculations can play a crucial role in characterising adsorbed overlayers, help to assign complicated vibrational spectra of large molecules and help to identify surface intermediates. This is invaluable in the study of surface reactions. The aims of this thesis are therefore several:

- To describe the adsorbate-surface interaction. To compare the adsorption structures with experimental data available. To identify short-lived reaction intermediates. To establish their structure and properties.

- To quantitatively simulate the vibrational spectra of adsorbed hydrocarbons. To compare with experimental spectra and corroborate band assignation. To determine the fingerprint for short-lived reaction intermediates.

- To study the possible reaction pathways. To establish the thermochemistry for hydrocarbon intermediates. To obtain the transition states. To calculate the reaction barriers. To provide insights into the factors that control reaction selectivity.

The thesis is outlined as follows.

In this Chapter (**Chapter 1**), we summarise the motivations behind the thesis, the aims and the questions it addresses.

In **Chapter 2**, we briefly describe the method we used for our quantum calculations. We also provide the computational details for this particular study.

After these introductory chapters we discuss our results. In **Chapter 3**, we describe in detail the application of normal mode calculations to interpret RAIRS and HREELS spectra of propyne on a series of metal surfaces (Cu, Pt, Pd and Rh). We would like to emphasise that not knowing the extent to which normal modes are made up of two or more internal coordinates can lead to confusion as to whether observed isotopic shifts are reasonable or not. We were able to study the isotopic effects thanks to the IRIAN code [12].

In **Chapter 4**, we investigate the decomposition of propylene on the clean and sulphated Pt(111) surface. We determine the nature and relative stability of each of the decomposition fragments. The study is completed by simulating vibrational spectra. We aim to find the fingerprint of short-lived surface intermediates so that they can be identified in experiments.

In **Chapter 5**, we study the hydrogenation of 1,3-butadiene on the Pt(111) and Pd(111) surfaces mainly to determine the causes of the different selectivity observed experimentally on these metal surfaces. We explore the possible reaction pathways in detail and focus on the role of reaction intermediates.

In **Chapter 6** we present our main conclusions from the foregoing chapters. Finally, we provide a summary in Catalan and a list of published and submitted publications.

## 1.7 References and Notes


[1] G.A. Somorjai, *Introduction to Surface Chemistry and Catalysis*, John Wiley and sons, Inc., New York (1994).

[2] J. W. Niemantsverdriet, *Spectroscopy in Catalysis*, Wiley-VCH (2000).

[3] J.M. Thomas, W. J. Thomas, *Principles and practice of Heterogeneous Catalysis*, VCH, Bassel – NewYork (1997).

[4] F. Zaera, *Israel Journal of Chemistry* 38 (1998) 293.

[5] A. Gross, *Surf. Sci*. 500 (2002) 347.

[6] L.A. Curtiss, K. Raghavachari, G.W. Trucks, J.A. Pople, *J. Chem. Phys*. 94 (1991) 7221.

[7] M. Alcami, O. Mo, M. Yañez, *Mass. Spectrom. Rev*. 20 (2001) 195.

[8] H. Arakawa, M. Aresta, J. N. Armor, M. A. Barteau, E. J. Beckman, A. T. Bell, J. E. Bercaw, C. Creutz, E. Dinjus, D. A. Dixon, K. Domen, D. L. DuBois, J. Eckert, E. Fujita, D. H. Gibson, W. A. Goddard, D. W. Goodman, J. Keller, G. J. Kubas, H. H. Kung, J. E. Lyons, L. E. Manzer, T. J. Marks, K. Morokuma, K. M. Nicholas, R. Periana, L. Que, J. Rostrup-Nielson, W. M. H. Sachtler, L. D. Schmidt, A. Sen, G. A. Somorjai, P. C. Stair, B. R. Stults, W. Tumas, *Chem. Rev.* 101 (2001) 953.

[9] K.W. Kolasinski, *Surface Science: Foundations of catalysis and nanoscience*, John Wiley and sons, ltd.New York-Weinheim-Queensland-Singapore-Ontario (2002).

[10] N. Sheppard, C. De la Cruz, *Adv. Catal*. 41 (1996) 1.

[11] B. Hammer, J.K. Norskov, *Adv. Catal.* 45 (2000) 71.

[12] IRIAN program was developed by A. Clotet. Universitat Rovira i Virgili. Tarragona. Spain (2003).

# Contents

# List of abbreviations and symbols

| | |
|---|---|
| BSSE | Basis set superposition error |
| DFT | Density functional Theory |
| DOS (PDOS) | Density of states or Projected density of states |
| EELS (HREELS or VEELS) | Electron energy loss spectroscopy ( High resolution electron energy loss spectroscopy or vibrational energy loss spectroscopy) |
| $E_{ads}$ | Adsorption energy |
| $E_{CxHy/surface}$ | Energy of the system adsorbate-surface |
| $E_{CxHy\ (g)}$ | Energy of the hydrocarbon in the gas phase |
| $E_{surface}$ | Energy of the surface |
| $E_{reac}$ | Reaction energy |
| $E_{TS}$ | Energy of the transition state |
| GGA | Generalised gradient approximation |
| H–L | HOMO (highest occupied molecular orbital)–LUMO (lowest unoccupied molecular orbital) |
| $I_i$ | Intensity |
| IR | Infrared |
| IRIAN | |
| LDA | Local density approximation |
| LEED (LEED-IV) | Low energy electron diffraction (Low energy electron diffraction-Intensity voltage) |
| MEP | Minimum energy path |
| MSSR | Metal surface selection rules |
| NEB | Nudged elastic band |
| PAW | Projector augmented wave |
| PhD | Photoelectron diffraction |
| PW91 | Perdew-Wang 91 |
| RAIRS | Reflection absorption infrared spectroscopy |
| RECP | Relativistic effective core potentials |
| TDS | Thermal desorption spectroscopy |
| TS | Transition state |
| UHV | Ultra high vacuum |
| US-PP | Ultra soft pseudo potentials |
| VASP | Vienna ab initio simulation package |
| ZPE | Zero point energy |
| $\nu_i$ | Experimental frequency |
| $\omega_i$ | Harmonic calculated frequency |
| $\theta$ | Coverage |